Studies of Microdomain Structures and their Dynamic Behaviors in Block Copolymers(Dissertation_全文)

AUTHOR(S):

Okamoto, Shigeru

Studies of Microdomain Structures and their Dynamic Behaviors in Block Copolymers

Shigeru Okamoto

1997

Studies of Microdomain Structures and their Dynamic Behaviors in Block Copolymers

Shigeru Okamoto

1997

Contents

General Introduction

"Complex liquids" are one of the recent great concern in physics and materials science. Complex liquids are the liquid systems which cannot be understood by the simple model used for the simple liquids and liquid metals. The observed physical phenomena in a complex liquid system cannot be explained by the individual motion of constituent atoms or molecules. Instead, the collective motion plays an essential role. In other words, such a phenomenon cannot be reduced to the individual events of the elements. Not only a study of such a system is important in itself but also it may suggest a way to understand more complex systems. In this thesis I deal with one of the complex liquid systems.

A polymeric liquid/liquid mixture system is one of the typical examples of a complex liquid system. In the two-phase state, the system has an internal structure formed by the interfaces between the two polymeric liquid phases, while the two polymers form a homogeneous mixture without an internal structure in the one-phase state. On the phase transition from the one-phase state to the two-phase state, concentration fluctuations develops by the collective motion of the polymer molecules, resulting in the formation of interfaces with a variety of patterns. Such a phenomenon provides us with a fascinating subject to investigate.

Multicomponent polymer systems used for intensive investigations as complex liquids are classified into two major categories, polymer blends and block copolymers. The most important characteristic difference is that in the latter the two kinds of polymer molecules are connected by a covalent bond to form one molecule. In equilibrium, in the two-phase state a polymer blend phase-separates into two macroscopic domains like a water/oil system. On the other hand, a block copolymer cannot segregate macroscopically because of the chemical junction between the two components, resulting in formation of a periodic domain structure. Such a phase transition is called an order-disorder transition, or a microphase separation transition, and the resulting structure is called a microdomain structure. Therefore, the

characteristic spacing of a microdomain structure is of the order of the gyration radius of the block copolymer, i.e., 10-100 nm. This means that a block copolymer system is macroscopically homogeneous and microscopically heterogeneous, and hence contains a tremendously huge area of interfaces, which exhibit highly symmetric 3-dimensional structures on a 10-100-nm scale ("nanopatterns"). These nanopatterns themselves, and the physics of their formation are current topics of applied mathematics and physics.

An important characteristic of the microdomain structure of a block copolymer is that it is directional. The physical properties along a microdomain interface and perpendicular to it are expected to be different. Therefore, the property of a block copolymer as a material will be controlled by the orientation of the microdomain structure. In such a case, rheological information is extremely useful to understand its nature and to control its properties. Applying an external field, such as shear flow, may provide us a technique to affect the orientation of the interfaces, i.e., the alignment of molecules, and mesoscopic and macroscopic structures. From the viewpoint described above, I have investigated and performed detailed analyses of the static structures of block copolymer systems, which I present in this dissertation with studies of dynamic aspects of the nanopatterns of block copolymers under shear deformation in conjunction with their rheological properties. In this context, I discuss the rheo-optics of their orientational changes by mechanical stimuli, studied by the scattering and rheological techniques.

The size of the periodic domain structure of a block copolymer is 10-100 nm. Therefore, the small-angle X-ray scattering (SAXS) technique and transmission electron microscopy (TEM) were employed for the studies of the interfaces and the microdomain structures. Mechanical spectroscopy was employed to investigate the dynamic mechanical response. The time-resolved observations of the orientational changes were carried out in situ and in real time by the SAXS technique using two-dimensional (2D) detector, that was newly constructed for this purpose.

This dissertation consists of two parts. Part I contains 3 chapters (Chapters 1, 2, and 3), discussing microdomain formation and the static

structures of block copolymers, while Part II has 4 chapters (Chapters 4, 5, 6, and 7), discussing the development of a new 2D detector system for SAXS measurements and orientational changes of microdomains by mechanical stimuli, observed with the 2D detector system.

Chapter 1 first characterizes the ordering process of a polystyrene-*block*-polyisoprene-*block*-polystyrene triblock copolymer and the growth of the domain structures in a quiescent state by a rheological technique. The result is compared with that obtained in the conventional way by the scattering technique, which probes the thermodynamic behaviors of the block copolymer, i.e., miscibility of the constituent polymers.

In Chapter 2, the spatial arrangement of the constituent domains in a solvent-cast film of a polystyrene-*block*-poly(ethylene-*alt*-propylene) diblock copolymer in the strong segregation limit is investigated by SAXS and TEM techniques. Detailed analyses on the size and size distribution of the lamellar microdomains and their orientation in quiescent states are performed. The SAXS profiles are thoroughly analyzed using a one-dimensional paracrystal model.

In Chapter 3, I introduce a new molecular architecture in which three different polymer molecules, i.e., polystyrene, poly(*tert*-butyl methacrylate) and poly(dimethyl siloxane), are connected at a single junction point so that the copolymer has a shape of a three-arm star. Because of this complex molecular architecture, a new microdomain structure was observed. The new microdomain structure, investigated by TEM, SAXS and thermal analyses, seems to have three kinds of interfaces between each pair of the three components. The morphology constructed by those interfaces is quite different from Molau's classic morphologies such as lamellae, cylinders and spheres.

In Chapters 5,6, and 7, I discuss how block copolymers behave under oscillatory shear deformation. I employed block copolymers with various microdomain structures; a polystyrene-*block*-poly(ethylene-*alt*-propylene) diblock copolymer with lamellar microdomains, a polystyrene-*block*-polyisoprene-*block*-polystyrene triblock copolymer with cylindrical microdomains and a polystyrene-*block*-poly(ethylene-*alt*-propylene) diblock

copolymer with spherical microdomains in Chapters 5, 6, and 7, respectively. We constructed a new 2D detector system consisting of eight imaging plates (IP) for the time-resolved SAXS technique especially for oriented systems. The details of the 2D detector are presented in Chapter 4. In Chapter 5 I discuss static observations of oriented structures in the block copolymer set at the cessation of shear deformation. In Chapters 6 and 7, the orientational change of the microdomains, ordered in lattices, was observed in situ with the 2D detector system during shear deformation and after cessation. Moreover, dynamic measurement synchronous to shear deformation was carried out, in Chapter 7. The rheological properties of ordered microdomains were also measured in situ during the deformation and after the cessation of the deformation (Chapter 7).

In this thesis I intend to show how rich in research topics block copolymers are. The topics covered here are only a part of them, but spread over phase transition, pattern formation, topology of interfaces, mechanical property and structure control. Although the studies presented here are far from a complete understanding of the complex system, the combination of the rheological technique and the structure analysis by SAXS, especially with the 2D detector system, is proved to be effective in the study of block copolymer systems and sheds some light on the phenomena in the complex system.

Part I

Studies of Microdomain Structures in Block Copolymers

In 1976, Chung and Gale reported the first observation of rheological order-disorder transition (ODT) in the melt of a polystyrene-*block*-polybutadiene-*block*-polystyrene triblock copolymer.[1] Since then, the ODT in block copolymers has been a fascinating subject for many researchers. The phenomenon cannot be explained by a linear viscoelasticity theory and is considered to be related to a cooperative phenomenon in a complex liquid. I investigated the ODT in a triblock copolymer by means of small-angle X-ray scattering (SAXS) as well as a rheological technique and discuss the results in Chapter 1. The employment of the two techniques sheds some light on the ordering process of the block copolymer. In the remaining chapters of Part I, I present the studies of detailed analyses of microdomain structures and the novel morphological structures in block copolymers as revealed by SAXS and transmission electron microscopy.

Reference

(1) Chang, C. I.; Gale, J. C. *J. Polym. Sci., Polym. Phys. Ed.* **1976**, *14*, 1149.

Chapter 1

Order-Disorder Transition and Ordering Process of a Block Copolymer as studied by Small-Angle X-ray Scattering and Rheological Methods

1-1. Introduction

Block copolymers at temperatures below the ODT temperatures (T_{ODT}), form highly ordered morphologies with spatially periodic composition fluctuations (domains), while above T_{ODT}, the copolymer molecules are randomly mixed in a disordered state. Block copolymer phase transitions are weakly first order.[1] Roe et al.[2] and Hashimoto et al.[3-8] were the first groups to use scattering techniques for observing structural changes in block copolymers near the T_{ODT}. SAXS data on their diblock copolymer revealed that secondary peaks, showing long-range order, disappeared as the T_{ODT} was approached. The first-order peak intensity dropped to a weak intensity level relevant to the broad scattering maximum from disordered melts which was difficult to detect at short counting times for the X-ray scattering. It has also been well-established that the order-disorder transition affects the mechanical properties.[9-14] The long relaxation modes, as observed in the dynamic moduli at low frequencies, dropped significantly when heating through the ODT. Bates and coworkers[15,16] reported an interesting evolution of low-frequency dynamic mechanical properties above the T_{ODT} of a diblock copolymer. The ordered sample showed an extended power law relaxation region at low frequencies with $G' = G'' \sim \omega^{0.5}$. The dynamic mechanical behavior was in good agreement with consecutive small-angle neutron

scattering measurements on the same diblocks.[17]

Han et al.[18] studied SAXS and rheology of a triblock copolymer near ODT and found the corresponding T_{ODT}'s to be in agreement with each other. Similarly, Koberstein et al.[19] studied the ODT of a triblock copolymer and suggested a temperature difference of ~45 K between T_{ODT} by SAXS and T_{ODT} by rheology. This might be attributed to composition fluctuation effects on the scattering measurements. Using SAXS and rheology, Stühn et al.[20] observed a single ODT for a low molecular weight diblock copolymer (nearly symmetric composition). The transition behavior was symmetric in heating and cooling.

This chapter is concerned with the ordering of a strongly microphase separating triblock copolymer which forms cylindrical domains of the minor component in a continuous matrix of the major component. The cylinders arrange in a highly regular hexagonal lattice. The local order is defined by the direction of the cylindrical domains and by the orientation of the lattice planes. In the as-cast sample, the order is uniform within grains of ~1 μm, but the directors of domains and lattice planes vary randomly from grain to grain.

In the following, I will distinguish between (1) the single-phased or disordered structure, (2) the microphase-separated structure (local concentration fluctuations; formation of hexagonal lattice; microdomain scale ~50nm), (3) the grain network structure (grains of uniformly ordered structure, ~1μm, and random director change from grain to grain; continuity of PS domains across grain boundaries), and (4) the long-range order in which domain orientation and lattice orientation are uniform throughout the sample (~1-mm scale). A sample with such long-range order has been termed "single crystal".[21]

1-2. Experimental Section

1-2-1. Specimen

Polystyrene-*block*-polyisoprene-*block*-polystyrene (SIS) (designated as SIS-56) was prepared by anionic polymerization in cyclohexane using *sec*-butyllithium as initiator and the antioxidant 2,6-di-*tert*-butyl-4-methylphenol. The 1,4-content is 95 mol % (90% cis, 5% trans) and 5 mol % are 3,4 units. The number average molecular weight, M_n = 56 000, was determined by membrane osmometry and the heterogeneity index M_w/M_n = 1.1 by GPC where M_w is weight-averaged molecular weight. The weight percent composition is 24.3 % polystyrene and 75.7% polyisoprene by ^{13}C NMR, giving an equilibrium microphase-separated morphology of hexagonally packed cylinders of polystyrene (PS) in a polyisoprene (PI) matrix (evidenced by TEM and SAXS). The PI chains are much above and the PS chains are much below their entanglement molecular weight.

The polymer was dissolved in toluene to form ca. 10 wt.% polymer solution and cast into film on a glass plate at room temperature by slowly removing the solvent for 1 week. Thin polymer film of about 500 μm thickness was obtained. To further remove the solvent and the residual stresses introduced in the casting process, the film was vacuum-dried at 120 °C for 24 h. The thin film was cut into 3 mm-wide and 40 mm-long ribbons. The ribbon-shaped film specimens were stacked in a 4 mm-thick pile, and then used for the SAXS measurements.

1-2-2. Small-Angle X-ray Scattering

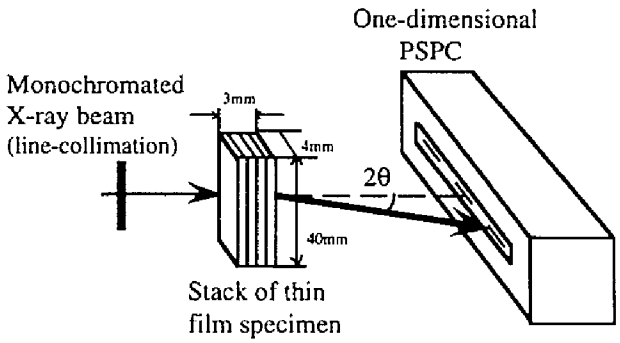

Figure 1-1. Experimental arrangement for the SAXS experiment showing schematically one-dimensional PSPC, and the line-focused X-ray image perpendicular to the surface of a stack of thin-film specimens. The scattering intensity distribution parallel to the film surface is measured (designated as "through configuration").

SAXS experiments were performed with the apparatus described in detail elsewhere.[7,22] The SAXS apparatus consists of a 12-kW rotating anode X-ray generator, a graphite crystal for incident beam monochromatization, a 1.5-m camera, and a one-dimensional position-sensitive proportional counter (PSPC). Line-focused Cu Kα radiation (λ= 0.154 nm) was used. The SAXS profiles were corrected for absorption due to the sample, the air scattering, the background scattering arising from thermal diffuse scattering due to density fluctuations, and slit height and slit width smearings.[23] The absolute scattered intensity was obtained by the nickel foil method.[24]

The SAXS profiles were measured for through configurations (the incident X-ray beam is perpendicular to the film surfaces and the scattering intensity distribution parallel to the film surface is measured; see Figure 1-1), and in situ as a function of temperature from 30 to 180 °C by incremental heating, using the temperature enclosure as described elsewhere.[5] The solution-cast film prepared as described above was used as a starting sample. The profiles at each temperature were obtained in situ with about 0.8-1.5 h of exposure to the X-ray beam on samples preheated for 0.5 h, to ensure thermal equilibration.

1-2-3. Rheometry

Dynamic mechanical properties were measured with parallel plate geometry using small-amplitude oscillatory shear ($\gamma = 0.03$) by RDS-7700, Rheometrics Co. Ltd., USA. Three different types of dynamic mechanical measurements were chosen to characterize the ODT of SIS-56: temperature sweeps at constant frequency ($\omega = 0.1$ rad/s), isothermal frequency sweeps over four decades of frequency (0.01 rad/s $< \omega <$ 100 rad/s), and isothermal time sweeps at constant frequency ($\omega = 0.1$ rad/s). Isothermal data were shifted both horizontally and vertically using the time-temperature superposition principle for the high-frequency end of the data. Shifting was performed with the interactive IRIS software.[25]

1-3. Results

1-3-1. ODT Determination by SAXS

The relative SAXS intensity, I, vs the magnitude of the wave vector, **q**, observed at various temperatures is shown in Figure 1-2(a),(b), where **q** is defined as

$$\mathbf{q} = (4\pi/\lambda)\sin(\theta/2) \qquad (1\text{-}1)$$

λ and θ are the wavelength of the X-ray and the scattering angle, respectively.

The initial morphology after solution casting consists of hexagonally packed cylinders of PS in a PI matrix. The cylinders align with a common director within grains. The director varies randomly from grain to grain herewith, producing a macroscopically isotropic structure. From the SAXS profile shown in Figure 1-2(a) (top curve), the peak positions can be estimated

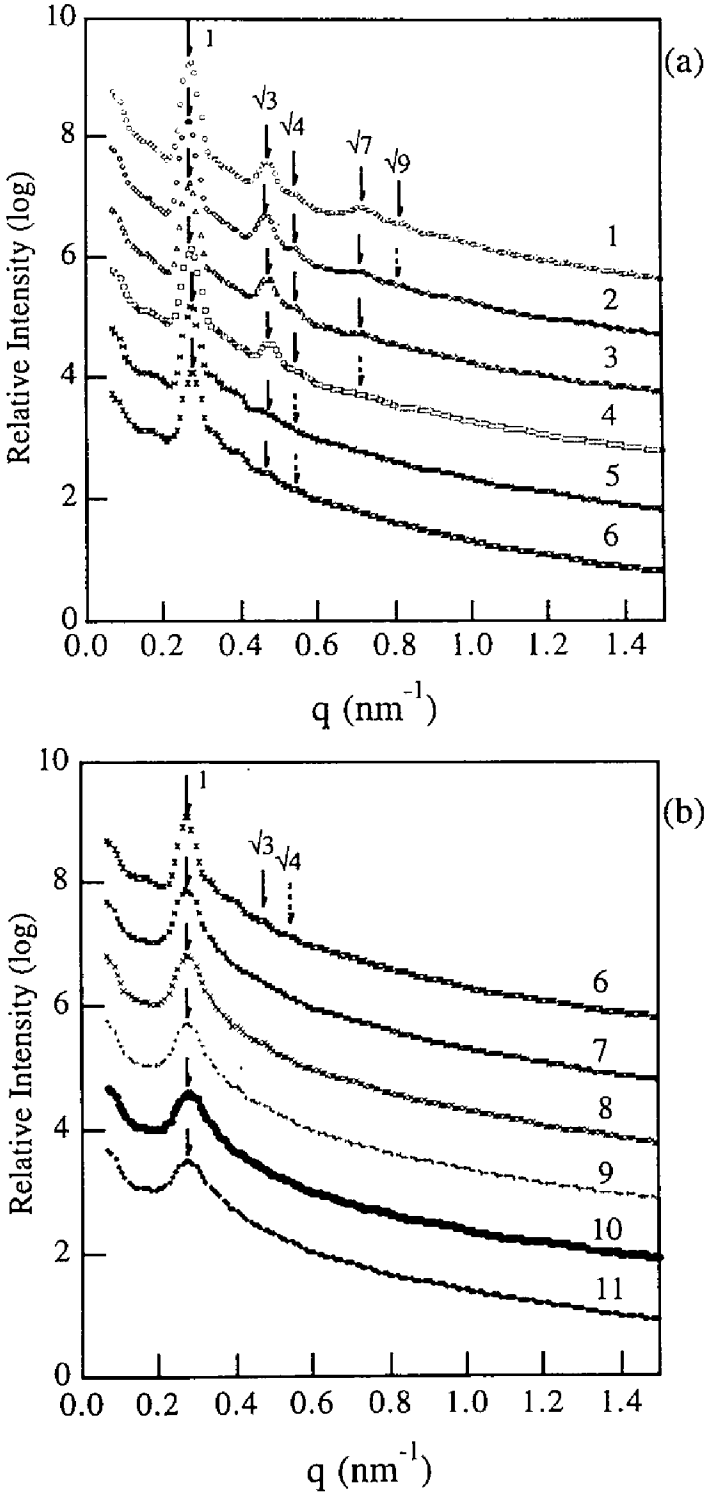

Figure 1-2. SAXS intensity profiles for heating (a) from 30 to 130 °C, and (b) from 130 to 180 °C. (1) 30, (2) 80, (3) 100, (4) 110, (5) 120, (6) 130, (7) 140, (8) 150, (9) 160, (10) 170, and (11) 180 °C.

to be as follows: θ = 21.8, 39.1, 45.8, 59.8, and 68.4 min which have a relation of 1, $\sqrt{3}$, $\sqrt{4}$, $\sqrt{7}$, and $\sqrt{9}$. This is typical for d-spacings of a hexagonally close packed array of cylinders with sufficiently long-range order. The intercylinder distance (lattice parameter) was calculated to be 28.1 nm. A cylinder diameter of 14.5 nm can be calculated from the lattice parameter and the volume fraction of PS, assuming a complete segregation of the constituent copolymer chains in their respective domains.

As the temperature was increased (Figure 1-2(a),(b)), the higher order intensity maxima gradually disappeared and for T $\geq$ 140 °C only the first-order maximum could be observed. However, it would be premature to regard these profiles at T $\geq$ 140 °C as those in the disordered state. The higher order maxima attributed to the regularity in the microdomain structures are known to become very weak in the vicinity of the ODT.

For SAXS measurements, earlier findings[8,26] suggest that the ODT can be characterized in two ways, the first one based on the Landau-type mean field theory developed by Leibler in the context of the random-phase approximation,[27-31] and the second one based on the Ornstein-Zernike theory.[32]

(i) From Figure 1-2(a) characteristic size D can be estimated both for the spatial segmental density fluctuations in the ordered state and for the thermal segmental density fluctuations in the disordered state,

$$D = 2\pi/q_m \qquad (1\text{-}2)$$

where q_m is $\mathbf{q}$ at the scattering angle θ_m of the first-order maximum. In the disordered state, this D or q_m is independent of temperature except for minor changes due to the temperature dependence of the radius of gyration (R_g) of polymer coils, i.e.,

$$D \sim T^{0} \text{ (disordered)} \tag{1-3}$$

While in the ordered state, D or q_m depends on temperature[8]

$$D \sim T^{1/3} \text{ (ordered)} \tag{1-4}$$

The transition from T^0 to $T^{1/3}$ behavior characterizes the ODT.

(ii) An alternative way to characterize the ODT involves the intensity measurements at any given $\mathbf{q}$ near q_m as a function of temperature. The intensity depends on χN, and if χ is written as found in most experimental results,

$$\chi = A + B/T \tag{1-5}$$

where A and B are constant values, then Leibler's Landau-type mean field theory predicts that, in the disordered state, $I^{-1}(\mathbf{q})$ linearly decreases with increasing T^{-1},

$$I^{-1}(\mathbf{q}) \sim T^{-1} \text{ (disordered)} \tag{1-6}$$

The deviations from eqs 1-3 and 1-6 are attributed to a consequence of an onset of the microphase separation and the microdomain formation. It was suggested that these two types of deviation should be simultaneously utilized to determine ODT.[33]

The results of D and $I^{-1}(\mathbf{q})$ as a function of T^{-1} are shown in Figure 1-3 for $\mathbf{q} = q^* = 0.278$ nm^{-1}, the wavenumber for the scattering maximum in the profile at 180 °C. Notice that there is a regime where D is independent of T

while $I^{-1}(\mathbf{q})$ linearly decreases with increasing T^{-1}. Deviations from the relations expressed by eqs 1-3 and 1-6 were observed at 130 °C ≤ T ≤ 140 °C. This crossover temperature corresponds to the order-disorder temperature (T_{ODT}). In comparison, higher order maxima had been observed in the profile at 130 °C in Figure 1-2, which means SIS-56 at 130 °C is still in the ordered state. Thus, from both Figures 1-2 and 1-3 the T_{ODT} was evaluated to be between 130 °C < T ≤ 140 °C.

It should be noted that a small curvature or a weak deviation from the linearity of I^{-1} with respect to T^{-1} is seen in the plot of I^{-1} vs T^{-1} at T > 130 °C (broken curve in Figure 1-3). This confirms findings of Bates et al.[34,35] and Almdal et al.[36] on other block copolymers. The curvature or the deviation

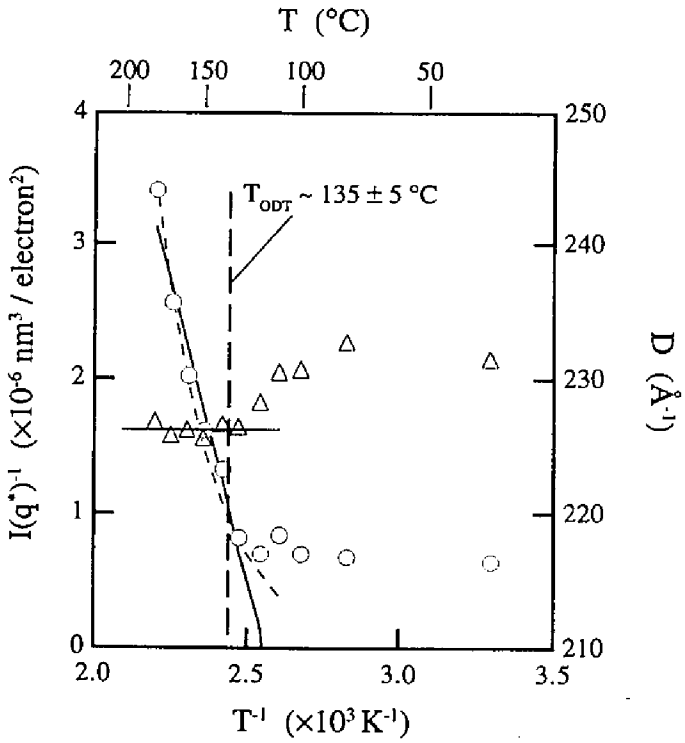

Figure 1-3. Inverse SAXS intensity (O) and characteristic size, D (Δ), vs inverse temperature plotted to determine the ODT, where $q^* = 0.278$ nm^{-1}.

from the linearity is attributed to the finite size effect proposed by Fredrickson and Helfand.[1] However, it is emphasized that this effect is small compared to the deviation from linearity at T ≤ 130 °C, i.e., below ODT.

1-3-2. ODT Determination by Rheometry

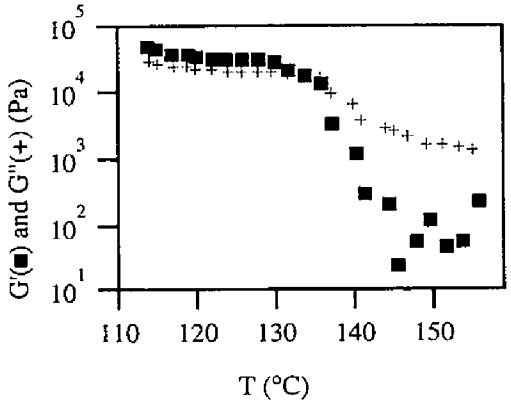

Figure 1-4. First heating curve (2 K/min) at ω = 0.1 rad/s.

We observed the occurrence of the ODT by two types of dynamic mechanical experiments. A convenient first test was to heat the microphase-separated sample gradually (2 K/min) in the rheometer while G' and G" were measured at a low constant frequency (ω = 0.1 rad/s) in the linear viscoelastic region, as shown in Figure 1-4. The elastic moduli were found to drop significantly during heating from 130 to 140 °C, indicating the nascence of the ODT. As the temperature increased above 135 °C, G' dropped by several orders of magnitude as the disordered phase was developing. By use of this technique, it was a good assessment that the ODT occurred near 135 °C.

Figure 1-5 shows reduced master curves of the elastic moduli over several decades of frequency determined from isothermal frequency sweeps shifted to a reference temperature of 160 °C. We assume that the high-frequency G' and G" were unaffected by the order-disorder transition and that they could be used to determine the horizontal and vertical shift factors a_T and b_T as plotted in Figure 1-6. The vertical shift was very small ($b_T \approx 1$). Low-frequency moduli, for instance at ω = 0.1 rad/s as used in Figure 1-4, changed by about 2-3 orders of magnitude. From Figure 1-5, it is obvious

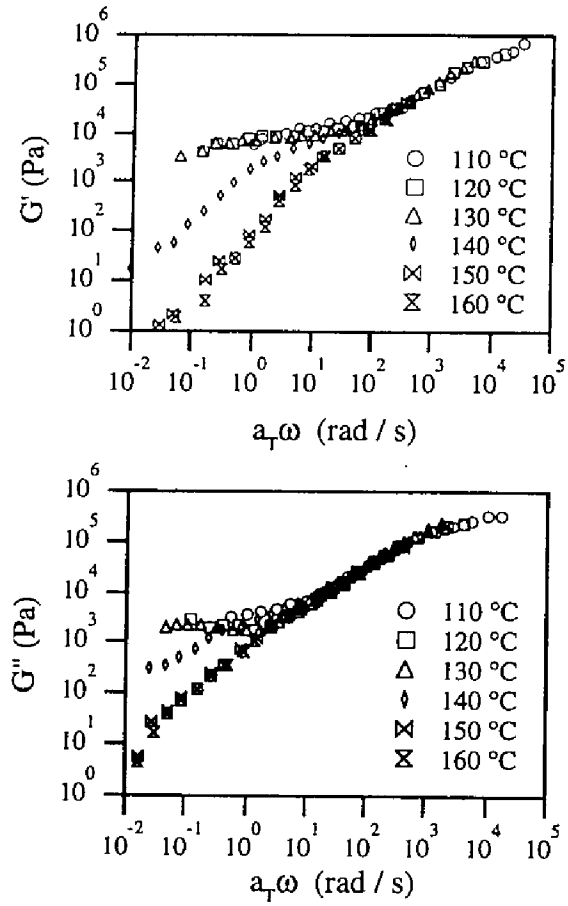

Figure 1-5. Master curves for heating with T_{ref} = 160 °C. Slopes of 2 and 1 are indicated as a reference in the low-frequency region.

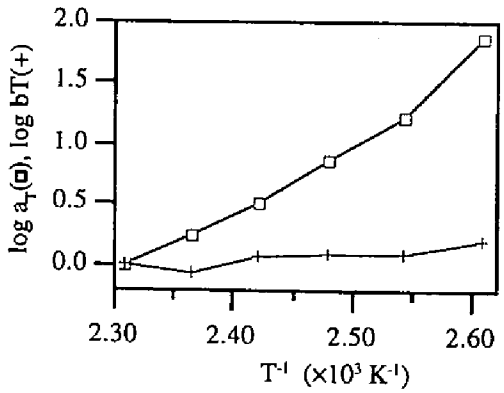

Figure 1-6. Shift factors, a_T and b_T vs inverse temperature, T_{ref} = 160 °C.

that there is a material characteristic frequency (~100 rad/s for SIS-56 at 160 °C) below which a typical drop of G' and G" due to the ODT can clearly be seen. Therefore, most emphasis was placed here on the low-frequency G' and G" data. The microphase-separated sample (top curve in each of the graphs of Figure 1-5) has relaxation modes over a wide frequency range, much beyond the experimentally accessible range. The disordered sample (bottom curve in each of the graphs of Figure 1-5) has a characteristic relaxation time which is fairly short (~10^{-4} s). Its terminal zone dominates nearly half the accessible frequency window. The entanglement plateau, which is typical for melts of high molecular weight, begins to show at the highest frequencies in Figure 1-5.

1-3-3. Ordering Processes Encountered by Quenching from Disordered State to Ordered State

1-3-3a. Rheological Observation

A sample was heated to 160 °C and then cooled through the T_{ODT} at a rate of -2 K/min. The low-frequency G' and G" were measured as a function of temperature (Figure 1-7). The cooling curve significantly differs from the heating curve as one sees by comparing Figures 1-7 and 1-4. The ordering process as observed by low-frequency G' and G" does not appear to be instantaneously reversible but is orders of magnitude slower than the disordering process.

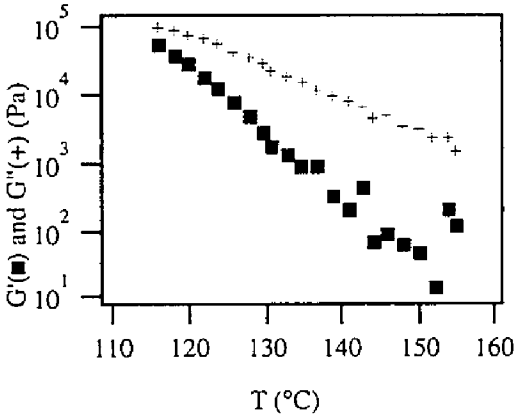

Figure 1-7. Cooling curve (-2 K/min) at ω = 0.1 rad/s.

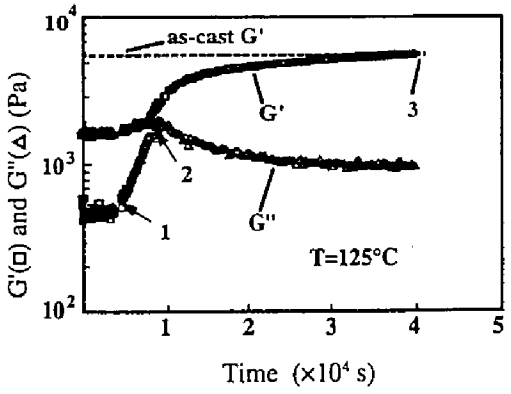

Figure 1-8. Isothermal time sweep at T = 125 °C and ω = 0.1 rad/s after heating above ODT. Isothermal frequency sweeps were taken after 70 min, 160 min, and 11 h as marked by 1, 2, and 3, respectively.

In a separate annealing experiment, samples were rapidly cooled through ODT and then held isothermally at 125 °C. G' and G" at ω = 0.1 rad/s were monitored (Figure 1-8) for 11 h until they finally returned to their initial values of the as-cast samples. In the same experiment, three frequency sweeps were performed at selected times, as indicated by the arrows on Figure 1-8: after 70 min, 160 min, and 11 h. The corresponding data in Figures from 1-9 to 1-11 clearly show the slow recovery of the low-frequency moduli over time.

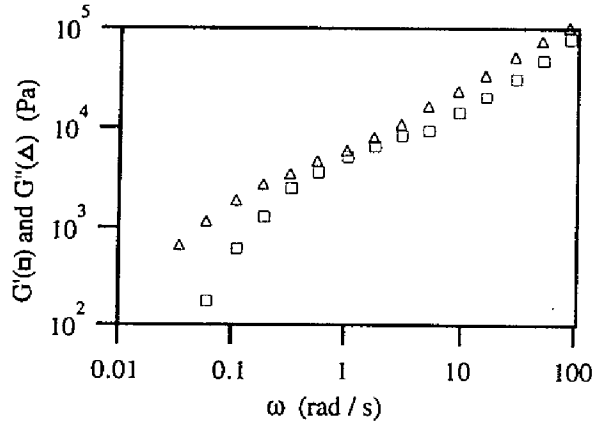

Figure 1-9. Frequency sweeps at T = 125 °C after anealing for 70 min.

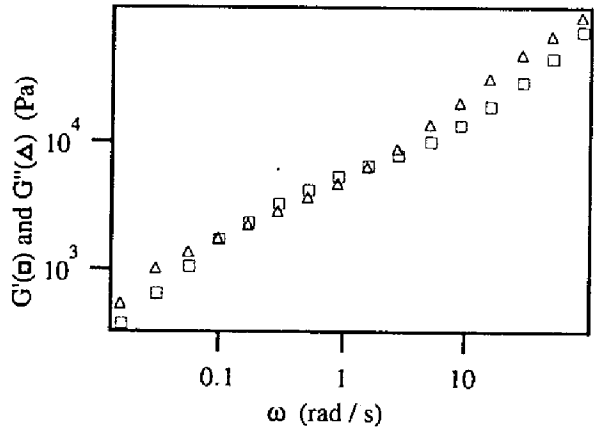

Figure 1-10. Frequency sweeps at T = 125 °C after anealing for 160 min.

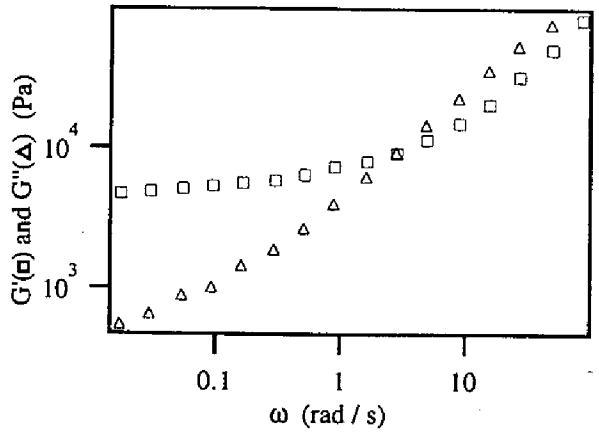

Figure 1-11. Frequency sweeps at T = 125 °C after anealing for 11 h.

1-3-3b. SAXS Observation

SAXS measurements started out with preheating an as-cast film to 125 °C for 30 min. Subsequently, the sample was heated to 160 °C and annealed for 30 min, where the SAXS profile was measured for 1 h. Then, the sample was quenched to 125 °C, by quickly transferring the cell to another temperature enclosure at 125 °C. Temperature equilibrium was attained in less than 1 min. The SAXS profiles were measured during the ordering process at 125 °C as a function of time; see Figure 1-12.

Figure 1-12 shows the profiles measured from 0 to 20 min (curve 2), from 13 to 14 h (curve 3) after quenching, together with the profile measured in situ at 125 °C after heat-treating the as-cast film at 125 °C for a long time so as to achieve equilibrium (curve 1), and that at 160 °C (curve 4). Although not shown here, the profiles obtained from 40 to 60 min and from 2 to 3 h after quenching were identical to that shown by curve 2. The time changes of the peak intensity and the half-width at half-maximum (hwhm) for the scattering maximum after the quenching from 160 to 125 °C are given in Figure 1-13, where the solid lines show the corresponding quantities after heat-treating the as-cast film at 125 °C. The results shown in Figures 1-12 and 1-13 clearly indicate that the microdomain formation and the lattice ordering as observed by SAXS are quite rapid, occurring within the first time frame of 20 min. The directions of the fluctuations and the lattice planes are random. A slight broadening of the scattering profiles and a decrease of the peak intensity occurred very gradually after 3 h. The origin of this gradual change of the scattering profiles is not understood at present, but it might be related to a long-range reorganization into the grain structure which was probed by rheology. The sample morphology does not seem to return to the as-cast (+ annealed) state, at least not during the short experimental time.

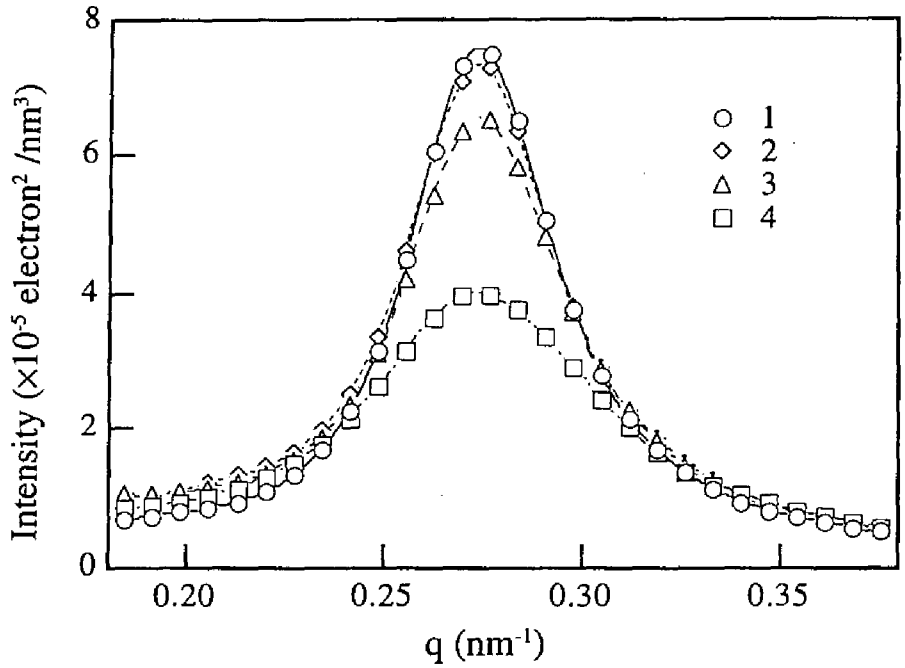

Figure 1-12. SAXS profiles at T = 125 °C as a function of time after quenching from 160 °C.

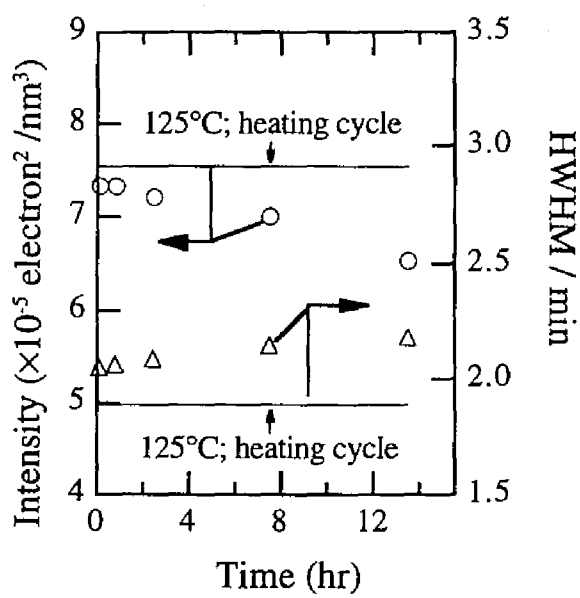

Figure 1-13. Time changes of the intensity maxima (○) and the half-width at half-maximum (hwhm, in units of minutes in θ) (△) for 1-h SAXS scattering profile shown in Figure 1-12. Two horizontal reference lines show the intensity maxima and hwhm for SAXS profiles measured at 125 °C during the heating cycle of the as-cast specimens.

1-4. Discussion

1-4-1. ODT Determination during Heating

The ODT gave rise to gross changes in the elastic modulus near the T_{ODT}. During the transition, the time-resolved low-frequency rheological properties changed so rapidly that even "point" measurements were affected. The magnitude of this experimental problem can be estimated with the mutation number[37]

$$N_{mu} = \Delta t \frac{1}{g} \frac{\partial g}{\partial t} \tag{1-7}$$

g stands for the quantity to be measured in the transitory experiment and $\partial g/\partial t$ is the rate of change of this quantity (here, g stands for either G' or G"). $\Delta t \simeq 2\pi/\omega$ is the experimental time for obtaining a single data point. For an acceptable measurement, the mutation number should be 0.1 or smaller for both G' and G", which is not the case during the temperature-induced transition. This is the origin of the large scatter in both the G' and G" transition data (Figure 1-4). At high temperatures, beyond the T_{ODT}, the rate of change was small and the G" data became acceptable again while G' was orders of magnitude smaller than G" so that it could not be resolved any more. The scatter in the G' data (not the G" data) expresses this limited resolution of the experiment.

Figure 1-5 shows the linear viscoelastic behavior both above and below the T_{ODT}. G' has a plateau region at intermediate frequencies as long as the polymer is microphase-separated. This plateau is not due to molecular entanglements (which would remain when heating above ODT), but it is

indicative of a "grain network structure" formed by continuity of the cylindrical microdomains through the grain boundary region. Above the ODT, the low-frequency properties are characteristic of a liquid-like behavior. Both the grain network and the domains are dissolved into a disordered melt above the T_{ODT}.

In the disordered state (bottom curve in each of the graphs of Figure 1-5), the entanglement behavior of the PI midblock seems to be drastically altered by the polystyrene end blocks. The polyisoprene midblock of SIS-56, with an average molecular weight of ~ 42 000, has an entanglement behavior which differs substantially from that of pure PI chains of the same length. A difference in plateau modulus is not noticeable (not enough high-frequency data on SIS-56 to confirm), but the molecular relaxation dynamics is somehow changed so that the entanglement region is shifted to much higher frequencies or shorter times. A pure chain of PI with the same molecular weight would have a characteristic relaxation time ~100 times larger than that of SIS-56.

The second special feature of the disordered SIS-56 melt is the broadening of the spectrum between about $10^2 < \omega < 10^4$ s^{-1}. The spectrum of a nearly monodisperse homopolymer melt, such as the disordered SIS-56, would be cut off at the beginning of the entanglement plateau,[38] while the disordered SIS-56 has been observed to have additional slow modes. The characteristics of these slow modes will be explored further in the near future.

The disordering process as observed by SAXS was also found to be rapid, and the dissolution of the microdomains was found to occur within minutes after a temperature jump from an ordered state to a disordered state for other block copolymer systems.[3,6,7,38] The SAXS results are in good agreement with the rheological ODT determination as long as the ODT is

determined by heating.

1-4-2. Ordering Process during Cooling

After quenching below the T_{ODT}, sufficient annealing must be performed to establish the fully developed grain network structure. The required annealing time is shortest at an intermediate annealing temperature, since the molecular mobility is decreased with decreasing temperature while the thermodynamic driving force for microphase separation increases with decreasing temperature, and vice versa. 125 ° C was found to be a suitable intermediate temperature for our sample when annealing at rest. The dynamic moduli grew in a sigmoidal curve (Figure 1-8) which resembles a nucleation and growth process, similar to crystallization kinetics, which has been theoretically developed to describe the ordering process as a homogeneous nucleation and growth process for symmetric diblocks.[39] Rosedale and Bates[16] also observed such rheological behavior using a diblock copolymer.

The ordering process seems to have two different time constants, a short characteristic time for the structure which is probed by SAXS and a long characteristic time for the structure which is probed by rheology. The ordering as observed by SAXS is completed within the first 20 min after quenching while the ordering as observed by rheology requires ~11 h. The apparent difference reflects different length scales at which the two methods tend to detect space-time organization of block copolymers in the microphase separation process. The SAXS data are more sensitive to the microdomain formation (local concentration fluctuations), i.e. time evolution of the order parameter in the length of the lattice parameter. On the other hand, the rheology is more sensitive to the grain network formation and annihilation of defects in the grain boundaries. The two data sets combined give a picture

in which the microdomain formation occurs rapidly on the domain scale, but the long-range structure reorganization resulting in the grain network formation requires a much longer time scale.

Independently, and in parallel to this study, Schuster and Stühns[40] also observed two time scales for the structuring, however, for a low molecular weight diblock. This suggests that the observed phenomenon is of a more general significance.

1-5. Conclusion

SAXS and rheology probe the morphology at very different length scales. SAXS measurements provide detailed structural information on a 10-nm scale. Low-frequency dynamic mechanical measurements are mostly affected by the 1-μm-scale grain morphology. Rheology locates the transition somewhere between 130 and 140 °C in good agreement with the SAXS results. The ODT can best be measured in a heating scan since the disordering occurs rapidly on all length scales. On the other hand, the ordering transition depends on the size of the structure and it will appear delayed depending on the scale of observation. During the quiescent ordering process (no flow) at 125 °C, SAXS measurements detected well-separated microphase domains within 20 min (first frame) while G' and G" show that formation of equilibrium grain morphology takes many hours.

The drop of low-frequency G' and G" values at ODT is much larger for SIS-56 than for diblock copolymers as investigated in other laboratories. Otherwise, the ODT has a very similar effect on relaxation dynamics and the involved time scales. This is rather surprising since the underlying morphologies for SIS-56 and for diblocks are very different.

References

(1) Fredrickson, G. H., Helfand, E. *J. Chem. Phys.* **1987**, *87*, 697

(2) Roe, R. Y.; Fishkis, M.; Chang, J. C. *Macromolecules* **1981**, *14*, 1091.

(3) Hashimoto, T.; Tsukahara, Y.; Kawai, H. *J. Polym. Sci., Polym. Lett.* **1980**, *18*, 585.

(4) Hashimoto,T.; Tsukahara,Y.; Kawai,H. *Macromolecules* **1981**, *14*, 708.

(5) Hashimoto, T.; Shibayama, M.; Kawai, H.; Watanabe, H.; Kotaka, T. *Macromolecules* **1983**, *16*, 361.

(6) Hashimoto, T.; Kowsaka, K.; Shibayama, M.; Kawai, H. *Macromolecules* **1986**, *19*, 750, 754.

(7) Hashimoto, T.; Suehiro, S.; Shibayama, M.; Saijo, K.; Kawai, H. *Polym. J. (Tokyo)* **1981**, *13*, 501.

(8) Hashimoto,T.; Shibayama,M. ; Kawai,H. *Macromolecules* **1983**, *16*, 1093.

(9) Chung, C. I.; Gale, J. C. *J. Polym. Sei., Polym. Phys. Ed.* **1976**, *14*, 1149.

(10) Guinlock, E. V.; Porter, R. S. *Polym. Eng. Sei.* **1977**, *17*, 535.

(11) Chung, C. I.; Lin, M. I. *J. Polym. Sci., Polym. Phys. Ed.* **1978**, *16*, 545.

(12) Widmaier, J. M.; Meyer, G. C. *J. Polym. Sci., Polym. Phys. Ed.* **1980**, *18*, 2217.

(13) Kraus, G.; Hashimoto, T. *J. Appl. Polym. Sci.* **1982**, *27*,1745.

(14) Watanabe, H.; Katoka, T.; Hashimoto, T.; Shibayama, M.; Kawai, H. *J. Rheol.* **1982**, *26*, 153.

(15) Bates, F. S. *Macromolecules* **1984**, *17*, 2607.

(16) Rosedale, J. H., Bates, F. S. *Macromolecules* **1990**, *23*, 2329.

(17) Bates, F. S.; Hartney, M. A. *Macromolecules* **1986**, *19*, 2892.

(18) Han, C. D.; Baek, D. M., Kim, J. K. *Macromolecules* **1990**, *23*, 561

(19) Koberstein, J. T.; Russell, T. P.; Walsh, D. J., Pottick, L. *Macromolecules* **1990**, *23*, 877.

(20) Stühn, B.; Mutter, R.; Albrecht, T. *Eur. Lett.* **1992**, *18*, 427.

(21) Keller, A.; Pedemonte, E.; Willmouth, F. M. *Nature* **1970**, *225*, 538.

(22) Suehiro, S.; Saijo, K.; Ohta, Y.; Hashimoto, T.; Kawai, H. *Anal. Chim. Acta* **1986**, *189*, 41.

(23) Fijimura, M.; Hashimoto, T.; Kawai, H. *Mem. Fac. Eng., Kyoto Univ.* **1981**, *43 (2)*, 224.

(24) Hendricks, R. W. *J. Appl. Cryst.* **1972**, *6*, 315.

(25) Baumgärtel, M.; Winter, H. H. *Rheol. Acta* **1989**, *28*, 511 *J.Non-Newtonian Fluid Mech.* **1992**, *44*, 15. Winter, H. H.; Baumgärtel, M.; Soskey, P. R. In *Techniques in Rheological Measurement*; Collier, A. A., Ed.; Chapman & Hall: London,1993.

(26) Mori, K.; Hasegawa, H.; Hashimoto, T. *Polym. J. (Tokyo)* **1986**, *17*,799.

(27) Leibler, L.; Benoit, H. *Polymer* **1981**, *22*, 201.

(28) Leibler, L. *Macromolecules* **1980**, *13*, 1602.

(29) de Gennes, P.-G. *Scaling Concepts in Polymer Physics*; Cornell University Press: Ithaca, NY, 1979.

(30) LeGrand, A. D.; LeGrand, D. G. *Macromolecules* **1979**, *12*, 450.

(31) Mori,K.; Hasegawa,H.; Hashimoto, T. *Polym.Prepr.Jpn.* **1984**, *33*, 2267.

(32) Benmouna, M.; Benoit, H. *J. Polym. Sci., Polym. Phys. Ed.* **1983**, *21*, 1227.

(33) Hashimoto, T. In *Thermoplastic Elastomers*; Legge, N. R., Holden, G., Schroeder, H. E., Eds.; Hanser: Munich, 1987.

(34) Bates, F.; Rosedale, J. H.; Fredrickson, G. H.; Glinka, C. *J. Phys. Reu. Lett.* **1988**, *61*, 2229.

(35) Bates, F;- Rosedale, J. H.; Fredrickson, G. H. *Phys. Reu. Lett* **1990**, *92*, 6255.

(36)Almdal, K.; Koppi, K. A.; Bates, F. S.; Mortensen, K. J. *Macromolecules* **1992**, *25*, 1743.

(37) Winter, H. H., Morganelli, P.; Chambon, F. *Macromolecules* **1988**, *21*, 532.

(38) Baumgärtel, M.; Schausberger, A.; Winter, H. H. *Rheol. Acta* **1990**, *29*, 400.

(39) Fredrickson, G. H.; Binder, K. *J. Chem. Phys.* **1989**, *91*, 7265.

(40) Schuster, M.; Stühn, B., draft paper 1992.

Chapter 2

Paracrystal Analyses of a Lamellar Microdomain Structure by Small-Angle X-Ray Scattering

2-1. Introduction

As described in Chapter 1, block copolymers form highly regular microdomain structures in the ordered state.[1] The morphology (size and shape of the microdomains) depends on the molecular weight, the composition, temperature, thermal history and the ordering process.[2,3,4,5,6] Since the typical size of the microdomains is of the order of 10 nm, small-angle X-ray scattering (SAXS) and neutron scattering (SANS) are useful for the structure analyses as shown in Chapter 1.

In Chapter 1, it was shown that the grain boundaries, i.e., the defects in the crystalline lattice formed by the microdomains affect the mechanical property. In Chapter 2, I pick up a lamella-forming block copolymer and investigate its spatial arrangement as evaluated by uniformity of the microdomains in the directions perpendicular and parallel to the interface. I characterize in detail the distribution of the lattice spacing and that of the single domain thickness by SAXS as well as their persistence lengths by TEM. The SAXS profile was thoroughly analyzed by one-dimensional paracrystal model with a uniaxial orientation with respect to the film normal which will be also described in this chapter.

The paracrystal model I describe in this chapter is also used for analyzing the SAXS data in Section 2-2, the experimental methods in Section 2-3, and results and discussion in Section 2-4.

2-2. *Paracrystal Model for Lamellar Microdomains and its Scattering Formulae*

The alternating lamellar morphology of A-B type diblock polymers, e.g. A and B being the domains comprising polystyrene (PS) and poly(ethylene-*alt*-propylene) PEP, is represented by an assembly of alternating disc-like particles of A and B. In Figure 2-1 the spatial electron density profile $\rho(r)$ along the assembly axis is shown where ρ_A and ρ_B

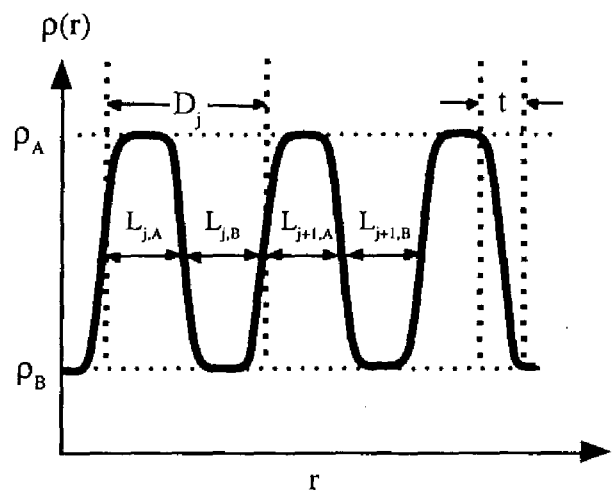

Figure 2-1. Schematic representation of the spatial distribution of the electron density $\rho(r)$ in a direction normal to the lamellar interface.

designate, respectively, average electron densities of A and B lamellae. This structure can be regarded as a one-dimensional paracrystal. The diameter or the lateral persistence length W of the lamellae is found to be much larger than the average thickness L_A of one of the lamellae A or the average lamellar spacing D for the typical lamellar microdomains of the block copolymers in the strong segregation limit.[3]

In the earlier work,[7] the scattering formula for the lamellar microdomains was derived by extending the one-dimensional paracrystal

theories of scattering originally proposed by Hosemann et al.[8] and refined by Blundell et al.[9] and others to the case in which the assembly axis of the discs is preferentially oriented with respect to the film normal. In the case when W » D, the observed scattered intensity along the film normal, J(h), is given by

$$J(h) \simeq h^{-2} I_p(h), \tag{2-1}$$

where h is the magnitude of the scattering vector **h** defined by $h = (4\pi/\lambda)\sin\theta$, λ and 2θ being the wavelength of the X-rays and the scattering angle, respectively. In eq 2-1, h^{-2} is the Lorentz factor associated with the orientation distribution of the assembly of the discs[7] and $I_p(h)$ is the scattering per single lamellar assembly along its axis, the axis being assumed to be normal to the flat interface of the disc. Note that the relationship between $I_p(h)$ and J(h) given by eq 2-1 is valid, irrespective of the degree of orientation.[7,10] $I_p(h)$ is given by

$$I_p(h) \simeq \langle |f|^2 \rangle - |\langle f \rangle|^2 + |\langle f \rangle|^2 (Z + I_C/N), \tag{2-2}$$

where f is the scattering amplitude of one of the discs A (PS domain) given by

$$f = \{[\sin(hL_A/2)]/(hL_A/2)\} \exp(-\sigma^2 h^2/2) \tag{2-3}$$

and Z is the lattice factor describing the statistical character in the spatial distribution of the centers of the discs. Using Hosemann-Bagchi paracrystal distance statistics,[8] Z is given by

$$Z = (I - |F|^2)/[1 - 2|F|\cos(h\bar{D}) + |F|^2] \quad (2\text{-}4)$$

In eq 2-3, L_A is the thickness of the A disc and σ is a parameter characterizing the thickness of the diffuse boundary of the disc,[11,12] $\sigma = 0$ corresponding to the sharp interface. The characteristic interfacial thickness,[3,4] t_j, is defined as

$$t_j = (2\pi)^{1/2}\,\sigma \quad (2\text{-}5)$$

and corresponds to the integral breadth of the smoothing function which characterizes the density profile across the interface. The angular bracket in eq 2-2 indicates an average of f or $|f|^2$ with respect to a distribution function $P_L(L_A)$ for the disc thickness L_A,

$$P_L(L_A) = (2\pi\sigma^2_{L_A})^{-1/2} \exp[-(L_A - \bar{L}_A)^2/2\sigma^2_{L_A}], \quad (2\text{-}6)$$

where $\bar{L}_A$ and σ_{L_A} are the average thickness and its standard deviation. In eq 2-4, the factor |F| is given by

$$|F| = \exp(-g^2\bar{D}^2h^2/2), \quad (2\text{-}7)$$

where g is the lattice distortion factor, given by

$$g = \Delta D/\bar{D}. \quad (2\text{-}8)$$

$\bar{D}$ and ΔD are the average lattice spacing (interdisc distance) and corresponding standard deviation, respectively. The distance statistics assume a Gaussian function for a distribution of D,

$$P_D(D) = (2\pi\Delta D^2)^{-1/2} \exp[-(D - \bar{D})^2/2\Delta D^2], \quad (2\text{-}9)$$

In eq 2-2, I_c is the zeroth-order scattering intensity, reflecting scattering from the assembly as a whole embedded in a medium, and N is the number of discs in the assembly. As in earlier work,[13] we assume the following distribution function $P_N(N)$ for N:

$$P_N(N) = \{\exp[-(N - \bar{N})^2/2\sigma_N^2]\} \times \Big\{ \sum_{N=1}^{2\bar{N}-1} \exp[-(N - \bar{N})^2/2\sigma_N^2]\Big\}^{-1}, \quad (2\text{-}10)$$

where $\bar{N}$ and ρ_N are the average number N and the corresponding standard deviation, respectively.

Since $P_D(D)$ and $P_L(L_A)$ are independent and Gaussian, the standard deviation σ_{L_B} for the B disc is given by

$$\sigma^2_{L_B} = \Delta D^2 - \sigma^2_{L_A} \quad (2\text{-}11)$$

Note that the volume fraction of K disc is given by

$$\phi_K = \bar{L}_K / \bar{D} \; (K = A \text{ or } B). \quad (2\text{-}12)$$

Therefore one can determine such structural parameters as $\bar{D}$, g, $\bar{L}_A$, σ_{L_A}, t_1, $\bar{N}$ and σ_N by best fit of the experimental and theoretical curves. In this work, a line collimation rather than a point collimation was used to obtain the SAXS profiles. The smeared SAXS intensity profiles along the film normal measured with the slit X-ray image parallel to the film surfaces were compared with the corresponding theoretical smeared intensity $\tilde{I}(h)$. From the best fit of the experimental and theoretical smeared scattering profiles, we attempted to obtain the characteristic parameters of the unique microdomains.

2-3. Experimental Section

2-3-1. Specimen

The polystyrene-*block*-poly(ethylene-*alt*-propylen) (SEP) used is the diblock copolymer of PS and PEP, which was obtained by the hydrogenation of polystyrene-*block*-polyisoprene diblock copolymer. The specimen SEP-34/130 has $M_n = 130 \times 10^3$, $M_w / M_n = 1.5$ and $\phi_{PS} = 0.34$. Since the content of 1,4-linkage of the precursory polyisoprene chain was found to be close to 100%, the PEP chain, which was obtained by the hydrogenation of the polyisoprene chain, is expected to be an almost perfect alternating copolymer of ethylene and propylene comonomer units.

Thin polymer films of about 50 μm thickness was obtained from ca. 5 wt.% toluene solution in the same manner as described in Chapter 1. In this chapter, the as-cast film was used for the SAXS measurement without heat treatment.

2-3-2. Small-Angle X-ray Scattering

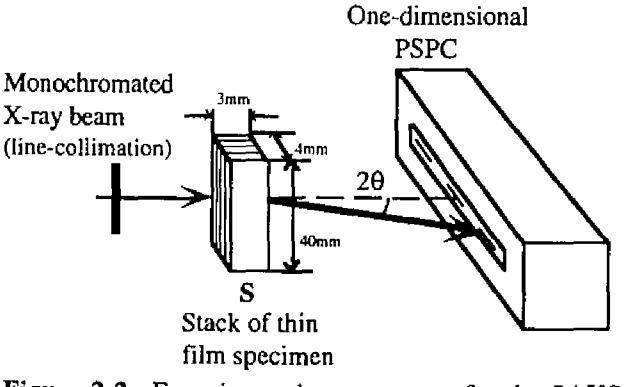

Figure 2-2. Experimental arrangement for the SAXS measurements showing schematically one-dimensional PSPC and the line-focused X-ray image parallel to the surface of a stack of thin-film specimens. The scattering intensity distribution perpendicular to the film surface is measured (designated as "edge configuration").

SAXS measurements were performed with the apparatus described in Chapter 1.[14] The SAXS profiles were measured by the incident beam with the line-shaped image for the edge configuration, i.e., the incident X-ray beam was parallel to the film

surface and the scattering intensity distribution perpendicular to the film surface was measured; see Figure 2-2.

2-3-3. Transmission Electron Microscopy

Transmission electron microscopy (TEM) was conducted on the ultrathin sections of ca. 50 nm thickness sliced from the as-cast specimen using a Reichert-Jung Ultracut E ultramicrotome with a cryogenic unit FC 4E. The thin sections were picked up on 400-mesh copper grids and stained with ruthenium tetraoxide (RuO_4) vapor prepared by the method reported by Montezinos et al.[15] TEM was performed at 100 kV with a Hitachi H-600 transmission electron microscope using a tilt specimen holder.

2-4. Results and Discussion

Figure 2-3 shows a typical TEM micrograph which clearly exhibits alternating microdomains of the lamella comprising the PS block chains and that comprising the PEP block chains. The PS lamellae are selectively stained and appear as a dark phase under TEM. We can consider the lamellar morphology as a one-dimensional assembly of the PS lamellae in the medium of the PEP matrix. Close examination of the micrograph revealed the volume fraction of the PS lamella, ϕ_{PS}, to be about 0.33.

Figure 2-3. Transmission electron micrograph of an as-cast film of SEP-34/130. The polystyrene domain is selectively stained by ruthenium tetraoxide.

The observed SAXS

profile of the as-cast film of SEP-34/130 at room temperature is shown in Figure 2-4 by the data points where the absolute smeared scattered intensity was plotted semilogarithmically as a function of scattering vector **h**. The

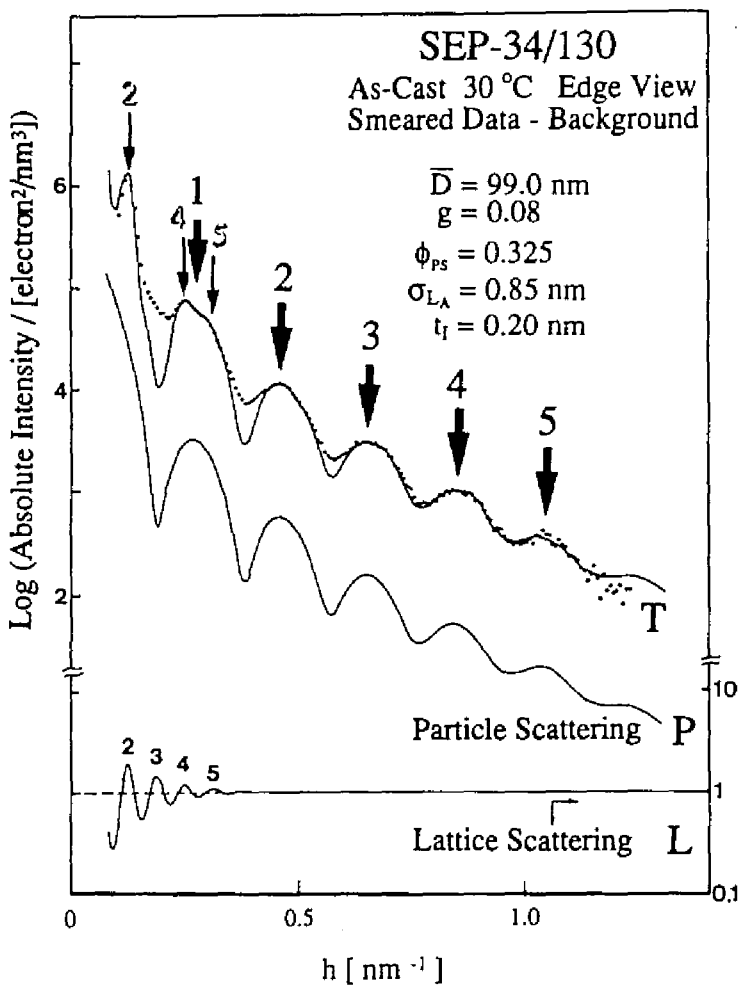

Figure 2-4. The observed SAXS profile for SEP-34/130 (data points), the best-fitted calculated profile (solid profile marked *T*) being obtained using the values for the structural parameters as indicated in this figure. The particle scattering factor (*P*) and the lattice scattering factor (*L*) are also included in the figure. The profile for the particle scattering factor is shifted along the ordinate to avoid overlap. The scattering maxima labelled by thin arrows numbered 2, 4 and 5 are due to the second-, fourth-, and fifth-order Bragg diffraction maxima from the lattice, while those labelled by thick arrows numbered 1 to 5 are due to the first- to fifth-order maxima from the single PS lamellae.

solid curves in Figure 2-4 will be discussed later.

The profile was measured by the one-dimensional PSPC under the following conditions. The incident X-ray beam with a line-shaped flux was irradiated parallel to the film surfaces (S) of a stack of thin-film specimens, and the scattered intensity from the stacks in a direction normal to the film surface was detected by the PSPC as sketched in Figure 2-2. Scattering experiments which were conducted separately with a point-focused X-ray beam and a two-dimensional detector with a beam parallel to the film surfaces as showed in Figure 2-2 a high degree of orientation of the lamellar interfaces parallel to the film surfaces, as reported for the lamellar microdomains observed for the solvent-cast films of polystyrene-*block*-polyisoprene diblock copolymers.[3, 13, 16] Thus the slit-height smearing does not strongly perturb the scattered intensity profile.

The experimental SAXS profile exhibits several peaks over the h range covered in this experiment ($0.10 < h < 1.20$ nm^{-1}). However, the profile appears to be quite different from that observed for typical lamellar microdomains which shows a series of higher-order scattering maxima at positions of integer multiples of that of the first-order maximum. It comprises the maxima labelled by the thin arrows numbered 2, 4 and 5 and those labelled by the thick arrows numbered 1 to 5 in Figure 2-4.

From a TEM investigation, the average lamellar spacing $\bar{D}$ was estimated to be ca. 100 nm. Thus the peak at $h = 0.126$ nm^{-1} (labelled with a thin arrow numbered 2) corresponds to the second-order maximum of the lamellar identity period $\bar{D}$ and those at $h = 0.248$ and 0.308 nm^{-1} (labelled by thin arrows numbered 4 and 5, respectively) to the fourth- and fifth-order maxima, respectively. Then the broad peaks labelled with the thick arrows numbered 1 to 5 observed in the region $h > 0.27$ nm^{-1} may be interpreted as

a series of higher-order maxima arising from the single lamellar particles with a narrow size distribution.

In order to interpret the origin of the several peaks of SEP-34/130, numerical calculation of the scattering profile was performed using the paracrystal theory. The solid curve marked T represents the best-fitted calculated profile, while those marked L and P represent, respectively, the lattice scattering factor Z, given by eq 2-4, and the particle scattering factor $\langle |f|^2 \rangle$, given by eq 2-3 and eq 2-6. In the numerical analysis of the scattering, the lamella composed of PS chains was taken as an A-type lamella and the lamella composed of PEP chains as a B-type lamella or a medium for A lamellae. It clearly shows that the theoretical profile based on the one-dimensional paracrystal model can describe the observed scattering profile well. The best fit yields such structural parameters as $\overline{D}$ = 99.0 (5) nm, ϕ_{PS} = 0.325 (5), g = 0.080 (5), $\sigma_{L_A} = \sigma_{PS}$ = 0.85 (5) nm, t_1 = 0.20 (5) nm, $\overline{N}$ = 10 and σ_N = 5, where ϕ_{PS} is the volume fraction of PS lamellae and σ_{PS} is the standard deviation for the thickness distribution of PS lamellae. Thus it turns out that the numerical analysis based on the one-dimensional paracrystal is quite useful for characterizing the lamellar microdomain. The values $\overline{N}$ and σ_N which primarily affect the zeroth-order scattering were not assessed with high accuracy because the intensity data at $h < 0.10$ nm^{-1} cannot be rigorously evaluated.

Comparisons of the theoretical profiles T, P and L with the experimental profile clearly show that the several broad scattering maxima appearing in the region $h > 0.27$ nm^{-1} and marked by the thick arrows numbered 1 to 5 in Figure 2-4 are attributed to the particle scattering of a single lamella. These maxima appear as a consequence of the following two factors: (i) the lattice factor is damped out to unity at larger h values (i.e. $h > 0.38$ nm^{-1}) because of

the large paracrystal distortion factor g ($\equiv \Delta D/\overline{D} = 0.08$ or $\Delta D = 7.92$ nm); and (ii) the maxima due to the single particle persist up to high h values because of its small thickness distribution as manifested by $\sigma_{PS} / \overline{L}_{PS} = 0.02$ or $\sigma_{PS} = 0.80$ nm, where $\overline{L}_{PS}$ is the average thickness of PS lamellae given by $\overline{D}\phi_{PS} = 32.2$ nm.

The volume fraction $\phi_{PS} = 0.325$ (5) determined by paracrystal analysis is of very high accuracy since the determination of $\overline{D}$ and $\overline{L}_{PS}$ itself is of high accuracy owing to the existence of the corresponding multiple-order diffraction maxima. This value of ϕ_{PS} agrees quite well with that estimated ($\phi_{PS,vol}$) by volumetric consideration of the SEP block copolymer assuming a complete segregation of PS and PEP into corresponding lamellar microdomains. The value of $\phi_{PS,vol}$ was estimated using the following equation, together with the weight fraction of PS, w_{PS}:

$$\phi_{PS,vol} = (w_{PS}/\rho_{PS})/[w_{PS}/\rho_{PS} + (1 - w_{PS})/\rho_{PEP}] \qquad (2\text{-}13)$$

where the mass densities ρ_{PS} and ρ_{PEP} of pure PS and PEP are assumed to be 1.06 and 0.86 g cm^{-3}, respectively. The agreement between the two values ϕ_{PS} and $\phi_{PS,vol}$ implies that the solvent used (toluene) is nearly neutral for PS and PEP. The lamellar microdomain which is expected to be formed at polymer concentrations ϕ_P higher than a certain critical concentration, $\phi_{P,C}$ may be maintained with the effective volume fraction of PS relative to that of PEP kept nearly constant during solvent evaporation to result in the one in bulk.

Let us discuss an important and striking factor in the microdomain structure, as manifested by

$$\sigma_{PS}/\overline{L}_{PS} < \Delta D/\overline{D}, \qquad (14)$$

viz, the structure in which the polydispersity of the PS lamellae is smaller than that of their repeat distances. Figure 2-5 sketches four possible spatial arrangements of the alternating lamellae of A (the black PS domains) and B (the white PEP domains). Figure 2-5(*a*) represents both thicknesses of A and B lamellae and hence the interlamellar distance D has a narrow distribution with $\sigma_{L_A}/\overline{L}_A \cong \sigma_{L_B}/\overline{L}_B \cong g \ll 1$, so that both the particle and lattice factors maintain the scattering maximum up to high h values and the net scattering profile is expected to show the higher-order diffraction maxima due to the single lamellar spacing $\overline{D}$ at the scattering vector **h**, corresponding to integer multiples of that of the first order. In this case, it is expected to be difficult to assign the series of the maxima to those due to the single lamella. Figure 2-5(*b*) shows both A and B lamellae with a uniform size but with a coherently wavy character. If the persistence length W along the interface is much larger than $\overline{L}_A$, the domain structure observed at $hW \geq 1$ is expected to be essentially identical to that shown in Figure 2-5(*a*). The TEM micrograph shown in Figure 2-2 suggests that the domains have the property $W \gg \overline{L}_A$. It is an interesting problem, however, to explore the effects of the wavy domain with $W \cong \overline{L}_A$ on the scattering profile. Figure 2-5(*c*) corresponds to the situation encountered in this experiment where the domains satisfy the relationship eq 2-14. Even in this case the domains satisfy the condition $W \gg \overline{L}_A$. The greater distortion in the interlamellar spacing compared with the distortion of the thickness of the A lamella gives the observed unique scattering profile in which the Bragg diffraction maxima are damped faster than the scattering maxima due to the single lamellar particle A. Finally, Figure 2-5(*d*) shows the case where both L_A and D have the same distortions,

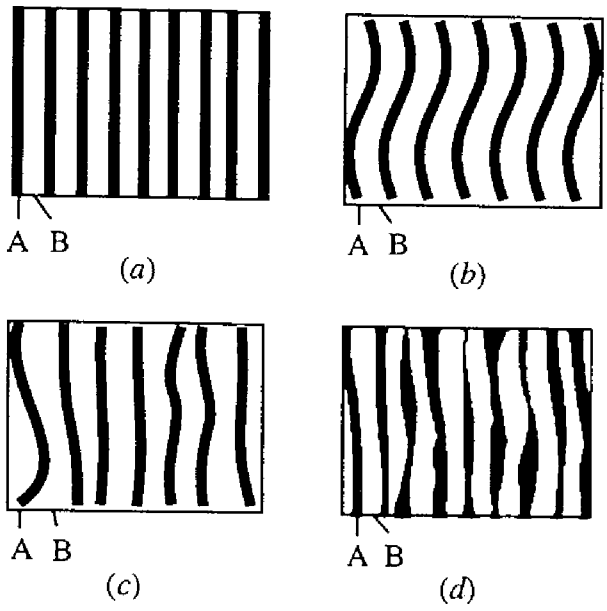

Figure 2-5. Various models for the alternating lamellae of *A* (PS lamellae) and *B* (PEP lamellae). (*a*) Both *A* and *B* lamellae are straight and have narrow thickness distributions. (*b*) *A* and *B* lamellae are coherently wavy and have narrow thickness distributions. (*c*) *A* and *B* lamellae are incoherently wavy and *A* lamellae have a narrow thickness distribution, giving rise to a broad thickness distribution of *B* lamellae. (*d*) *A* and *B* lamellae are incoherently wavy and polydisperse in thickness.

which gives rise to the scattering profile with both the Bragg diffraction maxima and the particle scattering maxima rapidly damped with increasing h. Thus, in this case, we also do not expect the existence of the scattering maxima from the single lamella.

In order to obtain an insight into the physical factors giving rise to the interesting structure associated with the relation given by eq 2-14, we investigated the effect of annealing the specimen on the structure parameter according to the following scheme. The as-cast film was heat treated at a temperature T_a for 30 min, followed by SAXS measurement at T_a for 1 h. After the measurement, the same film specimen was subjected to the heat treatment at a higher temperature of T_a' for 30 min, followed by SAXS measurement at T_a' for 1 h. This procedure was repeated. The temperatures

covered are 298 (as-cast), 393, 453, 483, 503 and 523 K. The SAXS profiles were subjected to paracrystal analysis, part of the results being summarized in Figure 2-6 where $\sigma_{L_A}/\overline{L}_A$ (for PS lamellae), $\sigma_{L_B}/\overline{L}_B$ (for PEP lamellae) and g ($\equiv \Delta D/\overline{D}$) are plotted as functions of the annealing temperature T_a.

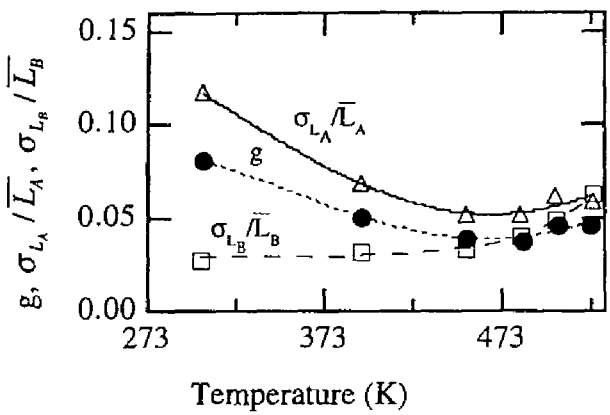

Figure 2-6. The temperature dependence of dimensionless quantities $\sigma_{L_A}/\overline{L}_A$, $\sigma_{L_B}/\overline{L}_B$, and g ($\equiv \Delta D/\overline{D}$).

It is clearly shown that annealing at 393 K, above T_g of PS lamellae, gives a large decrease in $\sigma_{L_B}/\overline{L}_B$ and hence g, but no change in $\sigma_{L_A}/\overline{L}_A$ indicating that the distribution in L_B was intensively relaxed by the annealing. Therefore a part of the large distortion of $\sigma_{L_B}/\overline{L}_B$ or g is due to a kinetic effect encountered during solvent evaporation. At higher temperatures, $T_a \geq$ 423K, the parameters tend to increase with T, which is believed to be a thermodynamic effect, i.e. due to a decrease in the segregation power.[1] Thus even in the regime where the system is close to thermodynamic equilibrium, there is a tendency for $\sigma_{L_A}/\overline{L}_A < \sigma_{L_B}/\overline{L}_B$, *viz*, the larger domain tends to fluctuate to a greater extent than the smaller domain, an observation which deserves further study.

2-5. Conclusion

Solvent-cast thin films (~50 μm) of a lamella-forming diblock copolymer (SEP-34/130) was studied in detail by SAXS. The SAXS profiles displayed a series of peculiar scattering maxima which cannot be ascribed to the higher-order diffraction maxima from the one-dimensional lattice of the regular lamellar structure. These SAXS profiles were analyzed by a one-dimensional paracrystal model with a preferential orientation. We obtained the results that these maxima are attributed to the higher-order scattering maxima of the particle scattering factor from single lamellar microdomains and that the relative standard deviation for the distribution of the polystyrene lamellar size is much smaller than that of the lamellar spacing. Thus the SAXS result was interpreted as being due to a bending distortion of the polystyrene lamella with a smaller thickness and a narrower thickness distribution than those of the poly(ethylene-*alt*-propylene) lamella. The unique structure gives rise to a situation where the oscillation of the particle factor with scattering vector **h** persists up to high h (magnitude of **h**) values while that of the lattice factor damps to unity at low h values. A study by transmission electron microscopy supported this result.

References

(1) Hashimoto, T. in *Thermoplastic Elastomers*; Ledge, N. R., Holden, G., Schroeder, H. E., Eds.; Hanser: Munich, New York, **1987**; p349.

(2) Hasegawa, H.; Tanaka, H.; Yamasaki, K.; Hashimoto, T. *Macromolecules* **1987**, *20*, 1651-1662.

(3) Hashimoto, T.; Shibayama, M.; Kawai, H. *Macromolecules* **1980** *13*, 1237-1247.

(4) Hashimoto, T.; Fujimura, M.; Kawai, H. *Macromolecules* **1980** *13*, 1660-1669.

(5) Molau, G. E. in *Block Polymers*; Aggawal, S. L., Ed.; Plenum Press; New York, **1970**; pp. 79-106.

(6) Sadron, C.; Gallot, B. *Makromol. Chem.* 1980 *164*, 301-332.

(7) Shibayama, M.; Hashimoto, T. *Macromolecules* **1986**, *19*, 740-749.

(8) Hosemann, R.; Bagchi, S. N. in *Direct Analysis of Diffraction by Matter*, Amsterdam: North-Holland, **1962**

(9) Blundell, D. J. *Acta Cryst.* **1970**, *A26*, 472-476,476-483.

(10) Ruland, W. *Colloid. Polym. Sci.* **1977**, *255*, 417-427.

(11) Ruland, W. *J. Appl. Cryst.* **1971**, *4*, 70-73.

(12) Vonk, C. G. *J. Appl. Cryst.* **1973**, *6*, 81-86.

(13) Hashimoto, T.; Nagatoshi, K.; Todo, A.; Hasegawa, H.; Kawai, H. *Macromolecules*, **1974**, *7*, 364-373.

(14) Hashimoto, T.; Suehiro, S.; Shibayama, M.; Saijo, K.; Kawai, H. *Polym. J.* **1981**, *13*, 501-516.

(15) Montezinos, D.; Wells, B. G.; Burns, J. L. *Polym. Lett.* **1985**, *23*, 421.

(16) Hashimoto, T.; Todo, A.; Itoi, H.; Kawai, H. *Macromolecules* **1977**, *10*, 377-384.

Chapter 3

Novel Morphology of Three-Component, Three-Arm, and Star-Shaped Block Copolymers

3-1. Introduction

In Chapters 1 and 2, formation of microdomain structures and detailed analyses of the structures were presented. The specimen studied there was linear diblock (Chapter 2) and triblock (Chapter 1) copolymers. For a linear block copolymer in the strong segregation limit, the morphology formed is solely described by the relative volume fractions of the two components, as being well known as "Molau's law".[1] However, the influence of copolymer architecture on the formation of the interface, and therefore on the structure of the microphase-separated state has not been studied well. In this chapter, for a new approach to create new domain structures which possibly have new properties , a new molecular architecture is introduced.

There is no doubt about the importance of multicomponent multiphase polymer systems (or "polymer alloys") in terms of both academic interest and practical use. Graft and block copolymers were a new class of polymers belonging to such systems and they gave a great impact to the world when they were first introduced. The copolymers we introduce in this and the previous papers,[2] ABC three-arm star-shaped copolymers (hereafter abbreviated as "ABC stars"), are another new class of polymers. We believe that they will develop a completely different physical situation and give a great impact again. In the previous paper

we reported the synthesis techniques of the model ABC stars[2] and in this paper we report the preliminary results of our study on their morphology.

The synthesis and the morphology of the three-arm star copolymers consisting of polystyrene, polyisoprene and polybutadiene arms named "miktoarm" (mixed-arm) copolymers were reported by Hadjichristidis and his coworkers.[3,4] However, their miktoarm copolymer and our ABC stars are essentially different as described below. Our copolymers, ABC stars, are the asymmetric star-shaped copolymers comprising three arms, i.e., polystyrene, poly(dimethylsiloxane) and poly(*tert*-butyl methacrylate), having completely different chemical natures and hence form three different microphases composed of each constituent polymer. On the other hand, the miktoarm copolymers consist of polystyrene, polyisoprene and polybutadiene arms. Since the latter two are miscible, the copolymers can form only two different microphases. Therefore, they are considered as "ABB' stars" according to our terminology. The molecular architectures of ABC stars and ABB' stars are similar, but their difference is not trivial. The microphase separation of the latter may be similar to that of AB_2 graft copolymers (A polymer grafted onto B polymer).[4,5] However, the former is considered as a new type of polymeric materials and might exhibit entirely new morphology and physical properties different from existing polymeric materials such as ordinary graft copolymers and linear block copolymers.[1,6,7] It will also bring about interesting problems in polymer physics. The reason why ABC stars are so different and important is discussed below.

It is expected that the characteristic molecular architecture of ABC stars with the three different arms connected at a single point plays an important role and this problem must be investigated both experimentally and theoretically. If

the constituent polymers of the ABC stars are immiscible each other, they undergo microphase separation to form three different phases, but the way they form microdomain structures should be very different from that of AB diblock or linear ABC triblock copolymers as schematically illustrated in Figure 3-1. In case of AB diblock copolymers in the strong segregation regime, the chemical junction points between A and B block chains are always confined on the ***interfaces*** (or in the narrow interfacial regions) between A and B microdomains regardless of the microdomain morphology (Figure 3-1(a)). The situation is same for linear ABC triblock copolymers (Figure 3-1(b)) although a greater variety of microdomain morphologies are possible for linear ABC triblock copolymers.[8-14] However, the situation is quite different for ABC stars. When the three components form their own microdomains, the chemical junction points of the three arms of ABC stars must be confined not only on the interfaces but also on the ***lines*** where three different microdomain interfaces, i.e., the interfaces between A and B, between B and C, and between C and A microdomains, intersect each other (Figure 3-1(c)). This topological constraint will restrict the microdomain morphology of ABC stars to very special ones. If the volume fractions of the three microdomains are all equal, two kinds of regular structures are intuitively derived: one consists of hexagonal columns of each microdomain and the other consists of lozenge-shaped columns of each microdomain as illustrated in Figures 3-2(a) and 3-2(b), respectively. But these models are strictly limited to the ABC stars having exactly the same volume fractions for the three components. What will be the microdomain structure if the volume fractions of the three components are not exactly the same? It is not is not easy to answer this question because it is not only the problem of polymer science but also a new problem in geometry.

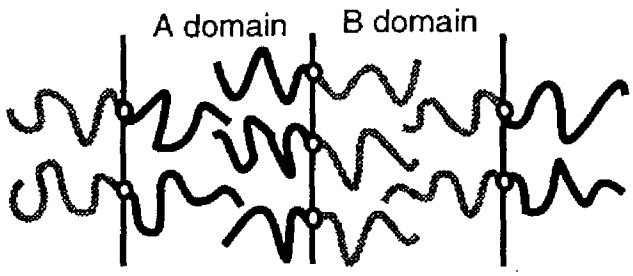

(a) AB diblock copolymer

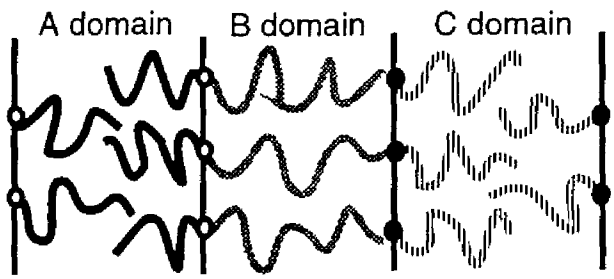

(b) ABC liniar triblock copolymer

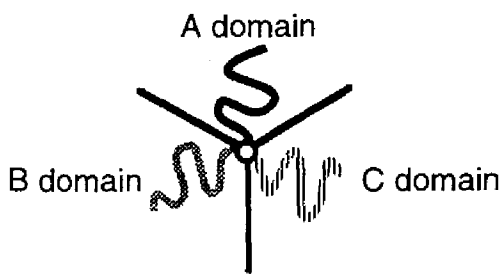

(c) ABC three-arm star copolymer

Figure 3-1. Schematic illustrations of the arrangement of copolymer chains: (a) AB diblock copolymer: the chemical junction points are confined on the interface. (b) linear ABC triblock copolymer: the chemical junction points are confined on the interfaces. (c) ABC star: the chemical junction points are confined on a line.

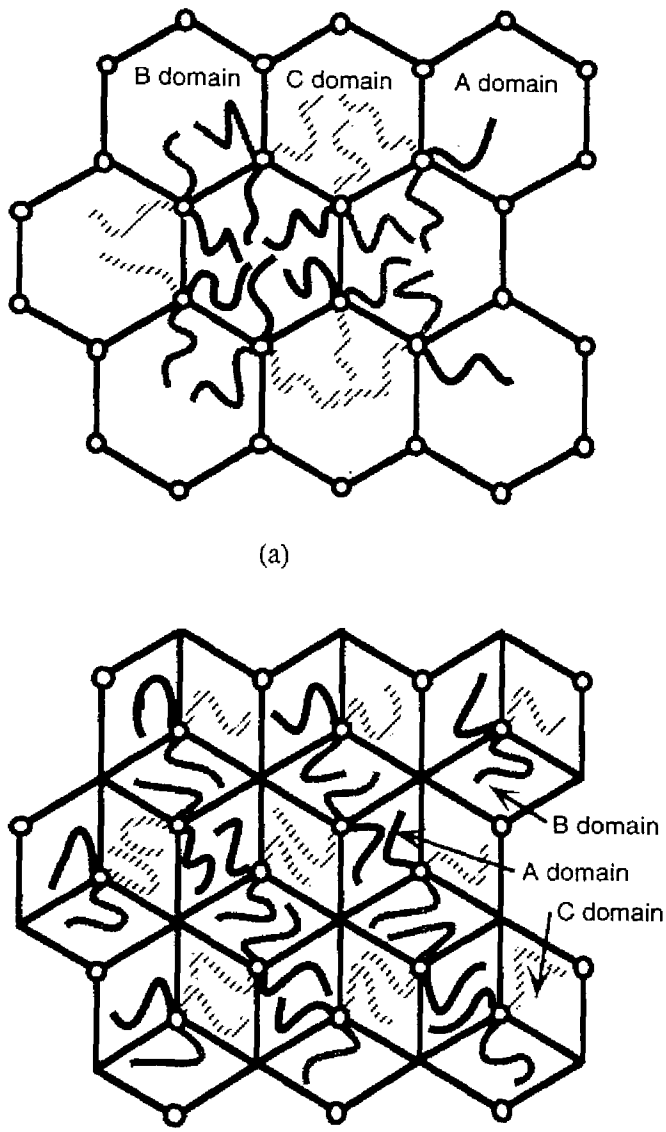

Figure 3-2. Possible microdomain structure models for the particular ABC star having equal volume fractions of the three components: (a) each microdomain consists of a hexagonal column. (b) each microdomain consists of a lozenge-shaped column. The chemical junctions are located on the lines normal to the paper as marked by circles. The circles form the same two-dimensional hexagonal array for both cases.

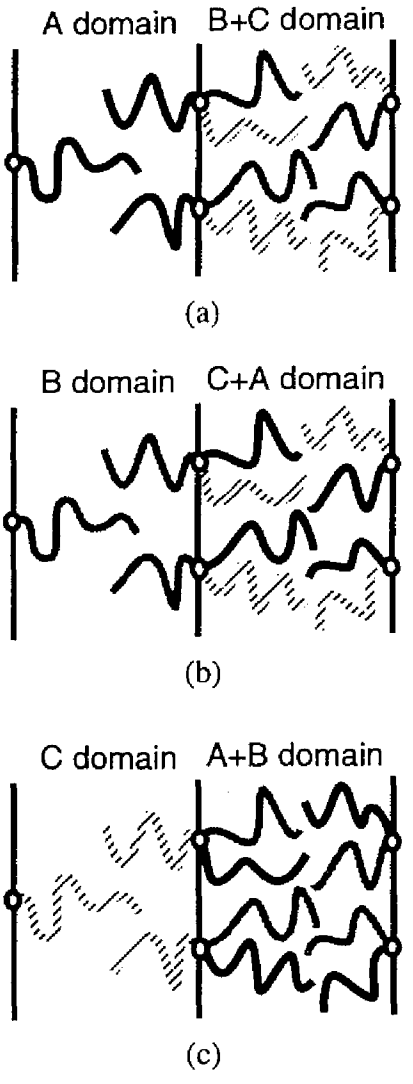

Figure 3-3. Schematic illustrations of the arrangement of ABC star chains: (a) B and C components are mixed to form a single phase. The chemical junctions are confined in the interfacial region. (b) C and A components are mixed. (c) A and B components are mixed.

Therefore, we think it is worthwhile to show the results of our observation in this paper although the structure is not yet clarified.

If the segregation power between B and C components of ABC stars decreases at high temperatures, B and C might mix to form a single phase resulting in the ordinary two-phase microdomain structures as illustrated in Figure 3-3(a). In such cases, the ABC stars will behave similarly to AB_2 graft copolymers and the chemical junction points are located in the interfacial region between A microdomain and the microdomain composed of the mixture of B and C. Such an example was reported for the miktoarm copolymers of ABB' type.[4,15,16] Change in the temperature may cause further phase separation between B and C resulting in a microdomain structure of three different phases. If the energetic cost to form a three-phase structure overtakes the gain in demixing between B and C, B and C are forced to be mixed. Depending on the temperature dependence of the pairwise interaction among the three components, transition from the structure shown in Figure 3-3(a) to that in Figure 3-3(b) or 3-3(c) might take place when the temperature changes.

The topologically constrained ABC stars are anticipated to have unique features in the phase transitions as well. The order-disorder transition and order-order transitions must be intuitively different from those of various linear block copolymers which have been extensively studied up to now. Thus, we propose the ABC stars as a truly new class of multicomponent polymers and as a new generation in a series of block and graft copolymers which have been developed so far.

3-2. Experimental Section

3-2-1. Specimen

Three model ABC star copolymers, S-ZH(222), S-ZH(333) and S-ZH(444), the synthesis and the purification of which were reported in our first paper,[2] were investigated in this study. The characterization of these samples are listed in Table 3-1. The three arms of the copolymers consist of polystyrene (PS), poly(dimethylsiloxane) (PDMS) and poly(*tert*-butyl methacrylate) (PTBMA), each of them having nearly the same weight fraction (but not exactly the same). Each of the three digits in the parentheses of the sample codes gives the approximate molecular weight of each component in the unit of 10 kg/mole. Besides the star-shaped copolymers, some of the corresponding diblock copolymers, i.e., polystyrene-*block*-poly(dimethylsiloxane) (PS-PDMS) and polystyrene-*block*-poly(*tert*-butyl methacrylate) (PS-PTBMA) were also prepared separately or obtained as the aliquots in the synthesis courses of the star-shaped copolymers. These diblock copolymers were used as the reference material in the thermal analysis. All the samples were cast at room temperature from solutions in toluene which is a good solvent for all three components. The cast films were further dried under vacuum for 1-2 days at room temperature and used for the experiments.

Table 3-1. Characterization of three-component, three-arm star-shaped copolymers.

Sample code	$10^{-4}M_n$(total)	Wt% of PSt	Wt% of PDMS	Wt% of PTBMA
S-ZH(222)	5.9	27	37	36
S-ZH(333)	10.0	34	35	31
S-ZH(444)	13.5	36	26	38

3-2-2. Thermal Analyses

The measurements of thermogravimetric-differential thermal analysis (TG-DTA) were performed on the star-shaped copolymers and the diblock copolymers in the heating process from 25 to 450 °C at the heating rate of 20 °C /min with a Rigaku TAS-200 thermal analysis system. The differential scanning calorimetry (DSC) was performed on those samples with a Perkin-Elmer DSC 7 calorimeter. The samples were first heated to 200 °C at the heating rate of 20 °C /min, held at 200 °C for 3 min, and cooled to 50 °C at the cooling rate of -320 °C /min. The DSC data were collected for the second heating cycle from 50 to 200 °C at the heating rate of 20 °C /min. For the low temperature measurements, the samples were cooled down to -130 °C and the DSC data were collected for the heating cycle from -130 to 0 °C at the heating rate of 20 °C /min. Temperature was calibrated using the melting peaks of indium and zinc.

3-2-3. Transmission Electron Microscopy

The as-cast film specimens were embedded in epoxy resin without pre-staining. The samples were then subjected to ultramicrotoming into ultrathin sections of ca. 50 nm thick at room temperature with an LKB ULTROTOME type 4802A ultramicrotome using glass knives. The ultrathin sections without any staining were served for the transmission electron microscopic (TEM) investigation with a Hitachi H-600S transmission electron microscope operated at 100 kV.

3-2-4. Small-Angle X-ray Scattering

Small-angle X-ray scattering (SAXS) profiles of the as-cast film specimens were measured in the same manner as described in Chapter 1.[17-19] The profiles were obtained for the edge (see Figure 2-2) and through configurations (see Figure 1-1).

3-3. Results and Discussion

3-3-1. Thermal Analyses

The thermogravimetry (TG) curves show the change of the weight of the samples and thus give the information about their thermal stability. For S-ZH(222) the weight started to decrease gradually from ca. 200 °C and an abrupt drop was observed at ca. 260 °C, which coincides with a sharp exothermic peak in the differential thermal analysis (DTA) curve. This abrupt change of weight is attributed to the decomposition of PTBMA as the same behavior was observed for the aliquot PS-PTBMA diblock copolymer. The observations of weight loss and exothermic peaks at ca. 200 °C due to anhydride formation on thermal treatment of PTBMA homopolymers have been reported.[20] The thermal stability decreases with increasing the molecular weight of the ABC stars. For S-ZH(444) the weight loss became significant above ca. 130 °C. Thus, the annealing of S-ZH(444) may cause an undesirable change in the chemical structure of the sample and the TEM observation was limited to the as-cast film.

Figure 3-4 shows the DSC curve of S-ZH(222) for the higher temperature region. Two endothermic shifts were observed in the thermogram. They are considered as the glass transition temperatures (T_g) of the PS and PTBMA

components. T_g(midpoint) evaluated from the DSC curve was 96 and 121 °C. The former is in good agreement with the literature value of T_g for PS homopolymer (100 °C) and the latter with that for atactic PTBMA homopolymer (118 °C).[21] This suggests that the microdomains giving rise to these T_g are composed of almost pure PS and PTBMA components, respectively. If PDMS component had been mixed with either PS or PTBMA component as shown in Figure 3-3, the T_g of the microdomain composed of PS or PTBMA mixed with PDMS should have been moved to a temperature significantly lower than the T_g of pure PS or PTBMA, e.g., at -77 or -62 °C, respectively, estimated by using -127 °C for the T_g of pure PDMS[21] and Fox equation:[22]

$$T_g^{-1} = w_1 T_{g1}^{-1} + w_2 T_{g2}^{-1} \tag{3-1}$$

where w_i is the weight fraction of component i (i = 1 or 2) in the microdomain and T_{gi}^{-1} is the T_g of pure component i.

The aliquot PS-PTBMA diblock copolymers exhibited similar DSC curves as that in Figure 3-4 exhibiting two T_g relevant to PS and PTBMA microphases, while the PS-PDMS diblock copolymers showed only one T_g relevant to PS microphase in the DSC curves measured at the temperature range of 50-200 °C.

The existence of PDMS microdomains in the ABC star copolymer is further confirmed by the DSC measurements of S-ZH(222) (Figure 3-5(b)) and the corresponding PS-PDMS diblock copolymer (Figure 3-5(a)) for the lower temperature region. In Figure 3-5(a) for the diblock copolymer an exothermic peak at -96 °C and two endothermic peaks at -47 and -38 °C were observed. The

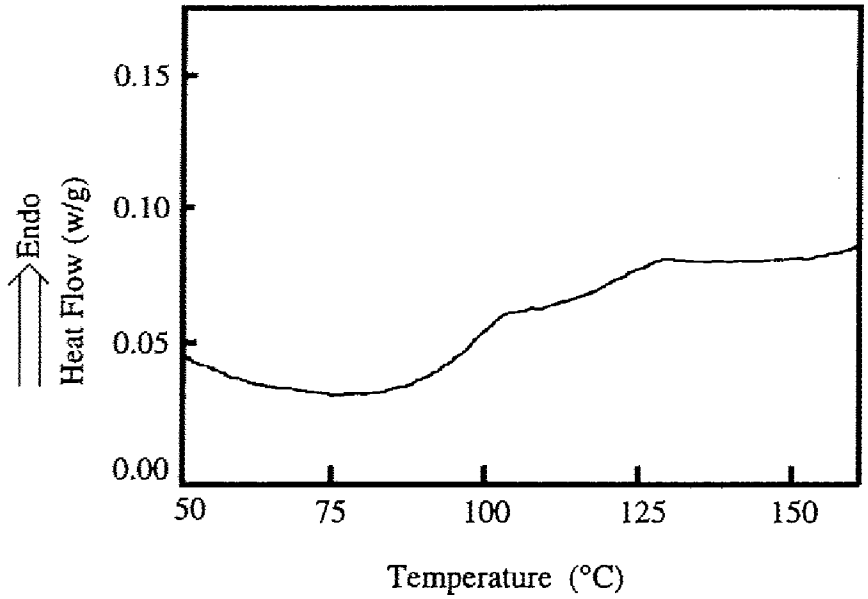

Figure 3-4. DSC curve for the second heating process of S-ZH(222) toluene-cast film for the higher temperature region (50 - 160 °C). The heating rate is 20 K/min.

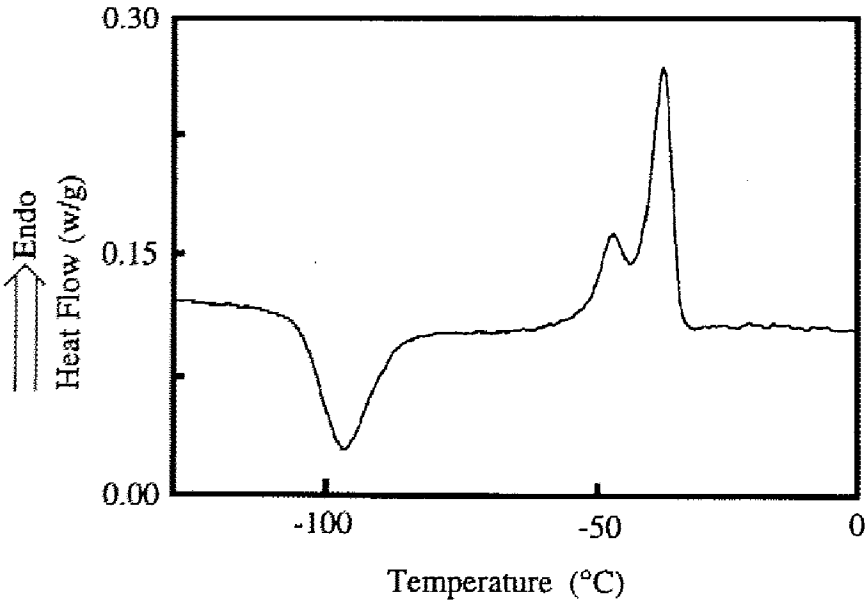

Figure 3-5. DSC curves for the heating process of a. PS-PDMS block copolymer and b. S-ZH(222) toluene-cast films for the lower temperature region (-120 - 0 °C). The heating rate is 20 K/min.

exothermic peak corresponds to the crystallization of PDMS component and the two endothermic peaks correspond to the melting of the PDMS crystals crystallized probably during the cooling process and the heating process. This observation is in good agreement with that reported for the microphase-separated PS-PDMS block copolymers by Feng et al.[23] Their measurement went down to -150 °C which was 20 °C below our lower limit and they observed the glass transition of the PDMS component having a similar molecular weight (M_n = 19,300) as ours at -125 °C. Thus, an observation of PDMS crystallization in a PS-PDMS block copolymer is a strong indication of its microphase separation. Figure 3-5(b) for S-ZH(222) clearly shows the exothermic peak of PDMS crystallization at ca. -115 °C and the endothermic peak of the melting of the PDMS crystals at ca. -45 °C. Therefore, the PDMS component in S-ZH(222) must be also forming its own microdomains independently. If the PDMS component of S-ZH(222) were mixed with one of the other components, PS or PTBMA, T_g of the mixed phase should be much higher than -115 °C (-77 °C for the PDMS/PS mixed phase and -62 °C for the PDMS/PTBMA mixed phase according to the calculation with eq 3-1) and PDMS would not crystallize at -115 °C. The existence of pure PDMS microphase is also supported by the absence of any T_g in the temperature range between -130 and 0 °C. It should be noted that the crystallinity of the PDMS component in S-ZH(222) is much smaller than that in the corresponding PS-PDMS block copolymer judged by the area of their melting peaks. This suggests that the PDMS chains in the microdomains of S-ZH(222) is more hindered from crystallization than those in the PS-PDMS block copolymer.

The DSC results imply that all three components are microphase-separated and forming their own microdomains in S-ZH(222), having the smallest molecular weight among the three ABC stars. Since the segregation power increases with increasing degree of polymerization, it is reasonable to conclude that the three components, PS, PTBMA and PDMS are microphase-separated also in the other two ABC stars, S-ZH(333) and S-ZH(444).

3-3-2. TEM Observation

TEM observation was performed on the ultrathin sections of the as-cast films without staining because Si atoms in PDMS component give a good contrast.[23] Figure 3-6 shows the typical images obtained from S-ZH(444) for low (part (a)) and high magnification (part (b)). Since the only element giving rise to the dark contrast in the images is Si atoms, the darkness in different regions reflects the content of PDMS segments in the thickness direction of the ultrathin section. The two-dimensional array of dark triangular patterns exhibits a three-fold symmetry (part (b)). The size of the dark triangles changes from one region (e.g. the region marked X) to another (marked Y) in part (a) although the orientation and the spacing (ca. 30 nm) of the periodic structure remain almost constant. This suggests that the regions X and Y have the same microdomain structure belonging to a single grain (the region where the microdomain structure is coherent) but sliced at different positions: the plane normal to the three-fold axis in the microdomain structure is slightly tilted with respect to the ultrathin section and that the structures at different levels along the three-fold axis are seen as the triangles with different sizes (note that the section thickness, ca. 50 nm, is slightly larger than the structural periodicity). This implies that the

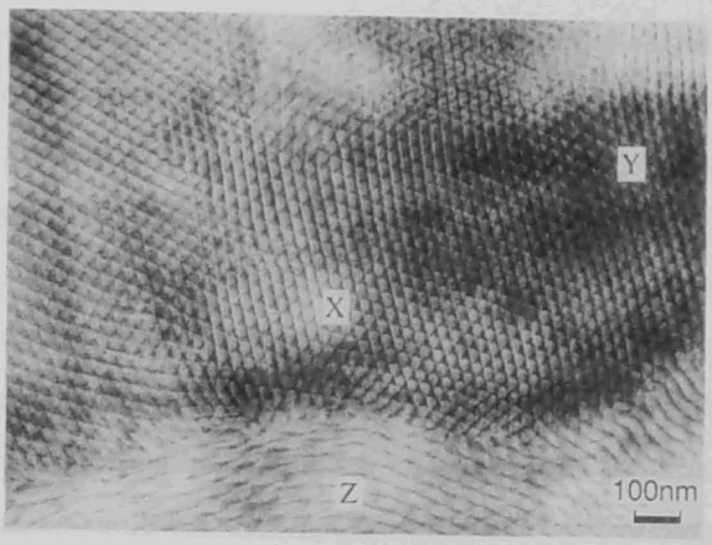

(a)

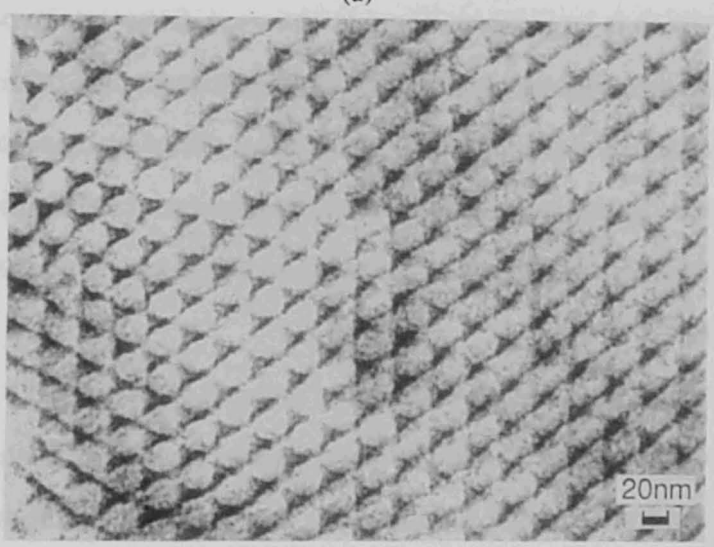

(b)

Figure 3-6. Transmission electron micrographs obtained from an unstained ultrathin section of S-ZH(444) toluene-cast film. a. low magnification. b. high magnification.

microdomain structure has a periodicity along the three-fold axis because if it did not and were composed of a two-dimensional array of three kinds of columnar microdomains as illustrated in Figure 3-2 the pattern should appear the same regardless of the levels of the slices. This implication is more clearly seen in the bottom of part (a) (the region marked Z) where another grain composed of the same microdomain structure with different orientation from that of regions X and Y is observed.

The appearance of the image in region Z is quite different from the region X or Y, but the microdomain structure itself is considered to be the same. It appears so different because the three-fold axis of this grain is significantly tilted with respect to the section normal. A layer-like (one-dimensional) periodicity (ca. 50 nm) which is larger than 30 nm is observed. Between the parallel dark lines dark triangles slightly elongated in the direction parallel to the dark lines are seen. Thus, the microdomain structure which is periodic also along the three-fold axis seems to be a complicated stucture. The dark PDMS microphase is seen to be continuous in three dimensions as no single area is observed without grayish contrast.

Besides these patterns a variety of patterns were observed in different areas of the same or different sections. Nevertheless, those patterns are considered to be originated from a single structure, i.e., they are different cross sections of the same structure and just reflect the complexity of the structure. It may be understood from an example shown in Figure 3-7. Parts (a) and (b) are the TEM pictures obtained from the same area of an ultrathin section (ca. 50 nm thick) of S-ZH(444) but in part (b) the section is tilted by 25° in the microscope around the axis indicated by a white broken line. The patterns in the two micrographs

appear quite differently. The dark triangular patterns become more clear in part (b).

To summarize, neither of the two simple models as shown in Figure 3-2 can explain the TEM observations. The dark PDMS microdomain seems to be continuous in three dimensions. Therefore, it is natural to consider that the microdomains of PS and PTBMS both appearing bright are also continuous in three dimensions because the volume fraction of PDMS is less than 1/3. Although the PS and PTBMA microdomains are not distinguishable, it is reasonable to consider that both phases are continuous in three dimensions because their volume fractions are almost the same. Thus, a complicated but regular microdomain structure consisting of three continuous networks of different components is suggested for S-ZH(444).

S-ZH(222) seems to have the similar structure as S-ZH(444). However, the TEM micrographs are less clear because of the smaller microdomain size for the smaller molecular weight and because of the overlapping of the structure within the ultrathin sections.

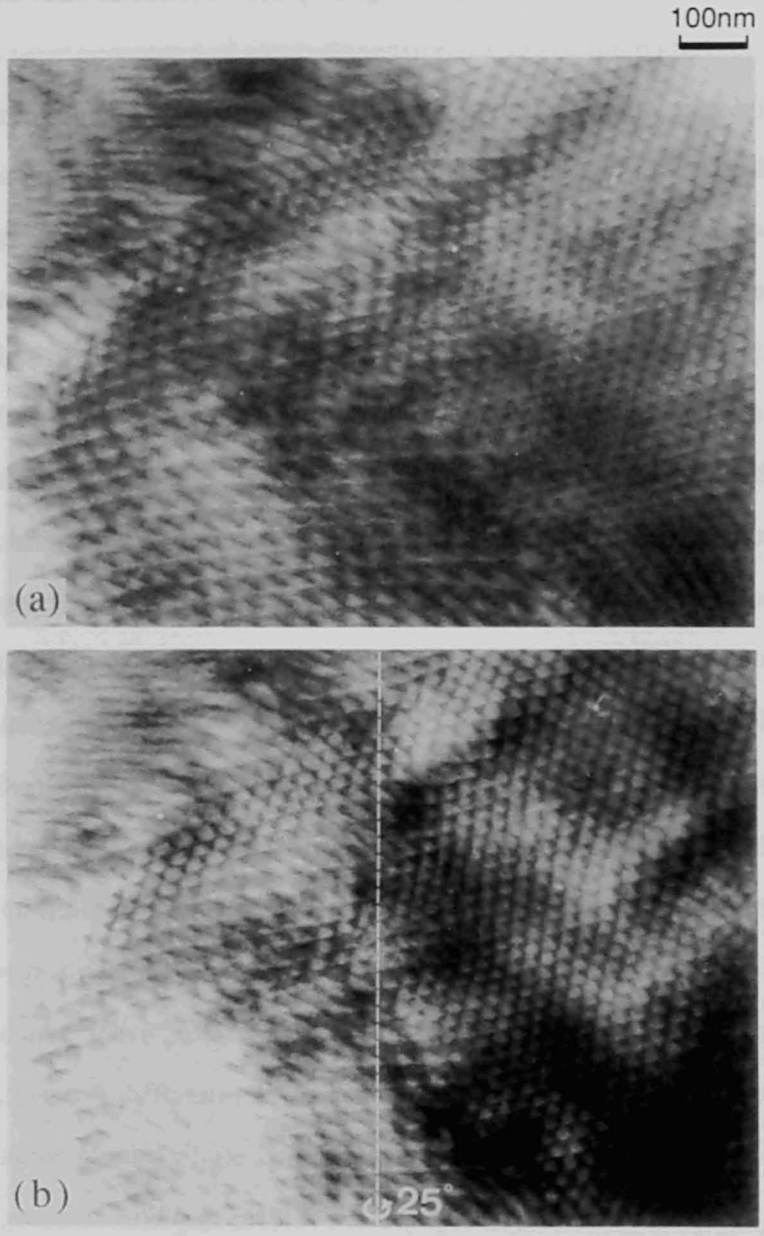

Figure 3-7. Transmission electron micrographs obtained from an unstained ultrathin section of S-ZH(444) toluene-cast film. a. an area exhibiting various patterns. b. the same area as part (a) but the section was tilted by 25° about the axis indicated by the white broken line.

3-3-3. SAXS

Figure 3-8 shows the SAXS profiles obtained for the as-cast film of S-ZH(444) with two configurations, edge (triangles) and through (circles). The logarithm of the absolute intensity is plotted against the magnitude of the scattering vector, q (= $(4\pi/\lambda)\sin(\theta/2)$, θ: scattering angle, λ: wavelength). The difference between the two profiles can be attributed to the nonequilibrium effect set in the film specimen during the casting process. The structural relaxation parallel to the film surface was hindered by the interaction between the film and the substrate resulting in the smaller spacing for the edge profile than the through profile. When the abscissa is normalized by q*, the q value at the first-order peak, the edge and through profiles can be superimposed on top of each other as shown in the insertion of Figure 3-8.

The scattering profiles of S-ZH(444) exhibit multiple scattering peaks at q positions in the ratio of 1, $3^{1/2}$ and $7^{1/2}$. This strongly supports the existence of the very regular structure with three-fold symmetry as observed in the TEM images. The Bragg spacings evaluated from the first-order scattering peaks are 47 nm and 36 nm for the through and edge profiles, respectively. The latter is in good agreement with 30 nm, the spacing observed by TEM, which is reasonable because the ultrathin section is cut perpendicularly to the film surface and the TEM images correspond to the edge profile. Further analysis of the SAXS profiles will be performed when a possible model for the structure comes out.

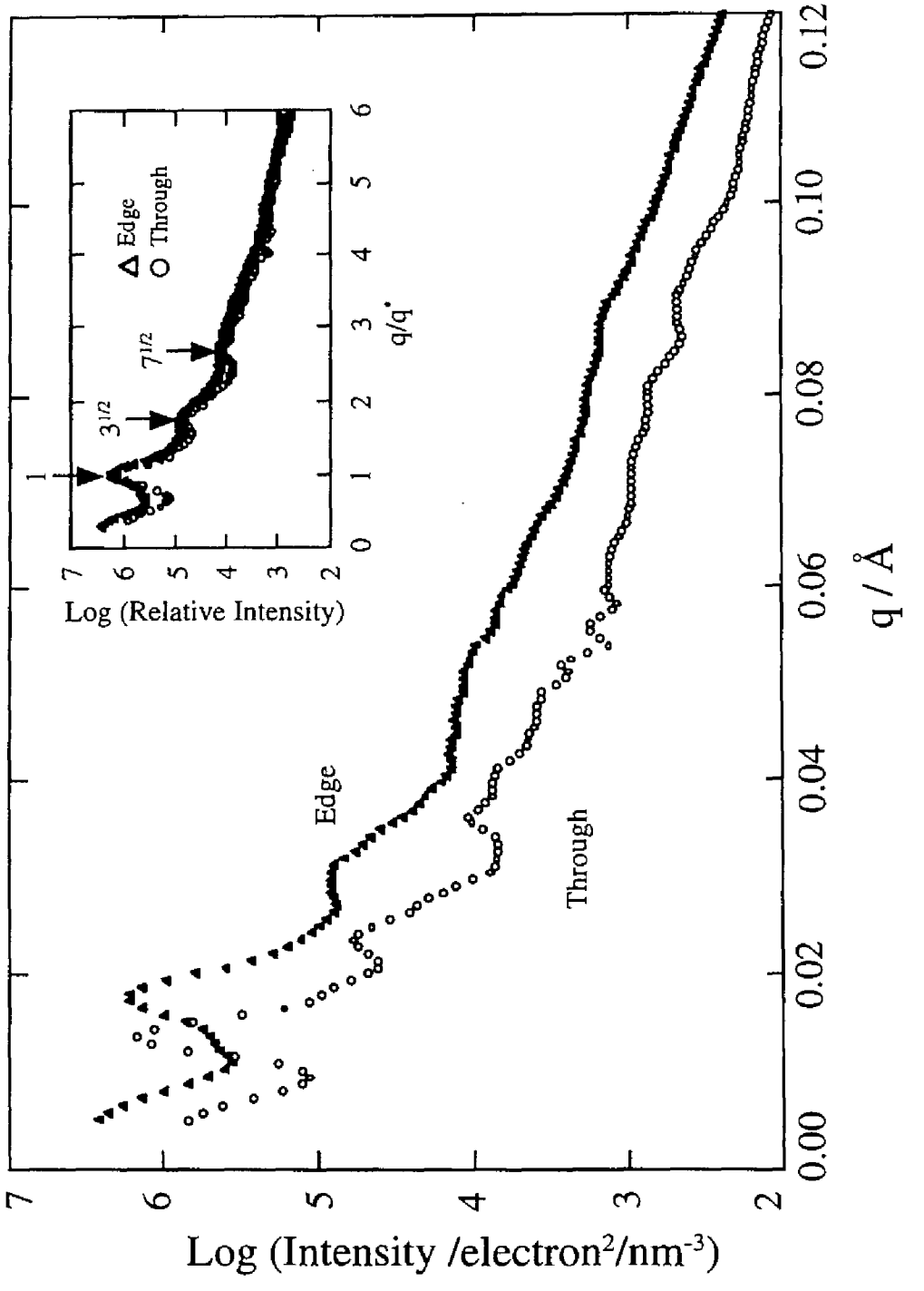

Figure 3-8. Small-angle X-ray scattering profiles for edge (open triangle) and through geometries (open circle) obtained from S-ZH(444) toluene-cast film. The insertion shows the normalized profiles with the abscissa q/q*.

3-4. Conclusion

Three-component, three-arm star-shaped copolymers consisting of polystyrene, poly(dimethylsiloxane) and poly(*tert*-butyl methacrylate), each of them having nearly the same weight fraction were investigated by means of DSC, TEM and SAXS. DSC results exhibiting the glass transition of polystyrene and poly(*tert*-butyl methacrylate) and the crystallization and melting of poly(dimethylsiloxane) strongly suggest the microphase separation of the three components into three microdomains. TEM and SAXS results strongly support the existence of the very regular microdomain structure with a three-fold symmetry. Each of the three components possibly forms a three-dimensionally continuous network domains resulting in an ordered tricontinuous microdomain structure.

References

1. Molau, G. E. in 'Block Polymers' (Ed. S. L. Aggarwal), Plenum, New York, 1970.
2. Fujimoto, T., Zhang, H., Kazama, T., Isono, Y., Hasegawa, H. and Hashimoto, T. *Polymer* 1992, **33**, 2208.
3. Iatrou, H. and Hadjichristidis, N. *Macromolecules* 1992, **25**, 4649.
4. Hadjichristidis, N., Iatrou, H., Behal, S. K., Chludzinski, J. J., Disko, M. M., Garner, R. T., Liang, K. S., Lohse, D. J. and Milner, S. T. *Macromolecules* 1993, **26**, 5812.
5. Pochan, D. J., Gido, S. P., Pispas, S., Mays, J. W., Ryan, A. J., Fairclough, P., Hamley, I. W. and Terril, N. *Macromolecules* 1996, **29**, .
6. Hasegawa, H., Tanaka, H., Yamasaki, K., Hashimoto, T. *Macromolecules* 1987, **20**, 1651.
7. Bates, F. S. and Fredrickson, G. H. *Annu. Rev. Phys. Chem.* 1990, **41**, 525.
8. Riess, G., Schlienger, M. and Marti, S. *J. Macromol. Sci., Polym. Phys. Ed.* 1980, **17**, 355.
9. Arai, K., Kotaka, T., Kitano, Y. and Yoshimura, K. *Macromolecules* 1980, **13**, 1670.
10. Shibayama, M., Hasegawa, H., Hashimoto, T. and Kawai, H. *Macromolecules* 1982, **15**, 274.
11. Mogi, Y., Kotsuji, H., Kaneko, Y., Mori, K., Matsushita, Y. and Noda, I. *Macromolecules* 1992, **25**, 5408.
12. Gido, S. P., Schwark, D. W., Thomas, E. L. and Goncalves, M. C.

Macromolecules 1993, **26**, 2636.

13. Stadler, R., Auschra, C., Beckmann, J., Krappe, U., Voigt-Martin, I. and Leibler, L. *Macromolecules* 1995, 28, 3080.
14. Zheng, W. and Wang, Z.-G. *Macromolecules* 1995, **28**, 7215.
15. Floudas, G., Hadjichristidis, N., Iatrou, H., Pakula, T. and Fischer, E. W. *Macromolecules* 1994, **27**, 7735.
16. Floudas, G., Hadjichristidis, N., Iatrou, H. and Pakula, T. *Macromolecules* 1996, **29**, 3139.
17. Hashimoto, T., Suehiro, S., Shibayama, M., Saijo, K. and Kawai, H. *Polym. J.* 1981, **13**, 501.
18. Fujimura, M., Hashimoto, T. and Kawai, H. Mem. *Fac. Eng., Kyoto Univ.* 1981, **43**, 224.
19. Hendricks, R. W. *J. Appl. Crystallogr.* 1972, **5**, 315.
20. Matsuzaki, K., Okamoto, T., Ishida, A. and Sobue, H. *J. Polym. Sci., Part A* 1964, **2**, 1105.
21. Brandrup, J. and Immergut, E. H. 'Polymer Handbook, 3rd Ed.', Wiley, New York, 1989.
22. Fox, T. G. *Bull. Am. Phys. Soc.*, 1956, **1**, 123.
23. Feng, D., Wilkes, G. L. and Crivello, J. V. *Polymer* 1989, **30**, 1800.

Part II

Dynamic Behaviors of Block Copolymers under Large-Amplitude Oscillatory Shear Deformation

In Part I, I mainly dealt with the static aspects of the interfaces in block copolymers, such as the determination of the order-disorder transition temperature and the domain structures, as well as the time-evolution of the microdomain structures in the ordering process. On the other hand, I will deal with the dynamic aspects of the microdomain interfaces and structures in block copolymers in Part II. It is extremely interesting how the molecules confined in a space of several ten-nanometer scale respond to mechanical stimulation. Such knowledge may provide us a new insight in the physics of complex liquids and also a new technique in an industrial application of block copolymers. Along this line, I will investigate effects of external fields on orientational change of microdomains, or rearrangement of molecules in Part II.

Chapter 4

Time-Resolved Small-Angle and Wide-Angle X-ray Scattering Apparatus Using an Imaging Plate as a Two-Dimensional Detector

4-1. Introduction

I constructed a new two-dimensional (2D) detector for SAXS in order to make it possible to investigate the behaviors of block copolymers under mechanical stimuli by X-ray diffraction. In this chapter, I present an application of an imaging plate, consisting of phosphor crystals photostimulable by X-ray, as a 2D detector for time-resolved small-angle X-ray scattering (SAXS) and wide-angle X-ray diffraction (WAXD) studies, especially designed for a use with a rotating-anode X-ray generator as a high-intensity X-ray beam source.

The imaging plate (IP) made out of a thin layer of the photostimulable phosphor crystals BaFBr : Eu^{2+} of thickness of 150 μm on polyester substrate film was originally developed for X-ray medical examinations.[1,2] Here I report an application of IP for time-resolved small-angle X-ray scattering (SAXS) and wide-angle X-ray diffraction (WAXD) studies. It has also been applied as a two dimensional detector for X-ray diffraction and scattering in materials science.[3-5]

When IP is exposed to scattered X-ray beam, the incident X-ray photons excite color centers in the photostimulable materials. The number of excited color centers is proportional to the number of incoming X-ray photons. Thus the generation of color centers corresponds to a recording or writing

process for the scattered X-ray. When the plate exposed to the scattered X-ray is scanned by a He-Ne laser beam, it emits a luminescent light whose intensity is proportional to the intensity of the scattered X-ray photons (reading process). The luminescent light is detected by a photomultiplier and the resulting photocurrent is digitized by an analog-to-digital converter (ADC). The color centers remaining in the plate can be erased by radiation from a halogen lamp. In this chapter I report a time-resolved SAXS and WAXD apparatus constructed in our laboratory using this imaging plate together with some preliminary results obtained using it.

In the past, most time-resolved SAXS and WAXD apparatus have been constructed using one-dimensional (1D) or two-dimensional (2D) position sensitive proportional counters (PSPCs).[6-14] The PSPC is an ideal photon counting device which is especially good at detecting weak X-ray intensity. However it has the drawback that the counting rate for incoming X-ray photons is rather low; typically a counting loss greater than or equal to ca. 10% is encountered when the counting rate of the incident photons is greater than or equal to 10^4 counts/s. For the 2D PSPCs, the position resolution is usually limited to the distance between anode wires so that the position resolution is not better than 1 mm. Then a large detector-to-camera distance is usually required for a high angular resolution, as in the example of a 10 m SAXS camera.[9] As a 2D position sensitive detector, the IP has an angular resolution of ca. 0.1 mm, much better than 2D PSPC and as good as a 1D PSPC. The IP is superior to a PSPC in detecting high flux X-ray photons: it can count up to ca. 2×10^6 counts/(s pixel), where one pixel has an area of 0.125×0.125 mm^2. Thus the IP is an ideal detector for SAXS and WAXD experiments with an incident X-ray beam from synchrotron radiation facilities.[3-5]

4-2. Apparatus

4-2-1. Overall Setup

Figure 4-1 shows an outline of the optical system in the SAXS and WAXD apparatus with the IP system. We use a 18 kW rotating anode X-ray generator (Sra-M18XHF, MAC Science Co., Ltd., Japan) which has two shutters. On one side of the focal spot we set up a SAXS system and on the other side a WAXD system. The Cu-K_α X-ray beam monochromatized by a graphite crystal (designated as monochro. in Figure 4-1) passes through a magnetic shutter on both systems. In the SAXS system, the X-ray beam is collimated by a couple of pinholes or slits. The third slit is used to eliminate the parasitic scattering from the 2nd slit or pinhole edge. The camera distance between the specimen and the IP face for the SAXS system is fixed at 1410 mm. In these conditions the maximum scattering vector q attainable is 2.88 nm^{-1} where $q = (4\pi/\lambda)\sin(\theta/2)$, and θ and λ are the scattering angle and wavelength of the X-ray beam, respectively. The minimum scattering vector depends on the size of the collimated beam and of the beam stop. The beam stop is put on a polyester film and placed at 60 mm in front of the IP in the vacuum chamber, as shown in Figure 4-1. When using a beam stop of 3 mm diameter, the minimum scattering vector accessible is $q = 4.85 \times 10^{-2}$ nm^{-1}. In the WAXD system, the X-ray beam is collimated by a pinhole collimator (diameter 0.1, 0.5, 1.0 mm). The camera distance between the sample and the IP face can be changed from 70 mm to 220 mm. If the camera distance is 150 mm, which corresponds to the radius of the curvature of the IP plates as will be described later, we can use the IP detector as a cylindrical camera.

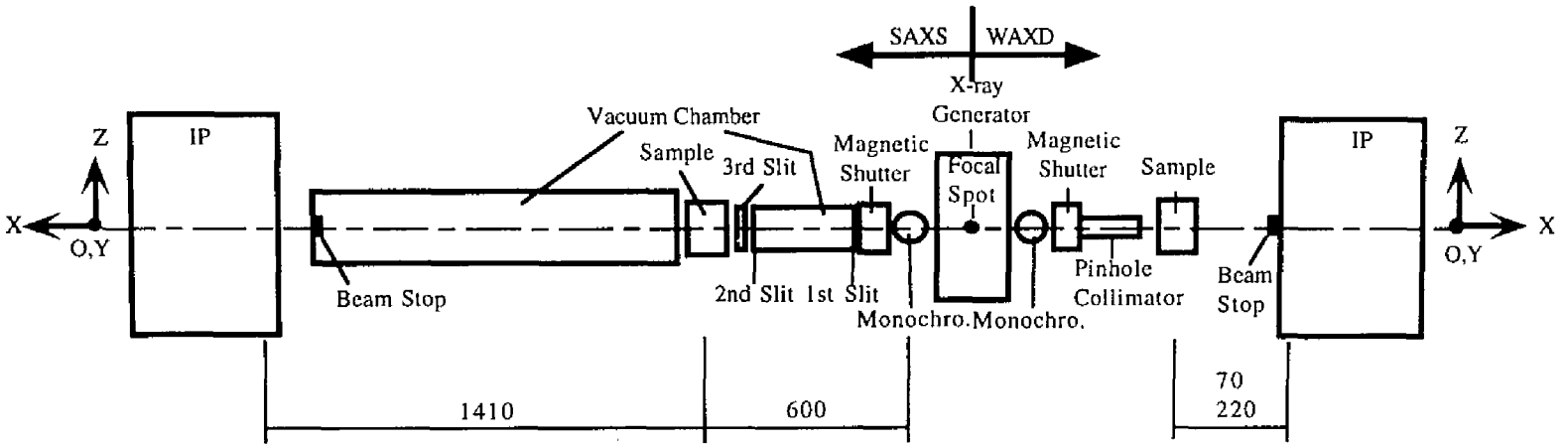

Figure 4-1. Optical alignment of the time-resolved small-angle and wide-angle X-ray scattering system using the Imaging Plate (IP) as a two-dimensional detector.

4-2-2. 2D Imaging Plate Detector

Figure 4-2 shows an inside view of the detector part of the IP system. The whole detector part is placed in a box which shuts off room light. The detector has the shape of an octahedral cylinder, and to each face is attached an imaging plate of 200 mm width and 100 mm height. The IPs have radii of curvature 150 mm along the *OZ* axis and infinite along the *OY* axis. The 2D scattering pattern recorded on an IP is read out by scanning the laser beam in the horizontal and vertical directions with a step of 125 μm, which defines an array of 800 × 1600 pixels. The plate designated ① in Figure 4-2 is the IP exposed to a scattered X-ray; the plate opposite to this one faces the reading device ④. We can carry out the writing and reading operations simultaneously. The He-Ne laser beam ③ (10 mW power) is led into the scanning device ④ through the optical fiber. There is a lens at the end of the scanning device. This lens focuses the laser beam to a size of 70 μm on the IP face and collects the photo-stimulated luminescence (PSL) that is emitted from the IP face when the IP face exposed to scattered X-rays is irradiated with the laser beam. The scanning is conducted by rotating the scanning device ④, which is shifted continuously along the *OY* axis. The radius of curvature of the IP corresponds to that of the rotating scanning device. It takes 300 s to read out the data from the whole area of the IP of 200 mm × 100 mm. Two photomultipliers (PM1 and PM2) with different sensitivities are used to detect the PSL and to expand the dynamic range in detecting the PSL: the second PM (PM2) is used to measure intensities of the PSL that saturate the first one (PM1). The IP thus subjected to the reading operation is then placed at the erasing position ② in Figure 4-2, where radiation from a halogen lamp erases the residual pattern (color centers) on

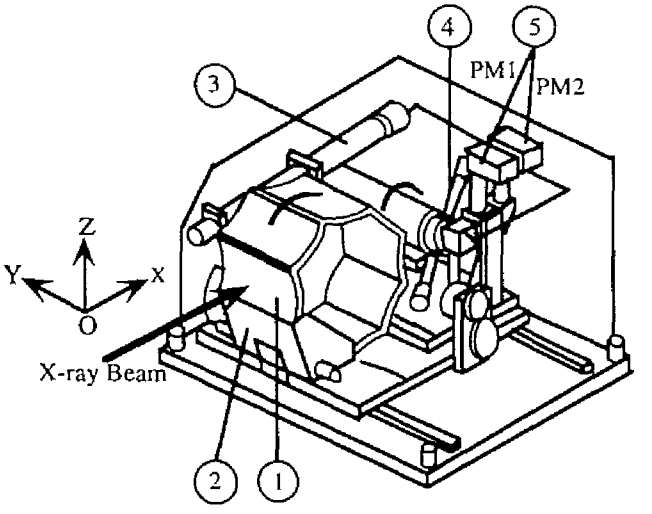

Figure 4-2. Schematic view of the inside of the Imaging Plate (IP) detector which has eight IPs with their full size of 100 mm × 200 mm. ① The IP in the exposure position for 2D X-ray scattering patterns; ② the IP in the erasing position where a halogen lamp (500 W) is installed; ③ a He-Ne laser (10 mW) used as a reading device ④; ⑤ two photomultiplier tubes (PM1 and PM2) and preamplifiers which detect photo-stimulated luminescent light intensity emitted from the IP.

the IP. In this way the IP can be used repeatedly. A distortion of 2D scattering patterns due to the curvatures of the IP was corrected with computer programs developed in our laboratory. Validity of the correction software was confirmed by comparing the data with the desmeared scattering profiles obtained by other detectors.

Figure 4-3 shows a typical procedure of a time-resolved experiment using the IP. The shifting rate of the IP along the horizontal direction the *OY* is 40 mm/s. In the case of an IP being divided into n sections along the *OY* axis (n = 4 in the case of Figure 4-3(a)), it takes 5/n s to shift the IP from the center of an exposure section to the next center. The time required to rotate the IP drum to the exposure position (i.e., rotation from plate no. 1 to next plate no. 2) is 2 s. The plate to be exposed is changed from no. 1 to no. 8 in turn, as shown in Figure 4-3(b). When plate no. 1 is irradiated with scattered

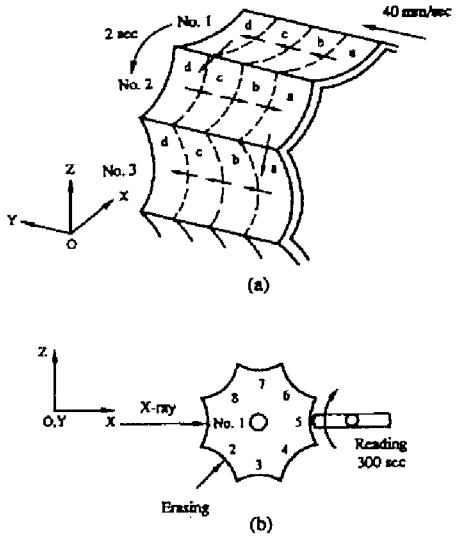

Figure 4-3. Schematic diagram showing shifting of the IP detector plane relative to the incident X-ray source in the time-resolved measurements using the IP detector.

X-rays, we can simultaneously read out the data from plate no. 5 at a different side. If the reading and the writing are carried out at the same time and if the exposure time is shorter than the reading time (300 s), then the lapse of time between reading and exposing is the dead time of the measurement.

Figure 4-4 schematically shows the principle of the reading procedure by using two PMs with different

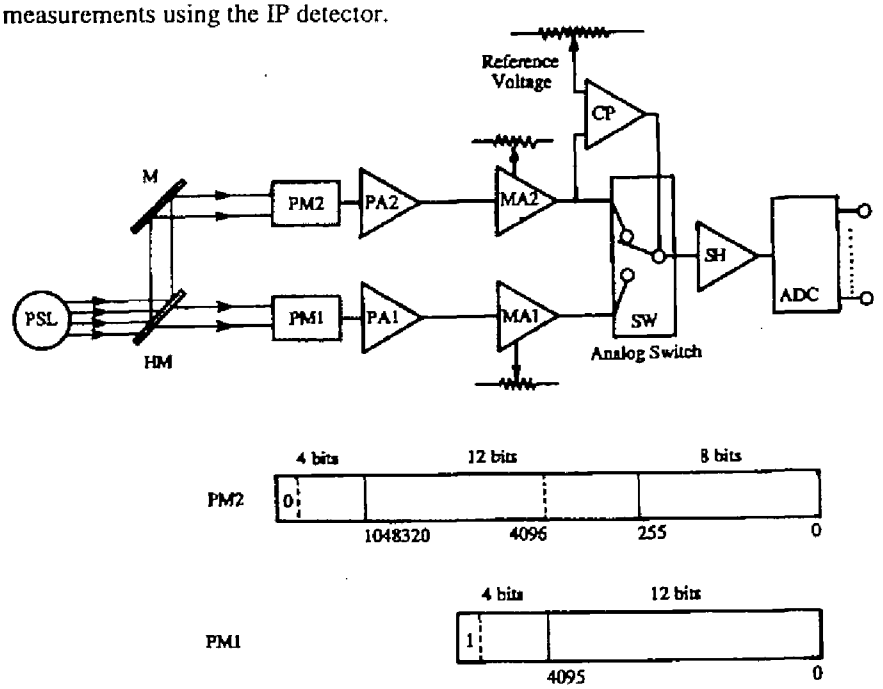

Figure 4-4. Method of expanding the dynamic range of the IP X-ray detector system by using two photomultiplier tubes (PM1, PM2) with different sensitivities. PSL, photo-stimulated luminescence; HM, half mirror; M, mirror; PA1 and PA2, preamplifiers; MA1 and MA2, main-amplifiers; CP, comparator which compares the intensity measured by PM2 with the reference voltage; SW, analog switch; SH, sample hold; ADC, A/D converter. PM2 is used for high intensity level (4096 - 1048320 level) and PM1 for low intensity (0 - 4095 level).

sensitivities. PM2 has lower sensitivity and PM1 higher. The PSL that is stimulated by a laser beam is detected simultaneously by two PMs through a half mirror HM and a mirror M. PM2 is used for the high level intensities and PM1 for the low ones. The output of the PM2 is amplified through a preamplifier (PA2) and a main-amplifier (MA2) and compared with a certain reference voltage level. If the output of the MA2 is higher than the reference voltage level, the data of the PM2 is used, and if it is lower, the data of PM1 is used. A 12-bits analog-to-digital converter (ADC) is used to digitize the outputs of the amplifiers and the data is saved in the form of 2-bites binary (16 bits) adding four bits to the most significant bit. In the case of the high intensity data obtained by PM2, one digit is weighted with 256. The threshold between the two PMs is 4096 levels. PM1 counts from 0 to 4095 level and PM2 counts from 4096 to 1048320 level. One level corresponds to 3 X-ray photons.

Figure 4-5 shows a schematic diagram of the IP system. It consists of the IP detector, the controller and a personal computer (PC). The PC (PC9801RX2) sends the command to the controller through a serial interface RS232C, and makes the controller execute the writing, reading and erasing procedures of 2D scattering data and their data acquisition into the memory area, RAM (random access memory board) and HDD (hard disk drive unit) having capacities of 8 Mbytes and 40 Mbytes, respectively. The data are stored in the memory of the PC through an ethernet cable. The data on 100 mm $\times$ 200 mm IP occupies a memory of 2.56 Mbytes. A work station or a university computer connected to the personal computer through an ethernet cable could process and analyze the IP data.

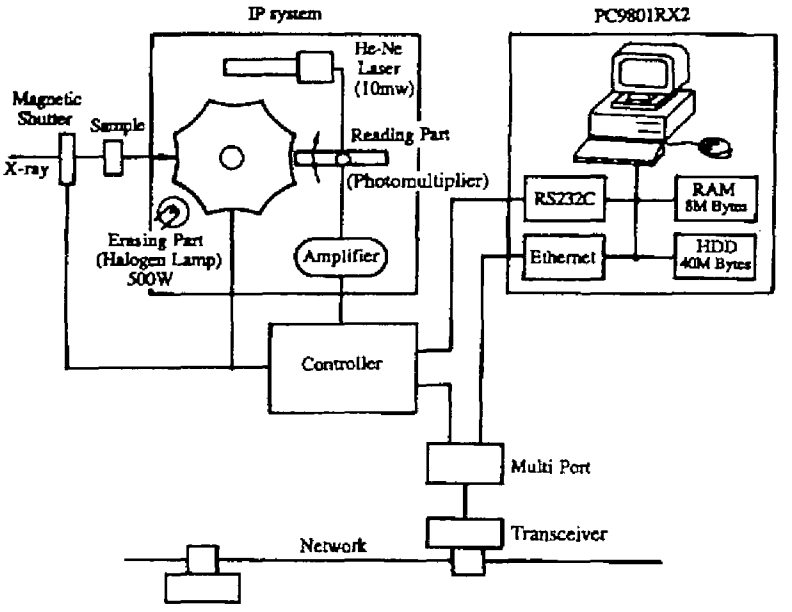

Figure 4-5. Schematic diagram showing control of the IP system with eight IPs and data acqusition (writing and reading) and data erasure.

4-2-3. Characteristics of 2D Imaging Plate System

Figure 4-6 shows the linearity and dynamic range of the IP used in this work. These data were obtained with the SAXS system shown in Figure 4-1 using a direct incident beam from the rotating anode generator generated with a power of 50 kV × 200 mA. The incident beam was collimated by a pair of pinhole slits (0.5 mm in diameter). The IP was irradiated by the incident beam for varying exposure time. The relation between the intensity and the exposure time is shown in Figure 4-6(a). The intensity (level/pixel) is obtained by dividing the total intensity received on a 7 pixels × 7 pixels square by the total number of pixels, 49. Therefore the intensity unit is the level per pixel. The intensity levels off around 8×10^5 level/pixel. This could be due either to saturation of the photo-stimulated luminescence in the IP with an increasing number of incident X-ray photons or to insufficient stimulation power of the laser used.

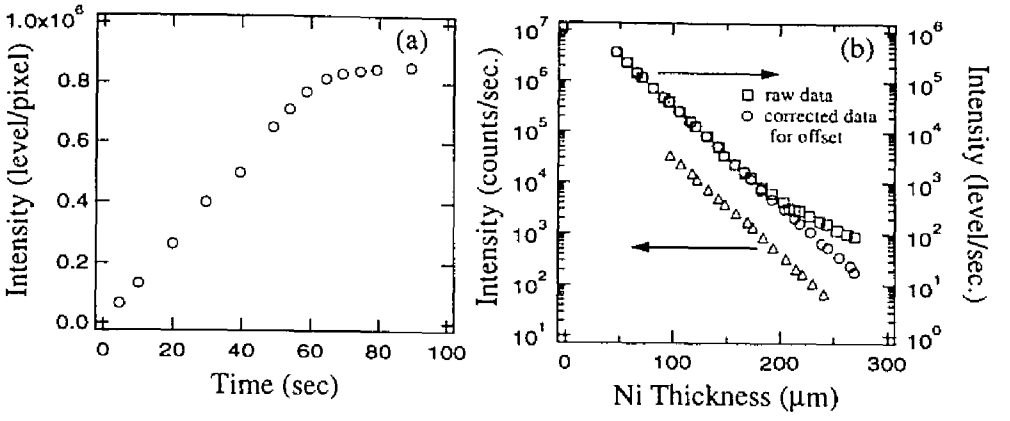

Figure 4-6. Dynamic range of the IP. (a) Relation between the exposure time and the intensity measured by the constant X-ray intensity. (b) Relation between thickness of Ni filter and the intensity measured by PSPC (△) and IP (○, □). The data after subtraction of the offset level (electric background and cosmic rays) from the raw data (□) are shown by ○.

Figure 4-6(b) shows the dependence of the incident intensity on the thickness of the Ni filter through which incident beam intensity was measured by a PSPC and the IP. The intensities measured by the two detectors are shown for the same solid angle. The left-hand side ordinate scale is the intensity measured by the PSPC (in counts per second) and the right-hand side is that measured by the IP (in level per second). At high incident X-ray intensity obtained with a thin Ni thickness (thinner than 100 μm) , the output of the PSPC is saturated due to a counting loss inherent in the system, but the IP can measure up to 8×10^5 level/pixel as shown in Figure 4-6(b) i.e., up to the intensity level much higher than the PSPC. At lower intensity measured with a thick Ni thickness (thicker than 200 μm), the relation between the intensity measured by IP and Ni thickness begins to deviate from linearity (see the data shown by squares), because of the offset electric signal level in the IP system which exists even without X-ray exposure. The offset corresponds to the intensity level of the electric background and cosmic

rays. The offset can be measured by reading out the intensity of the IP detector kept unexposed to X-rays for a given time after erasing. The offset increases with this resting time. If the correction of the offset level is exactly made, the intensity of an IP obtained at the low intensity level can be correctly evaluated, as shown by the data marked with circles. The intensity of the IP is equal to that of the PSPC if one level corresponds to 3 X-ray photons. This correspondence is obtained by taking into account the fact that the counting efficiency of PSPC with PR gas (Ar + 10% CH_4) is about 30%. The results in Figure 4-6(b) indicates that the IP has a very large dynamic range at least as large as five orders of magnitudes, which is much larger than the PSPC, and is especially good for the high intensity side. Thus it should be an ideal detector for synchrotron X-ray studies.

The uniformity of the sensitivity in any position of an IP and among eight IPs is evaluated from the change of the total intensity stored on a certain area of an IP. The intensity is measured by irradiating a direct beam with a constant intensity. If the IP drum is repeatedly driven with a constant speed from side to side along its horizontal direction (*OY* direction), a locus of the direct beam is drawn on the IP. Figure 4-7(a) shows the intensity variation over the different positions of an IP. The intensity on the same position of each IP plate was obtained by rotating the IP drum. Figure 4-7(b) shows the intensity variation among eight IPs. These result show that the sensitivity is fairly uniform. The sensitivity data were found to be reproducible and used for further corrections of the detector with respect to the sensitive distributions.

The position resolution of the IP detector was estimated by measuring the profiles of the scattered X-ray beam through a fine slit of 20 μm width, which is placed 35 mm in front of the IP face. Under the conditions employed,

the scattered X-ray profile is uniform over the slit width of 20 μm. Thus if the IP detector has infinitely fine position resolution, the scattering profile recorded onto the IP through the slit should be a step function of width of 20 μm. However, the actually observed profile is a Gaussian function with full width at half maximum (FWHM) equal to 318 μm as shown by filed circles in Figure 4-8. This indicates that the position resolution of the IP detector P(d) is given by a Gaussian function, $P(d) = (2\pi\sigma^2)^{-1}\exp(-d^2/2\sigma^2)$ with σ = 135 μm along the horizontal direction. The resolution is as good as the 1D PSPC detector used in our studies.[12,15] The same resolution function was obtained in the vertical direction.

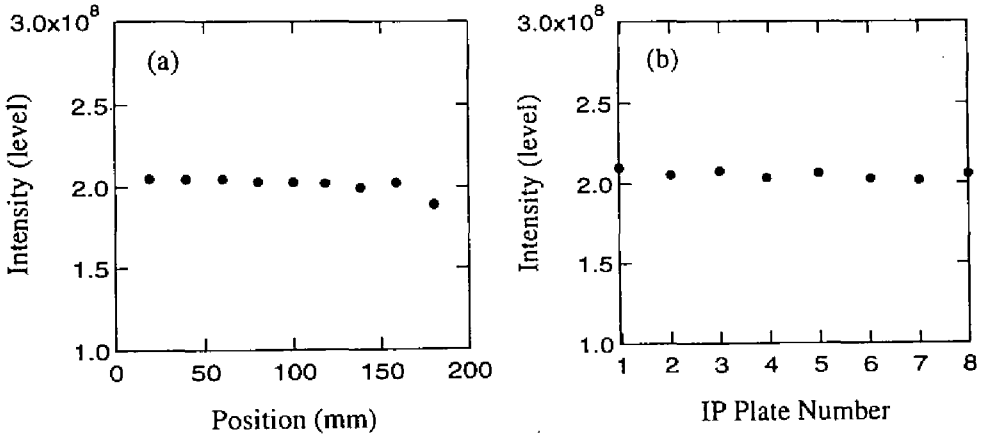

Figure 4-7. Uniformity of the sensitivity in a given IP (a) and that among eight IPs (b).

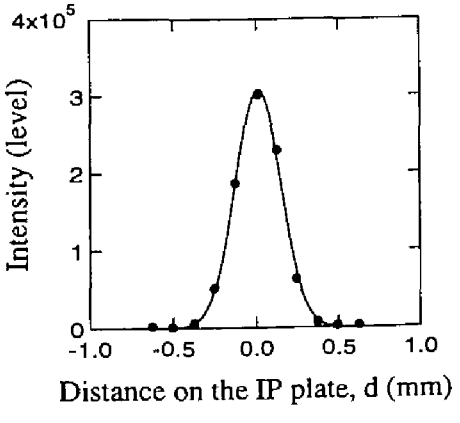

Figure 4-8. Determination of position resolution of the IP with a slit of width 20 μm. The position resolution is given by a Gaussian function with a standard deviation σ = 135 μm.

4-3. Time-Resolved SAXS AND WAXD Experiments in Applied Stress Field

In this section I show some applications of the IP detector for dynamic SAXS studies under oscillatory and transient stress fields.

Figure 4-9 shows a schematic diagram showing a typical time-resolved measurement under oscillatory shear strain using the IP system together with the timing charts of the experiment. This is a system newly developed in our laboratory in which the IP and the magnetic shutter (MS) are synchronized with the strain phase of the hydraulic sample deformation device through PC and controller. Details of the deformation device are described elsewhere.[12,13] As shown in part (a), the wave signal Ⓐ generated from the PC through the digital-to-analog converter (12 bits DAC) drives the actuator (DR) and imposes the strain on the sample (SP). The stress and strain are detected by the load cell (LC) and the linear variable differential transformer (LV), respectively, and recorded in the computer memory after analog-to-digital conversion (12 bits ADC). The ADC can convert up to 8 analog signals. Ordinarily the strain signal is sinusoidal and the strain phase in a cycle is divided into 64 channels as shown in Figure 4-9(c). Using these timing charts and operating MS on and off (Figures 4-9(a) for MS and the control signal Ⓑ and 4-9(d) for timing) and shifting the IP drum with respect to the incident beam (Figures 4-9(a) for the control signal Ⓒ and 4-9(e) for timing) synchronously with these timings, we can get, for example, 8 shots of the X-ray scattering profiles (i.e., 2D scattering patterns) in a strain cycle at every $\pi/4$ phase as shown in Figure 4-9(b) (see also the control signal Ⓐ in Figure 4-9(a). The stress and strain data are recorded at the middle point of each 64 phase. This sequence can be easily changed by

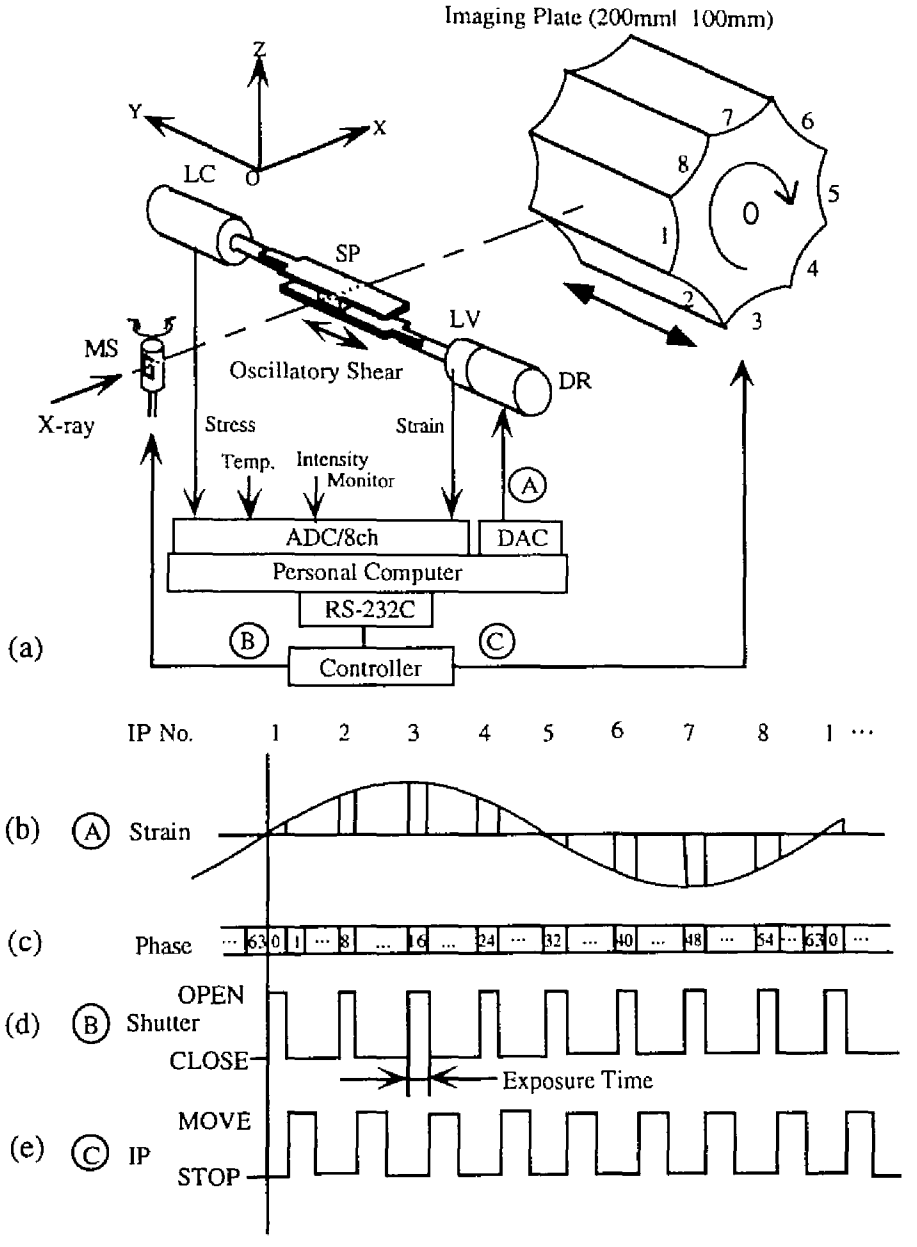

Figure 4-9. Schematic diagram showing a typical time-resolved SAXS and WAXD measurements under oscillatory shear strain using the IP system and the timing charts of the experiments. SP, sample; LC, load cell; LV, linear variable differential transformer; DR, actuator; MS, magnetic shutter; ADC, A/D converter; DAC, D/A converter.

rewriting the parameter file that is initially loaded to the computer.

Figure 4-10 shows the block diagram of the new time-resolved system. There are two computer systems ; one is associated with the IP system (system 1, i.e., the system including computer 1) already shown in Figure 4-5 and another is associated with the hydraulic sample deformation device and the analog data acquisition system (system 2 including computer 2). First we input the exposure time T for 2D X-ray scattering patterns and the number of strain phase N (at which 2D scattering patterns are recorded) into the IP system controller through system 1. Then we make System 1 wait for the shutter open timing pulse from System 2. The IP system is controlled according to this signal from system 2. For N up to 8, the IP drum moves only in a rotational direction, as shown in the bottom right corner of Figure 4-11. If $N \geq 9$, the IP drum should undergo both transverse and rotational shift, as shown in the bottom left corner of Figure 4-11; one IP should be divided into an appropriate number such that each division is used to record the 2D SAXS pattern at a given strain phase. We input the wave form data (shape, amplitude and frequency) and the data acquisition timing for the 2D SAXS pattern (through the wave and timing pulse generator) as well as the analog data (stress, strain incident X-ray beam intensity monitor, and temperature) into computer 2 in system 2. At the beginning of the experiment, the strain signal is converted into the analog data and the hydraulic sample deformation device is driven. The strain is imposed on the sample. System 2 controls the shutter opening pulse from DAC according to the program. Receiving this signal, System 1 opens the shutter and a SAXS pattern is measured on the IP for a fixed time. Immediately after the measurement, the IP is shifted to the next position. Again system 1 waits for the shutter opening pulse and the next sequence will start. In this way we can detect 2D scattering

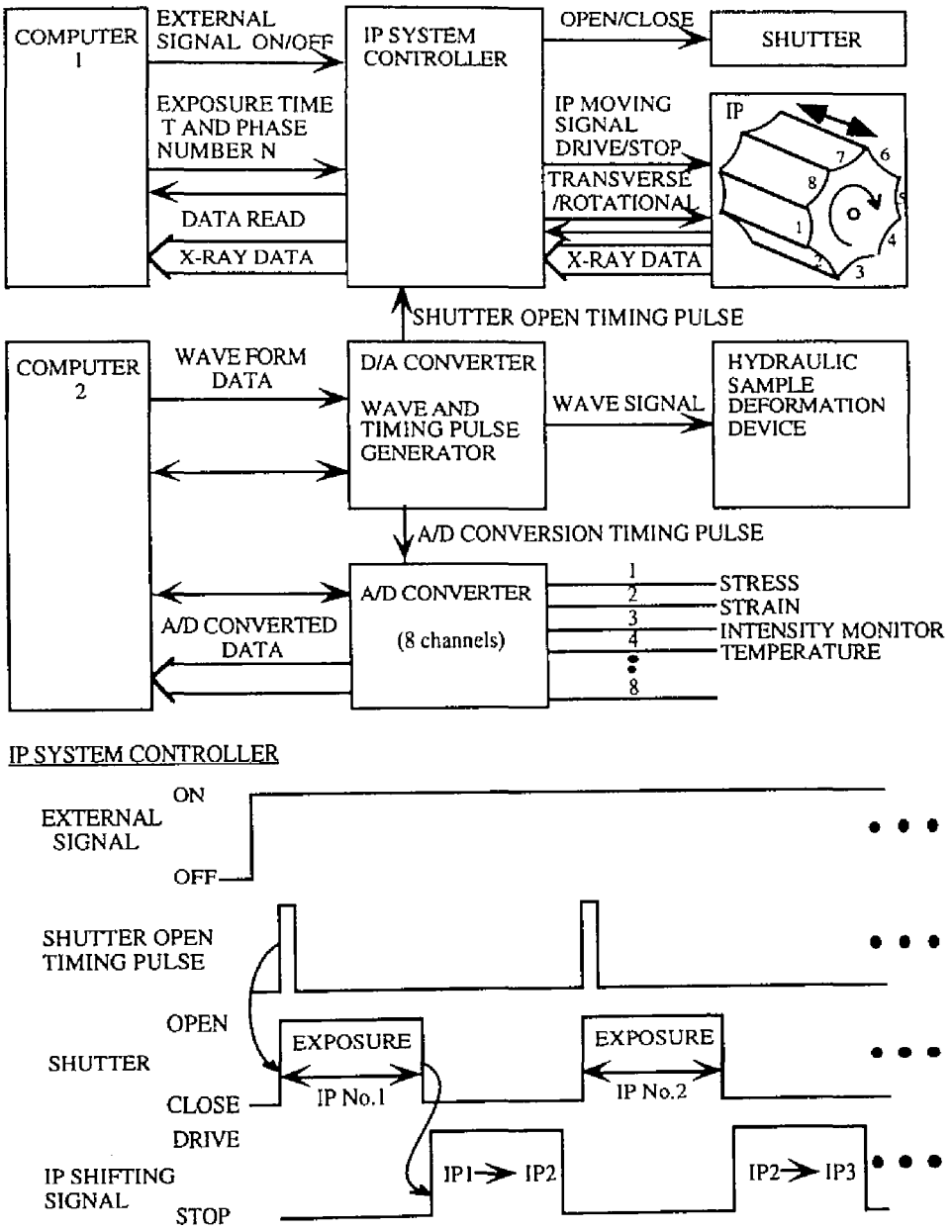

Figure 4-10. Block diagram showing the new time-resolved SAXS and WAXD apparatus with IP and the analog data acquisition system. The IP system is controlled by the signal from the hydraulic sample deformation device.

patterns on appropriate positions of the IP synchronously with strain phase over one cycle or repeatedly over M cycles to improve statistical accuracy of photon counting.

Figure 4-11 shows an example of timing charts used for a transient experiment. When the strain is rapidly imposed on the sample at time t, X-ray scattering patterns and the analog data are detected at the time of each sampling timing pulse Ⓒ and Ⓔ in Figure 4-11. After exposure, the exposed face is shifted according to the timing signal Ⓓ for shifting the IP. In the bottom part of the Figure 4-11 there are two examples of the IP-drum displacements. One is the transverse and rotational shift. Another is the rotational shift only. In the former example, the IP is divided into several parts, e.g., four. Then the size for a 2D scattering pattern is 50 mm wide × 100 mm long. Since the shifting speed in the transverse direction is 40 mm/s, it takes 1.25 s to shift from one exposure area to the next. After four exposures, the IP must be rotated to the new plate; no. 2. It takes 2 s. Again four exposures are performed on the new IP, and then the IP drum is rotated to the new IP. This action is repeated by the computer program. As there are eight plates in this system, we can get a maximum of 32 patterns in this case. The right-hand side in the bottom of Figure 4-11 shows an example of simple rotational shift.

Figure 4-12 shows the timing charts of the oscillatory experiment using a sinusoidal strain signal. In this case, 2D X-ray scattering patterns and analog data are obtained at every eight strain phase, among the 64 phases of one strain cycle. IP is driven by rotational shift only and the data obtained at the same strain phase are accumulated over many cycles onto the same IP plate.

Transient Experiment

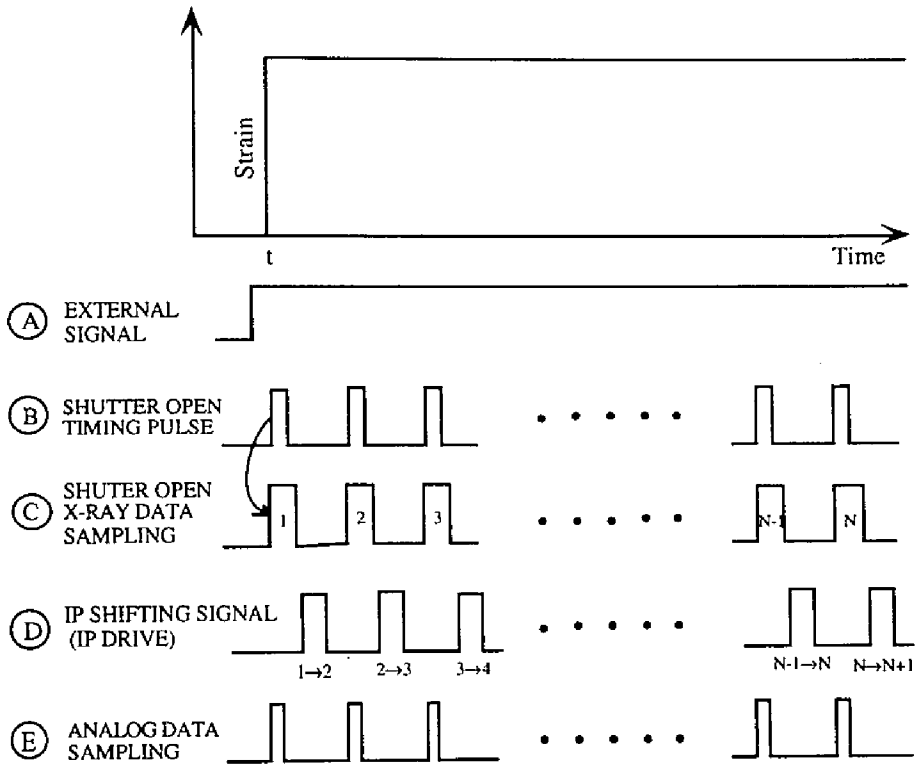

EXAMPLE OF IP SHIFT

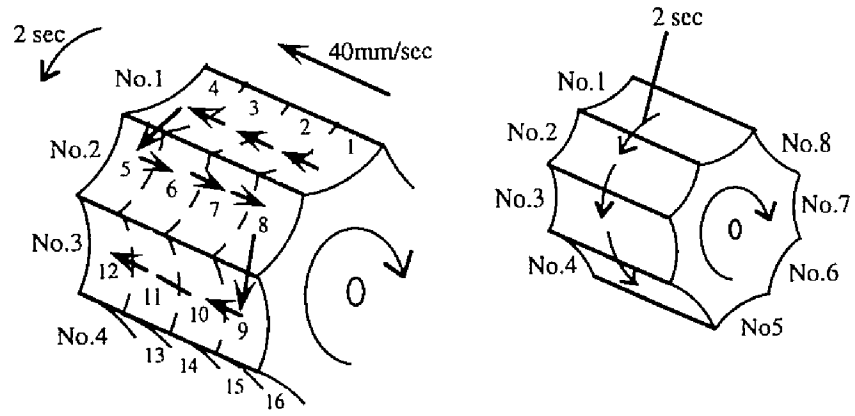

1. TRANSEVERSE AND ROTATIONAL SHIFT 2.ROTATIONAL SHIFT

Figure 4-11. Example of timing charts used for a transient experiment and schematic representation of how the IP detector is shifted. 1. The transverse and rotational shift. 2. The rotational shift only.

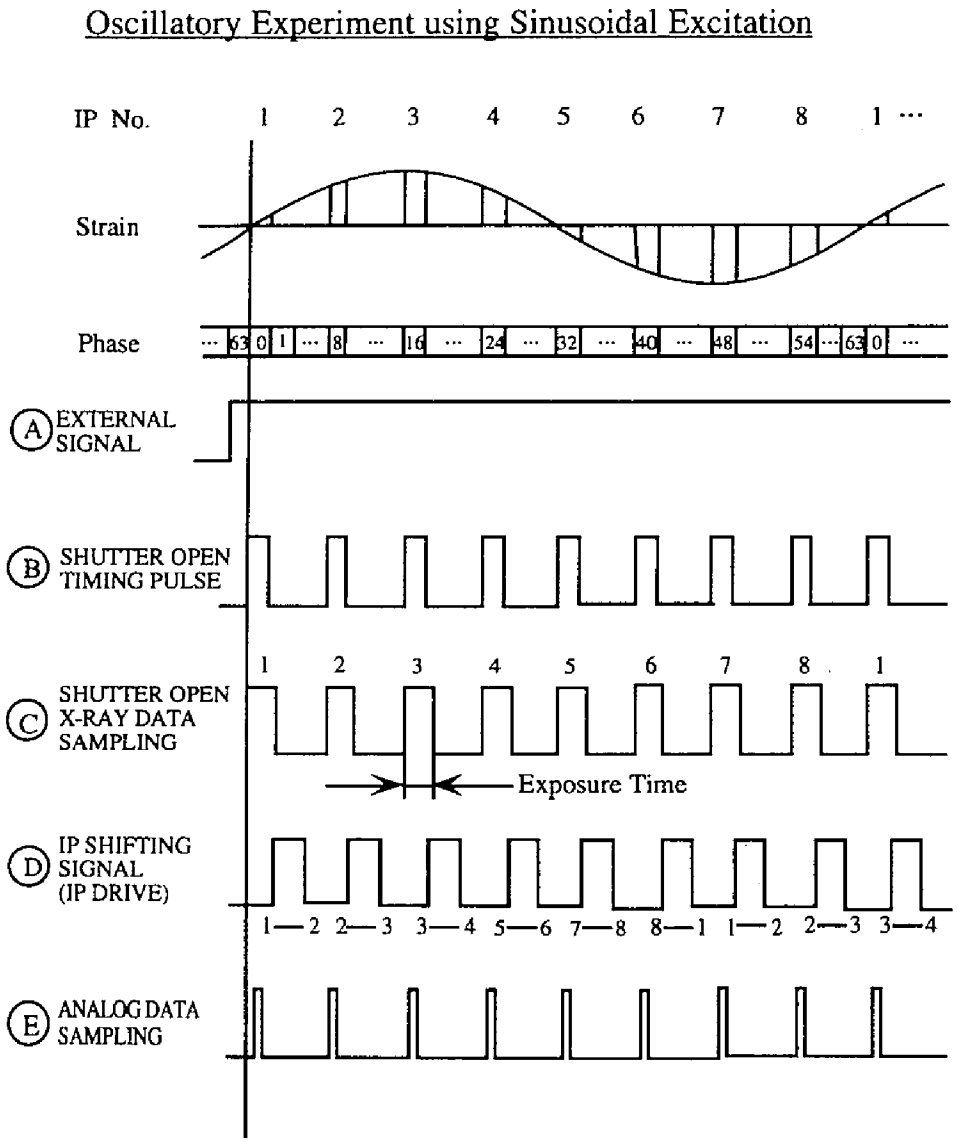

Figure 4-12. Example of timing charts used for the oscillatory experiment using a sinusoidal strain signal.

4-4. Applications

Figure 4-13(a) shows the time-evolution of SAXS patterns measured *in situ* during the isothermal crystallization of a crosslinked *cis*-1,4-polybutadiene rubber at draw ratio λ=2.5 and crystallization temperature T_c = -10 °C. In this experiment, the rubber with crosslinking density 1×10^{-4} mol/cm^3 [12,16,17] was first stretched at room temperature and subsequently cooled rapidly to -10 °C for the isothermal crystallization. The SAXS patterns were taken as a function of time. Each profile was measured with a 300 s exposure to X-rays. With increasing crystallization time, the two-point pattern oriented toward the stretching direction (SD) appears about 500 s after the crystallization. The two-point pattern shifts toward higher angles and the peak intensity increases with time. This indicates that, during the crystallization, the long period decreases as a results of the number of lamellar crystallites with time and that lamellar crystallites are regularly stacked with their lamellar normals oriented parallel to the SD. It is worth noting that the equilibrium crystallinity of the rubber at T_c = -10 °C is very low, ca 20% and hence the SAXS patterns have only weak intensity. Yet the SAXS patterns can be detected with a high sensitivity with this IP system.

Figure 4-13(b) shows the excess scattering pattern at 2130 s after onset of the crystallization which was obtained by subtracting the scattering pattern of the molten rubber at room temperature from the pattern in Figure 4-13(a) at 2130 s. The presence of the long period in the SAXS pattern is more clearly seen in Figure 4-13(b) after the correction for the background scattering. From this figure we can get the azimuthal angle dependence of the excess scattering patterns as shown in Figure 4-13(c). From such studies we can show that the orientation distribution of the lamellar normal is very sharp

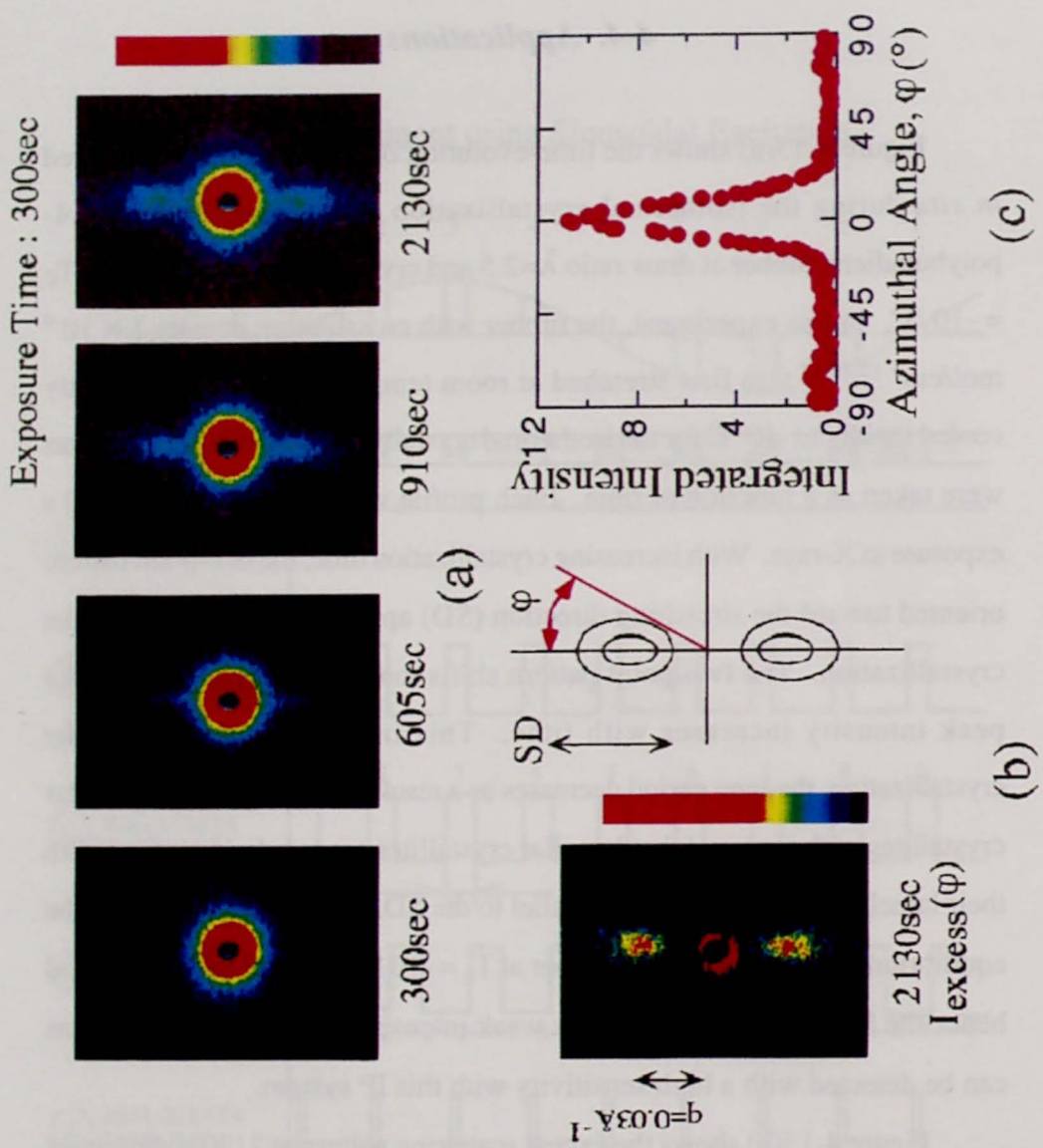

Figure 4-13. (a) A typical change in SAXS patterns measured in situ during the isothermal crystallization of the crosslinked *cis*-1,4-polybutadiene rubber at draw ratio $\lambda = 2.5$ and crystallization temperature $T_C = -10$ °C. (b) Excess scattering pattern obtained at 2130 s after onset of the crystallization which was obtained by subtracting the scattering pattern of the molten rubber at room temperature from the pattern of 2130 s in (a). (c) Azimuthal angle dependence of the excess scattering pattern (b) integrated with respect to q.

from the beginning of the crystallization. Further details of the studies will be reported elsewhere.[18]

Refferences

(1) Soda, M.; Takano, M.; Miyahara, J.; Kato, H. *Radiology* , **1983**, *148* , 833

(2) Kato, M.; Miyahara, J.; Takano, M. *Neurosurg. Rev.*, **1985**, *8* , 53

(3) Wakabayashi, K.; Amemiya, Y.; Tanaka, H. *in Proc. 11th Taniguchi Int Symp. Biophys.* (ed. T. Yanagida) Taniguchi Foundation, **1986**, 56

(4) Amemiya, Y.; Kojima, T.; Nomura, H.; Chikaishi, K.; Satow, Y.; Matsushita, T. *Photon Factory Activity Report*, **1986**, *4*, 306

(5) Amemiya, Y.; Wakabayashi, K.; Tanaka, H.; Ueno, Y.; Miyahara, J. *J.Science* , **1987**, *237* 164

(6) Dupont, Y.; Gabriel, M.; Chabre, M.; Guilk-Kryzywicki, T.; Schechter, E. *Nature*, **1972**, *238*, 331

(7) Schelten, J.; Hendricks, R. W. *J. Appl. Cryst.*, **1975**, *8*, 421

(8) Hashizume, H.; Nakajima, H.; Inoda, K.; Amemiya, Y.; Itoh, M.; Nishijima, T.; Kohara, K. *Jpn. J. Appl. Phys.*, **1976**, *15*, 2111

(9) Hendricks, R. W. *J. Appl. Crystallogr.*, **1978**, *11*, 15

(10) Schltz, J. M.; Lin, J. S.; Hendricks, R. W. *J. Appl. Crystallogr.*, **1978**, *11*, 551

(11) Matsushige, K.; Nagata, K.; Takemura, T. *Jpn. J. Appl. Phys.*, **1978**, *17*, 467

(12) Hashimoto, T.; Shibayama, M.; Saijo, K.; Suehiro, S.; Kawai, H. *Polymer J.*, **1981**, *13*, 501

(13) Suehiro, S.; Saijo, K.; Ohta, Y.; Hashimoto, T.; Kawai, H. *Analytica Chimica Acta*, **1986**, *189*, 41

(14) Hayashi, H.; Hamada, F.; Suehiro, S.; Masaki, N.; Ogawa, T.; Miyaji, H. *J. Appl. Crystallogr.*, **1988**, *21*, 330

(15) Fujimura, M.; Hashimoto, T.; Kawai, H. *Mem Fac Eng., Kyoto University* **1981**, *63*, 224

(16) Hashimoto, T.; Saijo, K.; Kosc, M.; Kawai, H.; Wasiak, A.; Ziabicki, A. *Macromolecules*, **1985**, *18*, 472

(17) Saijo, K.; Hashimoto, T. *Mat. Res. Soc. Symp. Proc.*, **1987**, *79*, 267

(18) Saijo, K.; Wasiak, A.; Hashimoto, T. in preparation

Chapter 5

Small-Angle X-ray Scattering Studies of a Cylinder-Forming Block Copolymer under Large Oscillatory Shear Deformation

5-1. Introduction

In this and the following chapters, the effects of mechanical stimuli on block copolymers were studied. In this chapter, I investigated the orientational change of the microdomain structures in a block copolymer after cessation of the deformation by the static measurements of SAXS with a two-dimensional detector presented in Chapter 4.

We used the same specimen as that employed in Chapter 1 which has cylindrical microdomains. As described in Chapter 1, we will distinguish between (1) the disordered structure, (2) the microphase-separated structure, (3) the grain network structure, and (4) the long-range order in which domain orientation and lattice orientation are uniform throughout the sample (~1-mm scale). A sample with such long-range order has been termed "single crystal".

Macroscopic orientation is achievable by flow. Keller et al.,[1] Hadziioannou et al.,[2] Pakula et al.,[3] Morrison et al.,[4,5] and Almdal et al.[6,7] demonstrated that shear can align the grain morphology and produce a "single crystal" structure. Long-range order can also be achieved by extensional flow.[8] In this study, we will use large-amplitude oscillatory shear (LAOS), which has been shown to generate a high degree of domain orientation.[2] LAOS was chosen since it can be applied slowly over long periods of time

and under good temperature control.

The strains for flow-induced ordering should be fairly small. A large imposed strain tends to disrupt the structure.[8,9] Large strains have been found to lower the shear viscosity in molten triblocks since they reduce the ratio of bridge to loop molecules; i.e., they reduce the probability of bridge molecules between separate domains and favor loop molecules which have both ends in the same domain.[10] These phenomena will be avoided here by choosing strains which do not exceed 4 shear units.

To date, techniques to produce long-range order have been mostly limited to applying deformation in the microphase-separated state. Shearing while cooling through ODT and below has been employed by Almdal et al.[7] for their study of ordering transitions in diblock copolymers.

Our approach is to thermally quench the sample from the single-phase state and anneal it at a constant quench depth ΔT just below ODT. Shearing is started immediately after the quench, and it is continued during annealing over a long time period. Shearing aligns the microphase-separated domains while they are growing. This structuring technique exploits the microphase-separating ordering kinetics, which is slowed down by the relatively high molecular weight of the polymer. After shear modification, both the rheology and morphology were investigated.

5-2. Experimental Section

5-2-1. Specimen

Polystyrene-*block*-polyisoprene-*block*-polystyrene (SIS) (designated as SIS-56) which is identical to the specimen used in Chapter 1, having an

equilibrium microphase-separated morphology of hexagonally packed cylinders of polystyrene (PS) in a polyisoprene (PI) matrix. The PI chains are much above and the PS chains are much below their entanglement molecular weight. T_{ODT} of the specimen was evaluated to be between $130 < T \leq 140$ °C in chapter 1. Cast films described in Chapter 1 was used for the experiments.

5-2-2. Small-Angle X-ray Scattering

SAXS experiments were performed with the apparatus described in Chapter 4. Two-dimensional SAXS was used for studying the order in the sheared samples. The SAXS patterns were corrected for sample absorption and air scattering. A newly developed image enhancement technique recovers higher order maxima. This will be discussed in conjunction with the results.

5-2-3. Rheometry

Dynamic mechanical properties were measured as described in Chapter 1 by RDS-7700, Rheometrics Co. Ltd., USA. Data analysis is also explained therein.

5-2-4. Transmission Electron Microscopy

The microdomain morphology of the SIS-56 specimen was investigated on the ultrathin films stained by osmium tetraoxide. Transmission Electron Microscopy (TEM) observation was carried out in the same manner as described in Chapter 2.

5-3. Results

5-3-1. Shearing at Constant Quench Depth

The as-cast material was mounted in the RDS-7700 and heated to 160 °C for 20 min in order to establish the disordered state. The sample was then cooled (at ~-5 K/min) to a temperature below the T_{ODT} and held there while large-amplitude oscillatory shear at a low frequency, $\omega = 0.01$ rad/s, and a shear strain amplitude, $\gamma = 4$, was applied. The required shearing time varied depending on the temperature. The four quench temperatures used were 125 °C for 10 h, 110 °C for 10 h, 100 °C for 4 h, and 80 °C for 2 h. The shear-induced domain orientation was investigated with birefringence, TEM, and SAXS, all done on room-temperature-cooled samples. Figure 5-1 shows the SAXS pictures of the 110 °C sample.

On the basis of the quiescent structuring observations, we first chose 125 °C as the annealing temperature for LAOS. However, no macroscopic orientation was seen, and even more importantly, there was no long-range order in the TEM image. The shearing process seemed to have disturbed the delicate microphase separation process. As the temperature for shearing was lowered, the driving force for phase separation increased and domain orientation was seen at an annealing temperature as low as 80 °C. An optimum temperature for the LAOS structuring seems to be ~110 °C. It provides sufficient molecular mobility and sufficient thermodynamic driving force for microphase separation.

Figure 5-1 contains the SAXS patterns taken along all three principal directions of the sample after LAOS at 110 °C. The pattern in Figure 5-1(a) is the diffraction intensity distribution in the plane passing through the origin of reciprocal space and parallel to the axes 3 and 2. Likewise, the pattern in

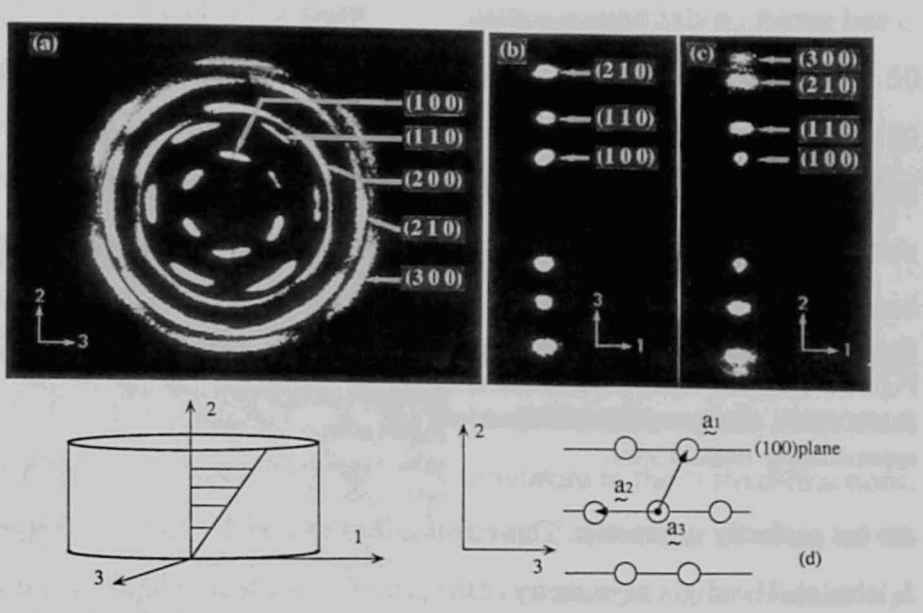

Figure 5-1. SAXS pattern after LAOS at 110 °C. Patterns (a)-(c) were obtained with the incident X-ray beam parallel to the 1-, 2-, and 3-axes of the shear flow, respectively.

Figure 5-1(b) belongs to the axes 1 and 3 and the pattern in Figure 5-1(c) to the axes 1 and 2. More rigorously, the pattern in Figure 5-1(c) presumably belongs to the plane parallel to axis 1 and line c. With the beam parallel to the flow direction, the 1-axis, Figure 5-1(a), shows a very sharp six-point pattern from (100) planes, indicating that the cylinders are aligned in the flow direction and packed with hexagonal symmetry in the plane perpendicular to the flow direction. Higher order diffractions from (110), (200), (210), and (300) were made visible by the following enhancement procedure:[11]

1. We divide the pattern into several concentric circles as is demonstrated in Figure 5-2, so that each of the concentric circles contains diffractions from equivalent planes.

2. The maximum intensity within each circle is normalized to 1. Then parts of the pattern with intensity levels between 0.5 and 1 are shown by

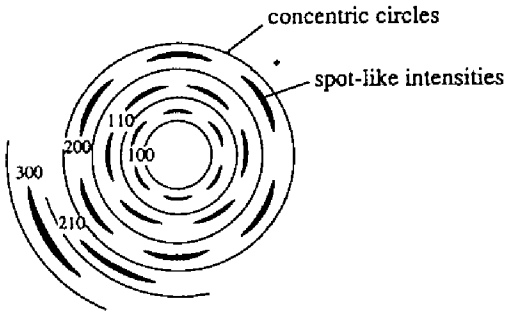

Figure 5-2. Schematic of the diffraction pattern in Figure 5-1(a). The relative intensities of (100), (110), (200), (210), and (300) diffractions are approximately 1000:20:3:2:1.

white color and the rest of the pattern is printed black (binarization). This allows comparison of intensity levels within each circle, but excluded comparisons of intensity levels between different circles.

The shape and intensity of the spots shown in Figure 5-1(a) are not perfectly symmetric. This effect is also seen in the patterns of Figures 5-1(b),(c). The slight asymmetry of the pattern is due to the slightly imperfect alignment of the specimen. The pattern was found to be very sensitive to how the specimens were cut from the sheared sheet and how they were mounted into the X-ray beam.

This same enhancement technique was also applied with the beam in normal and radial directions, the 2-axis and 3-axis views, respectively. Parts (b) and (c) of Figure 5-1 show only equatorial scattering normal to the flow axis 1, confirming that the cylinders are well aligned in the flow direction.

The equatorial distribution in the pattern in Figure 5-1(b) corresponds to the intensity distribution along line b in Figure 5-1(a). While (100) diffractions can be seen in the pattern in Figure 5-1(b), the corresponding diffraction cannot be seen along line b. However, this does not mean that there is no (100) diffraction along line b. In fact, the (100) diffraction intensity on line b is stronger than that of (110), though it is weaker than the (100) diffraction spots in off-equatorial positions. The fact that the (100) diffraction appears in Figure 5-1(b) and that its intensity is stronger than the (110) diffraction intensity is due to the orientational distribution of the hexagonal

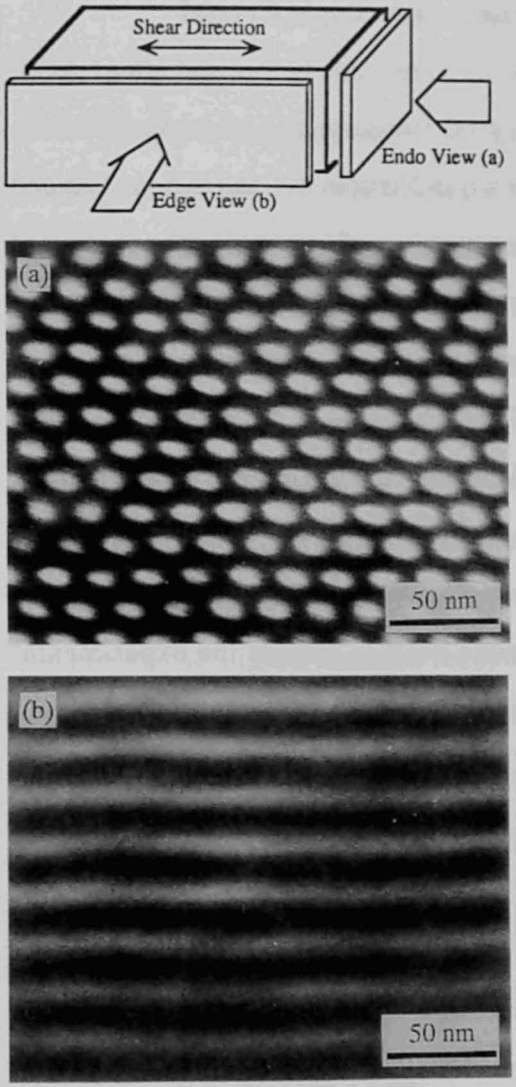

Figure 5-3. TEM of room-temperature sample after shearing at 110 °C; same sample as for Figure 5-1.

lattice around axis $\mathbf{a}_3$. Along line c, the (100) diffraction is about 50 times stronger than the (110) diffraction. Therefore, even a small fraction of cylinders with their primitive lattice vector $\mathbf{a}_1$ aligned parallel to the 2-axis may give rise to (100) diffractions which are dominant to the (110) diffractions, even if the major fraction of the lattice planes have an orientation as shown in Figure 5-1(d).

The equatorial intensity distribution in the pattern in Figure 5-1(c) corresponds to the intensity distribution along line c in Figure 5-1(a). Peak positions of the (100) diffractions are not symmetric, and this asymmetry is also seen along line c in pattern (5-1(a)). We attribute this asymmetry, and also the fact that (110) and (210) diffractions are found in addition to the (100) and (300) diffractions, to the imperfect alignment of the sample against the X-ray beam.

The periodic structure can also be seen in TEM; see Figure 5-3. The cylindrical domains show a slight undulation.

5-3-2. Linear Viscoelastic Properties of the Single Crystal

Linear viscoelastic measurements were made before and after LAOS. Frequency sweeps for the single crystal structure and isotropic structure (microphase well-separated) are shown in Figures 5-4 and 5-5, at 120 and 130 °C, respectively. The high-frequency values of G' and G" are not affected by the ordering process; i.e., these values are about the same for the single crystal structure and the as-cast morphology. At intermediate frequencies, the alignment somewhat reduces G' and increases G" when sheared in the direction of the cylindrical domains. However, the differences are quite small. The largest differences are seen at the lowest frequencies since the crossover to the terminal zone was shifted (shortening of the longest relaxation time of the plateau regime). The terminal zone itself is outside the experimental window so that it cannot be analyzed here.

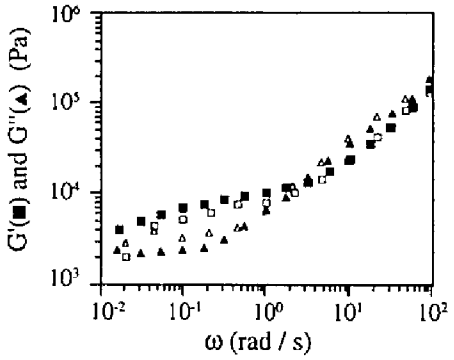

Figure 5-4. Frequency sweep at 120 °C after LAOS at 110 °C, unfilled symbols. The as-cast sample is represented by the filled symbols.

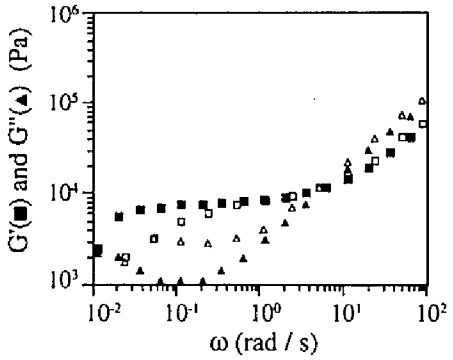

Figure 5-5. Frequency sweep at 130 °C after LAOS at 110 °C, unfilled symbols. The as-cast sample is represented by the filled symbols.

5-4. Discussion

LAOS is uniquely suited for slowly orienting the growing domains during microphase structure formation. The stress and strain vary sinusoidally, applying only high stress and strain for part of the cycle. As the cylindrical domains start to form and grow, the flow field supplies enough energy to influence the direction of domain formation. The cylindrical domains formed in the direction of flow give rise to smaller stresses than the domains perpendicular to flow, as we saw on separate measurements with a SBS triblock copolymer (not reported here). This lets us believe that the structuring is due to the merging of domains which are aligned with the flow direction and that these aligned domains remain unaltered by the flow. Newly formed small domains of different orientation can gradually reorient with the shear flow. The growth of large perpendicular domains, which would have to be broken up before aligning in flow direction,[8] are believed to be suppressed by the shear.

The cylindrical domains order into a hexagonal lattice structure. As was seen on SBS,[8] LAOS on SIS-56 has a strong tendency for aligning the (100) hexagonal lattice planes normal to the 2-axis of the shear flow; see Figure 5-1. The cylindrical domains in these lattice planes are part of the shear surfaces of the imposed shear flow. The favoring of this lattice alignment lets us conclude that it requires the lowest energy during shearing. A surface-induced ordering cannot be excluded, but it is highly unlikely for a sample thickness of 1 mm.

The flow-induced order is quite high, as can be seen by the narrow arcs of the diffraction patterns in Figure 5-1. If it were perfect as shown in Figure 5-1(d), (100) diffractions should not be seen in Figure 5-1(b) since

the (100) planes do not satisfy the diffraction conditions. However, we found (100) and (210) diffractions in addition to the (110) diffractions. This is attributed to slight imperfections in the order and to difficulties in specimen alignment with the X-ray beam.

It was quite unexpected that a shearing temperature near T_{ODT} (~10 K below) did not give sufficient structuring while a lower temperature produced the desired structuring effect. It seems that the development of the microphase-separated structure was suppressed or kept at extremely small scale by the LAOS and the room-temperature quenched samples showed no noticeable order in TEM and SAXS. However, even in the event that shear disturbed the microphase separation at 125 °C, the microphase separation should have developed a microdomain morphology after cessation of shear flow and during cooling of the specimen. Such microdomain morphology did not show under TEM. This compares to an earlier observation in which application of strong mechanical disturbances to a similar system at T > 120 °C, such as constant shear stress to large strains ($\gamma > 20$), permanently altered the degree of microphase separation.[5]

5-5. Conclusion

The rapid microphase separation and the slow development of extended domains provide suitable conditions for shear alignment of the developing morphology. Shear flow prescribes the direction in which the cylindrical domains prefer to grow and hexagon planes prefer to align. The director is uniform for the growing grain morphology; i.e., grain boundaries are avoided. The flow-induced ordering is optimum at an intermediate temperature. The temperature must be sufficiently far below T_{ODT} so that induced microphase

separation is strong, but the temperature must also be high enough to maintain sufficient molecular mobility. The suppression of microphase separation by shearing at small quench depth is an unexpected result which was not the objective of this study. It is a most interesting phenomenon which will require further study.

References

(1) Keller, A.; Pedemonte, E.; Willmouth, F. M. *Nature* **1970**, *225*, 538.

(2) Hadziioannou, G.; Mathi s, A.; Skoulios, A. *Colloid Polym. Sci.* **1979**, *257*,136.

(3) Pakula, T.; Saijo, K.; Kawai, H.; Hashimoto, T. *Macromolecules*, **1985**, *18*, 1294.

(4) Morrison, F. A.; Winter, H. H. *Macromolecules*, **1989**, *22*, 3533.

(5) Morrison, F. A.; Winter, H. H.; Gronski, W.; Barnes, J. D. *Macromolecules*, **1990**, *23*, 4200.

(6) Almdal, K.; Bates, F.; Mortensen, K. J. *J. Chem. Phys.*, **1992**, *96*, 9122.

(6) Almdal, K.; Koppi, K. A.; Bates, F. S.; Mortensen, K. J. *Macromolecules*, **1992**, *25*, 1743.

(8) Scott, D. B.; Waddon, A. J.; Lin, Y. G.; Karasz, F. E.; Winter H. H. *Macromolecules*, **1992**, *25*, 4175.

(9) Kraus, G.; Naylor, F.E.; Rollamnn, K. W. *J. Polym.Sci., Polym. Phys. Ed.*, **1971**, *9*, 1839.

(10) Lin, Y. G.; Zhou, R.; Chien, J. C. W.; Winter, H. H. *Macromolecules*, **1988**, *21*, 2014.

(11) Hashimoto, T.; Saijo, K.; Okamoto, S.; Kume, T., to be submitted for publication.

Chapter 6

Small-Angle X-ray Scattering Studies of a Lamella-Forming Block Copolymer under Large Oscillatory Shear Deformation

6-1. Introduction

According to the result in Chapter 5, large-amplitude oscillartory shear (LAOS) is uniquely suited for slowly orienting the growing domains during microphase structure formation, and has a strong tendency for aligning the (100) hexagonal lattice planes of cylindrical microdomains parallel to the shear plane. The experiment was conducted in the weak segregation limit near order-disorder transition (ODT) temperature. In this chapter, the specimen having lamellar microdomains was subjected to a large amplitude of sawtooth type oscillatory shear strain in the very strong segregation limit far below the order-disorder transition temperature, and ***in situ*** observation during the shear deformation and during relaxation upon cessation of shear was carried out with a 2D detector described in Chapter 4.

Investigation of the self-assembly of block copolymers (self-assembling processes and mechanisms, and structures self-assembled in equilibrium or non-equilibrium) provides a fascinating research theme in statistical mechanics of complex fluids. The investigation is important also from a viewpoint of controlling "**nanopattern**", as the copolymers can form ordered patterns of a nanometer scale. Most of the works along this line so far have been done for the copolymer systems without applied fields.[1,2] An extension of the above studies for the systems subjected to applied fields provides a

theme one-step advanced; it involves intriguing problems on open, non-equilibrium systems. Steady-state or transient nanopatterns developed are expected to be extremely rich in their varieties.

The effect of flow on such nanopatterns as lamellar and cylindrical morphologies was first demonstrated by Keller et al.[3] They showed it gives rise to highly aligned lamellae or cylinders for polystyrene-*block*-polybutadiene-*block*-polystyrene (SBS) copolymer melts. Subsequently, Hadziioannou et al.[4] obtained comparable results with polystyrene-*block*-polyisoprene (SI) and polystyrene-*block*-polyisoprene-*block*-polystyrene (SIS) using oscillatory shear deformation. These studies were extended to detailed studies on the deformation behavior of the block copolymer microdomains as studied by TEM, SAXS and birefringence.[5,6] More recently, there have been many experimental reports published on the shear-induced orientation of cylindrical[7-11] and lamellar microdomains.[12,13] The shear effects are also discussed on lattice orientation and deformation of the spherical microdomains.[14,15] The shear affects the phase transition also, as reported on the shear-induced disorder-to-order transition.[16,17]

In this work I focus on the effect of large amplitude oscillatory shear deformation on orientations of lamellar microdomains developed in a polystyrene-*block*-poly(ethylene-*alt*-propylene) diblock copolymer (SEP). The effect of shear deformation or flow on the lamellar microdomains was previously reported by Koppi et al.[12] and Winey et al.[13] They reported the unique "perpendicular orientation" of lamellae under the reciprocating shear deformation at high frequencies and at temperatures (T) close to but below the order-disorder transition (ODT) temperature (T_{ODT}), or the normal "parallel orientation" of lamellae at the same T but at the low frequencies or

at T far below T_{ODT} irrespectively of frequencies. The perpendicular orientation shows the lamellar normals **l** preferentially oriented parallel to the neutral axis of the shear deformation (OX axis), while the parallel orientation shows **l** preferentially oriented parallel to the shear gradient direction (OZ axis) (see Figure 6-1). Koppi et al. reported the experiments at T = 356K for a PEP-PEE block copolymer having T_{ODT} = 369 K (T/T_{ODT} = 0.97 or χ_{ODT}/χ = 0.98) or at T = 423 K for a copolymer having T_{ODT} = 564 K (T/T_{ODT} = 0.75 or χ_{ODT}/χ = 0.78), while Winey et al. reported the experiments at T = 371K and 417K for a SI diblock copolymer having T_{ODT} = 425K, corresponding to T/T_{ODT} = 0.87 or χ_{ODT}/χ = 0.79, and T/T_{ODT} = 0.98 or χ_{ODT}/χ = 0.97, respectively.

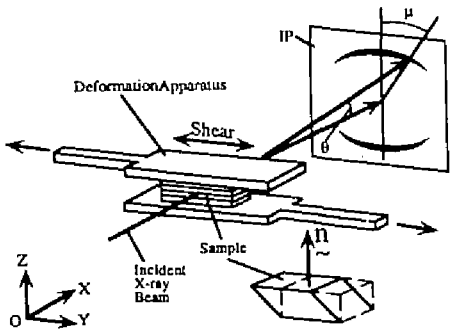

Figure 6-1. Optical setup of the SAXS apparatus used in this work where an imaging plate (IP) was used as a 2D detector. The Cartesian coordinate OXYZ is defined such that OX and OZ are parallel to the incident X-ray beam and the vertical direction of the apparatus, respectively, except for Figure 6-11 in which the beam was irradiated along OX, OY and OZ. A sawtooth type large-amplitude oscillatory shear deformation with a frequency of 0.0149 or 1 Hz is imposed with the shear displacement vector parallel to the OY axis. The unit vector **n** normal to the specimen surfaces is set normal to the OXY plane. θ and μ are a scattering angle and an azimuthal angle, respectively.

In this Chapter, I aim to report a new class of information on the effects of large-amplitude shear deformation on a lamellar orientation: shearing at a low temperature or in an even high segregation regime develops a ***biaxial orientation*** of lamellae as shown in Figure 6-10. It is also important to note that all our SAXS data, except those shown in Figure 6-11, were obtained ***in situ*** during the shear deformation and during relaxation upon cessation of shear, whereas previous works reported[12,13] were not done ***in situ***, involving additional processes such as

cooling, cutting and mounting the sample specimens having been subjected to the shearing at a given T and frequency f for the SAXS and SANS (small-angle neutron scattering) experiments. Only a few scattering experiments[10,15-17] have been carried out *in situ*, despite the necessity of doing the *in situ* experiments to avoid any artifacts encountered by the additional processes. Here we shall report some of our initial experimental results, especially anomalous biaxial orientation of lamellae. The detailed interpretation of the reorientation mechanism will be left as a future work.

6-2. Experimental Section

6-2-1. Specimen

The SEP sample (designated as SEP-34/32) was kindly supplied from Kuraray Co. Ltd., Japan. It was prepared by selective hydrogenation[18] of the polyisoprene block of a precursor SI diblock copolymer prepared by living anionic polymerization. It has a number-average molecular weight $M_n = 3.2\times10^4$, heterogeneity index $M_w/M_n = 1.5$ where M_w is weight-average molecular weight, and weight fraction of PS of 0.37. The polyisoprene block before hydrogenation had a microstructure rich in 1,4-linkage (95 %). Film specimens were prepared by the solution-cast method with toluene as described in Chapter 1. The films thus obtained were dried under vacuum at 30 °C until a constant weight was attained, and subsequently annealed at 30 °C for 2 days, prior to the use for real time and *in situ* studies.

6-2-2. Dynamic SAXS Apparatus

2D small-angle X-ray scattering patterns from the sheared specimen were obtained with the imaging plate (IP) system. The details of the IP system

was reported in Chapter 4.[19] The Cartesian coordinate OXYZ is defined such that the OX- and OZ-axes are parallel to the incident X-ray beam and the vertical direction of the apparatus, respectively.

The oscillatory shear strain was imposed on the film specimen as shown in Figure 6-1. The specimen was subjected to a large amplitude of sawtooth type shear strain γ with amplitude $\gamma_0 = 50$ % and frequency f = 0.0149 or 1 Hz at a temperature T = 105 or 130 °C (γ varies between $\pm\gamma_0$). The specimen surfaces are set parallel to OXY plane with the specimen normal **n** parallel to the OZ axis, and sandwiched between two metal plates with the shear displacement direction along OY axis. Unless otherwise stated, the incident X-ray beam was irradiated parallel to OX axis and the shear strain $\gamma = dy/dz$ existed in the plane OYZ. The oscillatory deformation was driven by a hydraulic deformation apparatus whose details on the computer-controlled data-acquisitions and the machine-operations were given in Chapter 4.[15,20] We employed the graphic enhancement technique for 2D SAXS patterns described in Chapter 5[21] in order to facilitate a visual inspection of their higher order maximum intensity distributions with respect to an azimuthal angle μ also defined in Figure 6-1.

6-2-3. Transmission Electron Microscopy

Transmission electron microscopy (TEM) was conducted in the same way as described in Chapter 2.

6-2-4. Rheometry

Dynamic mechanical properties and stress relaxation of the specimens were measured by RDS 7700-II, Rheometrics Co. Ltd., USA.

6-3. Results

6-3-1. Characterization of Undeformed State

Figure 6-2 shows a typical TEM micrograph obtained from SEP-34/32. It shows a mosaic structure consisting of grains of lamellar microdomain with different orientation. The bright phase corresponds to the microdomains composed of poly(ethylene-*alt*-propylene) block chains (PEP), while the dark phase corresponds to that of polystyrene block chains (PS) selectively stained

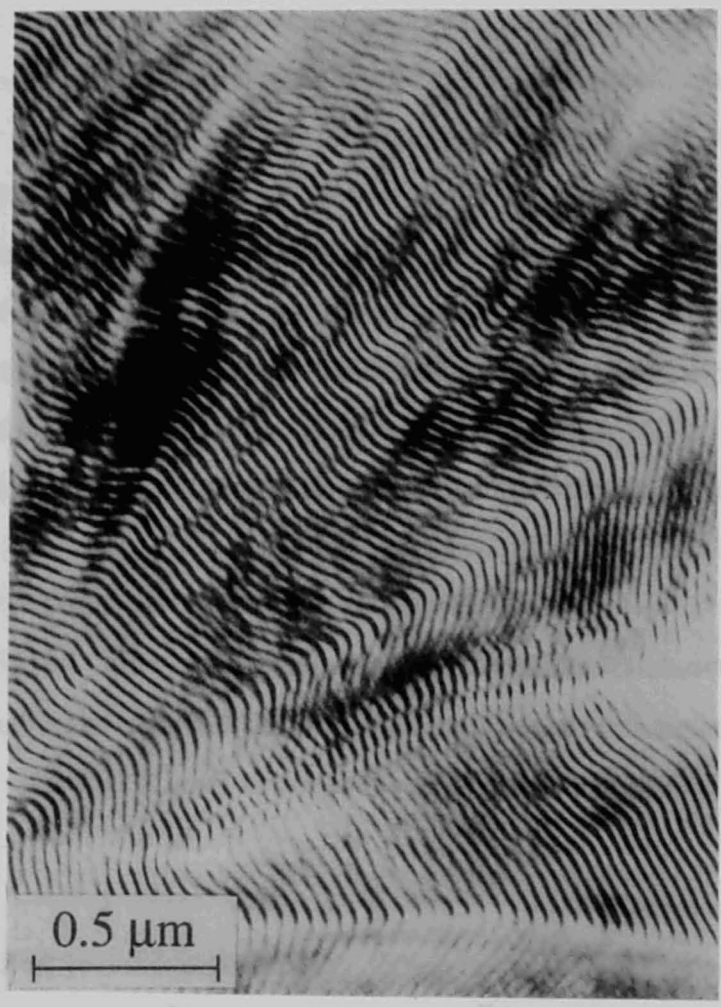

Figure 6-2. Typical TEM micrograph for undeformed SEP specimens ultramicrotomed and stained with RuO_4. The micrograph shows the grain structure whose grain-boundary structure is given by Scherk's first surface.

by RuO_4. This specimen contains a numerous number of grain boundaries with various types of interesting TEM images, whose details were analyzed and discussed elsewhere[22] for a similar SEP system showing the lamellar microdomain morphology.

An average grain size is roughly estimated as follows. The size of the grain parallel to the lamellar interface, i.e., the average span of the straight lamellae, is a few micrometers, while the size of the grain normal to the lamellar interface is several times larger than this. Our analysis indicated that all the grain-boundary images are explained by and large in terms of the minimal surface, designated Scherk's first surface.[23,24] Through this surface, a set of the PS and PEP lamellae with a given orientation is connected smoothly to another set of the corresponding lamellae having a different orientation without intersections of dissimilar lamellae, i.e., the PS (PEP) lamellae in a given set being connected to the PS (PEP) lamellae in another set. Thus the lamellae have 3D continuity through this type of grain-boundary.

Figure 6-3 shows the SAXS pattern for the undeformed specimen, taken with IP using the configuration as indicated in the Cartesian coordinate attached to the figure. The pattern indicates a preferential orientation of the lamellar normals **l** with respect to the film normals **n**. The preferential orientation is more quantitatively shown by the azimuthal angle (μ) dependence of the first-order and the second-order scattering maxima, as shown in Figure 6-4. Here $\mathcal{J}(\mu)$ designates integrated SAXS intensity distribution as a function of μ, defined by

$$\mathcal{J}(\mu) = \int_{q_1}^{q_2} I(q,\mu) q^2 dq \qquad (6\text{-}1)$$

where q_1 and q_2 are the q-values at the lower and upper bounds of the first-

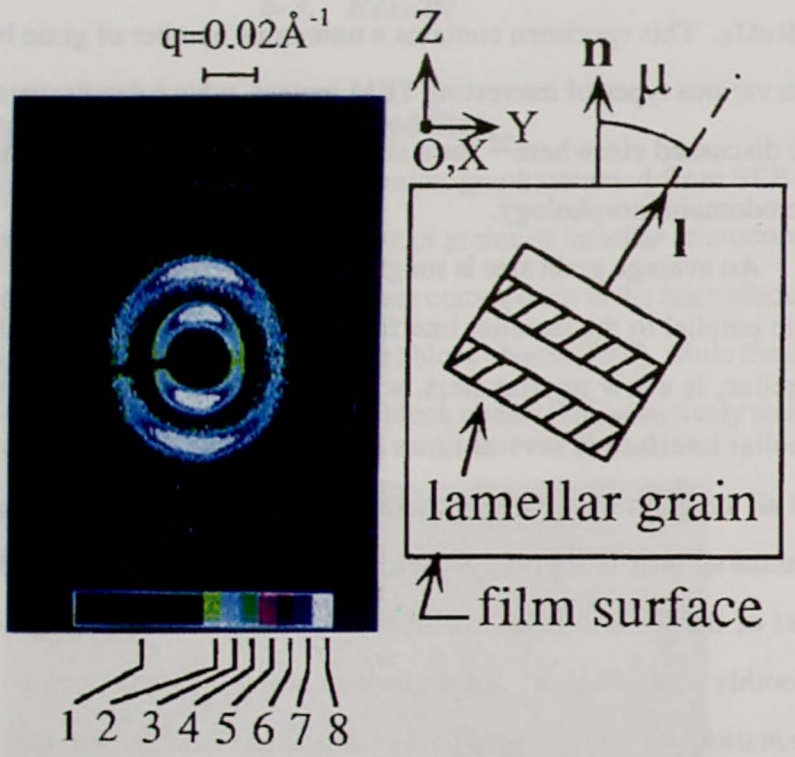

Figure 6-3. 2D SAXS pattern for undeformed SEP specimens. **n** and **l** are unit vectors parallel to the film normal and lamellar normal, respectively. Note that a direct-beam stopper interferes with the left half of the pattern in the near equatorial direction, giving rise to an abrupt intensity drop along the scattering ring. The same effect is seen also in Figure 6-8. The intensity ratio of the second-order maximum relative to that of the first-order maximum is approximately 1/15. The eight different colors in the bar, attached at the bottom of the pattern, indicate scattering intensity levels in a linear scale that were used in the graphic enhancement procedure, where each color bar corresponds to each intensity level interval (1-8 correspond to 0-0.61, 0.61-0.67, 0.67-0.72, 0.72-0.78, 0.78-0.83, 0.83-0.89, 0.89-0.94, and 0.94-1.0, relatively to the intensity maximum).

order maximum or the second-order maximum. If the lamellar normal **l** has a uniaxially symmetric orientation distribution with respect to the film normal, i.e., OZ axis, its normalized orientation distribution function $N(\mu)$ can be obtained by

$$N(\mu) = \mathcal{J}(\mu) / \int_0^{\pi} \int_{q_1}^{q_2} I(q,\mu) q^2 \sin\mu \, dq \, d\mu \qquad (6\text{-}2)$$

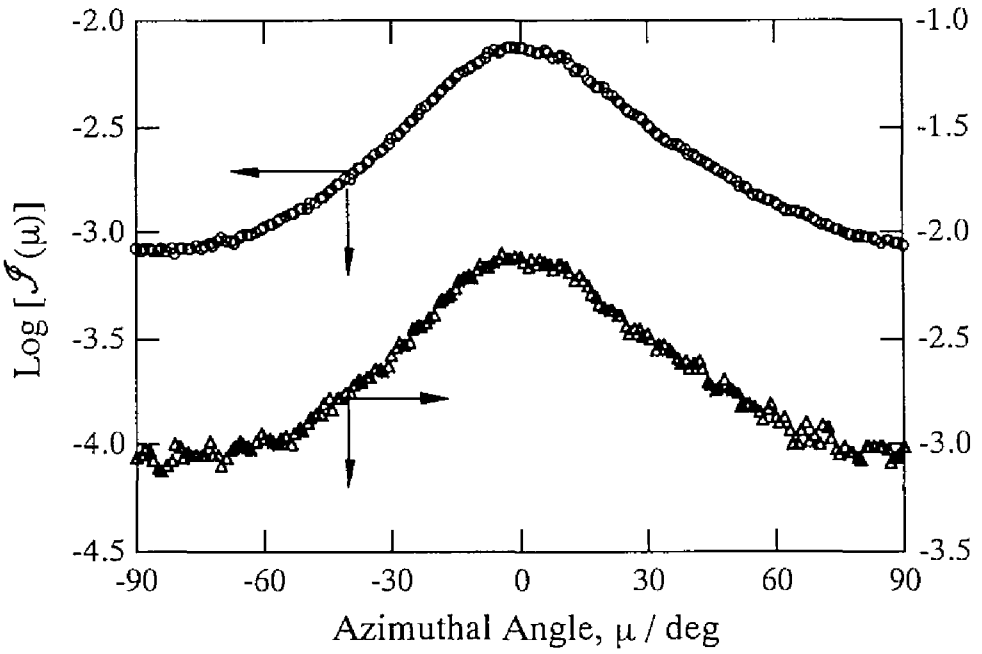

Figure 6-4. Azimuthal angle (μ) dependence of the first- and second-order diffraction maxima for the pattern shown in Figure 6-3, ωιτη μ = 0 being taken parallel to the OZ axis.

The second-order orientation factor f defined by

$$f \equiv [3 < \cos^2 \mu > -1]/2 \tag{6-3}$$

can be estimated from N(μ), i.e.,

$$< \cos^2 \mu > \equiv \int_0^{\pi} \cos^2 \mu N(\mu) \sin \mu d\mu \tag{6-4}$$

The initial state of our sample before shear deformation had the uniaxial orientation of I with respect to OZ axis, and its orientation factor f was estimated to be 0.31 from the data $\mathcal{F}(\mu)$ shown in Figure 6-4 and from eqs 6-1 to 6-4.

Figure 6-5 shows the meridional scattering intensity distribution parallel to the film normal as a function of scattering vector q = (4π/λ) sin(θ/2), θ

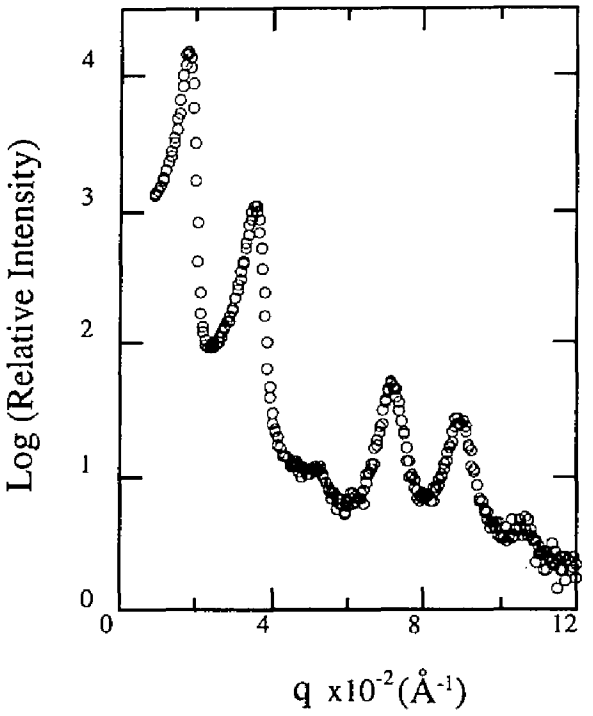

Figure 6-5. SAXS intensity distribution along the OZ direction in the pattern shown in Figure 6-3.

being the scattering angle. The profile shows a multiple-order scattering maxima up to at least the eighth-order maximum, each at the position of integer multiples of the first-order peak position, though the figure includes only up to the sixth-order maximum. This implies a small paracrystalline distortion factor.[25] Based on the paracrystal model described in Chapter 2, we estimated g (= $\Delta D / \overline{D}$) and obtained g ≅ 0.04. This implies a high regularity in the spatial arrangement of the lamellae. Here ΔD is the standard deviation of the interlamellar spacing D from the mean value $\overline{D}$ = 35.9 nm estimated from the Bragg equation: $2\overline{D}\sin(\theta/2) = m\lambda$ and m is integer related to the order of diffraction. The suppression of the third-order maximum is due to the fact that the form factor of the PS lamellae becomes close to zero at the corresponding q value, which yields the volume fraction of the PS

lamellae $\phi_{PS} \cong 1/3$. This value is close to the one as calculated from the fraction of PS in SEP-34/32 on the assumption of complete segregation between PS and PEP ($\phi_{PS} = 0.34$).

6-3-2. Mechanical Properties

Figure 6-6 shows stress relaxation at the two measuring temperatures 105 and 130 °C after rapidly imposing shear strain $\gamma = 100$ % within 10 μs in which the shear modulus G (Pa) was plotted against t(s) in double logarithmic

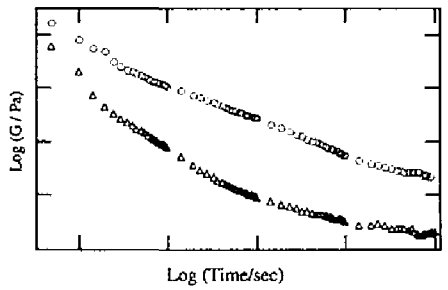

Figure 6-6. Stress relaxation after a rapid, large shear deformation at 105 and 130 °C. The large deformation of $\gamma = 100$ % was attained in the time interval of 10 μs.

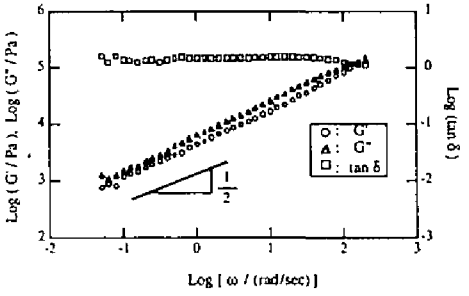

Figure 6-7. Linear dynamic mechanical response at 130 °C obtained for strain amplitude 1 % and static strain 0 %.

scale. Figure 6-7 shows linear dynamic mechanical response measured at 130 °C with dynamic strain amplitude 1 % and static strain 0 % where real and imaginary parts of the shear moduli, G' and G" respectively, as well as loss tangent tan δ were plotted against angular frequency ω in a double logarithmic scale. The data at 105 °C were not shown here but their low frequency behaviors are the same as those at 130 °C except for a difference in the modulus level. The power-law behaviors of G' and G'' at the low frequency limit are typical to the ordered microdomains.[8,15,26-29]

6-3-3. Effects of Large Amplitude Oscillatory Shear Deformation

Figure 6-8 shows effects of the large amplitude shear deformation at low frequency and at low temperature, i.e., f = 0.0149 Hz and T = 105 °C. Pattern (a) was taken *in situ* at 105 °C before the shear deformation, while patterns (b) and (c) were taken *in situ* during the deformation, in the deformation cycles N between 1 and 15 and between 75 and 89, respectively. One cycle corresponds to 67 s. On the other hand, patterns (d) and (e) were obtained between 0 and 1000 s and between 3000 and 4000 s, respectively, after cessation of shear, with the specimen having been subjected to the 89 cycles oscillatory deformation, i.e., the specimen giving rise to pattern (c). A main change of the pattern appears to occur for the first 1000 s after the oscillatory deformation being imposed, i.e., N = 1-15 after the deformation. The pattern obtained between N = 64 and 74 (not shown in the figure) was almost identical to pattern (c). Thus the pattern (c) appears to represent the steady state structure attained.

The effects of the shear on the patterns are seen in the following two main points: (i) The μ-dependence of the intensity shows a **biaxial orientation** of lamellar normals and (ii) with increasing N, the meridional scattering maxima (or diffraction spots along the OZ axis) have a sharper intensity distribution with respect to μ. The effects can be seen more clearly in Figure 6-12 later. Patterns (d) and (e) will be described later in Section 6-3-4. To our best knowledge, this evolution of the biaxial orientation was observed for the first time.

Figure 6-9 shows the effects of the large amplitude shear deformation at low frequency and at higher temperature, i.e., f = 0.0149 Hz and T = 130 °C. Pattern (a) was taken *in situ* at 130 °C before the shear deformation, while pattern (b) was taken in the time interval between 0 and 1000 s after

cessation of shear, at $\gamma = 0$, the sample having been subjected to the oscillations N = 1 - 60 (0 - 4020 s). Pattern (c) was taken as follows. After pattern (b) was taken, the specimen was rapidly cooled to 105 °C. The pattern was taken *in situ* at 105 °C in the time interval of 1000 - 2000 s after the quench from 130 to 105 °C. Pattern (c) will be described later in Section 6-3-4. The pattern obtained *in situ* during the oscillation was similar to that shown in pattern (b), except for the fact that the former is slightly broader than the latter in terms of the μ-dependence, due to the dynamical change of the pattern induced by the oscillation. The specimen sheared at the high temperature gives a sharper uniaxial orientation distribution with the lamellar normals parallel to OZ-axis than the undeformed specimen at 130 °C. However, it does not show the biaxial orientation at all. This result is consistent with previous results.[4,12,13] The azimuthal-angle dependence of the patterns will be shown more quantitatively in Figure 6-15, later.

Figure 6-10 shows effects of the shear deformation at high frequency and at the high temperature, i.e., f = 1 Hz and T = 130 °C. Pattern (a) was taken *in situ* at 130 °C before the deformation, while pattern (b) was taken *in situ* during the oscillation of N = 1-1000 (t = 0-1000 s). Patterns (c) and (d) were, respectively, obtained in the time intervals of 0 - 1000 s and 3000 - 4000 s after cessation of the oscillatory deformation of N = 1 - 4000. The results will be described in Section 6-3-4. The high frequency oscillation clearly gives rise to a **biaxial orientation** of the lamellar normals in the plane of OYZ, clearer than the case of f = 0.0149 Hz and T = 105 °C.

We next investigate a state of the biaxial orientation of the lamellar normals with respect to the Cartesian coordinate OXYZ. Figure 6-11 shows typical SAXS patterns taken with incident beam parallel to OX-axis [(a),

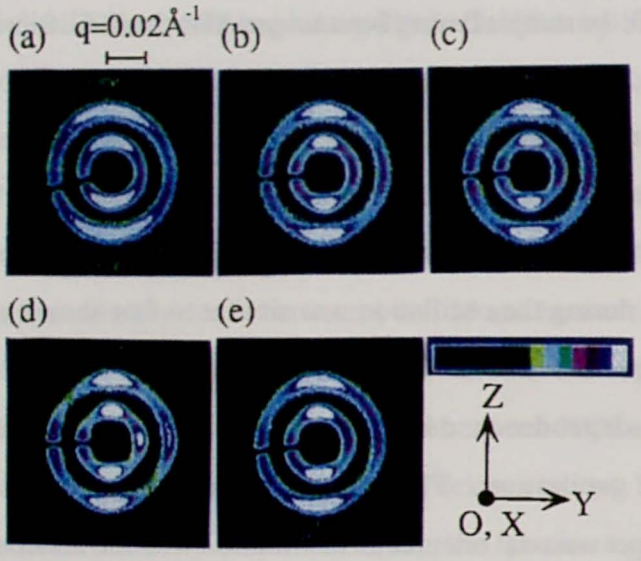

Figure 6-8. Effects of the large-amplitude oscillatory shear deformation at 0.0149 Hz and 105 °C on the SAXS patterns; (a) pattern for the undeformed specimen at 105 °C; (b and c) patterns taken *in situ* during oscillation cycles N = 1-15 and 75-89, respectively; (d and e) patterns taken *in situ* at 105 °C in the time interval of 0-1000 and 3000-4000 s after cessation of the shear deformation at $\gamma = 0$, respectively, from the state corresponding to that for pattern (c). The intensity ratio of the second-order maximum relative to that of the first-order maximum in the meridional direction is approximately 1/10. The eight different colors in the bar attached at the bottom of the pattern indicate scattering intensity levels in a linear scale that were used in the graphic enhancement procedure. Here the lower 60% of the intensity is represented by black and upper 40% is equally divided by 7 and represented by seven different colors, each having intensity 0-0.61, 0.61-0.67, 0.67-0.72, 0.72-0.78, 0.78-0.83, 0.83-0.89, 0.89-0.94, and 0.94-1.0, relatively to the intensity maximum. The same color representation of the intensity level was used for Figures 6-9 to 6-11.

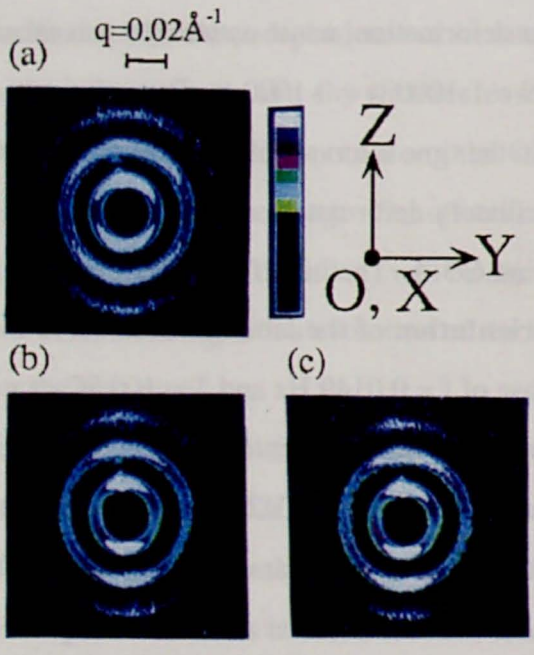

Figure 6-9. Effects of the large-amplitude oscillatory shear deformation at 0.0149 Hz and at 130 °C on the SAXS patterns; (a) pattern for the undeformed specimen at 130 °C; (b) pattern taken *in situ* at 130 °C in the time interval of 0-1000 after cessation of the oscillatory deformation of N= 60 at $\gamma = 0$; (c) pattern taken *in situ* at 105 °C in the time interval of 1000-2000 s after the specimen was first released from strain at 130 °C for 1000 s (pattern shown in part (b)) and then rapidly cooled to 105 °C. The intensity ratios of the second- and third-order maxima relative to that of the first-order maximum in the meridional direction are approximately 1/10 and 1/500. The eight different colors in the bar are explained in the caption of Figure 6-8.

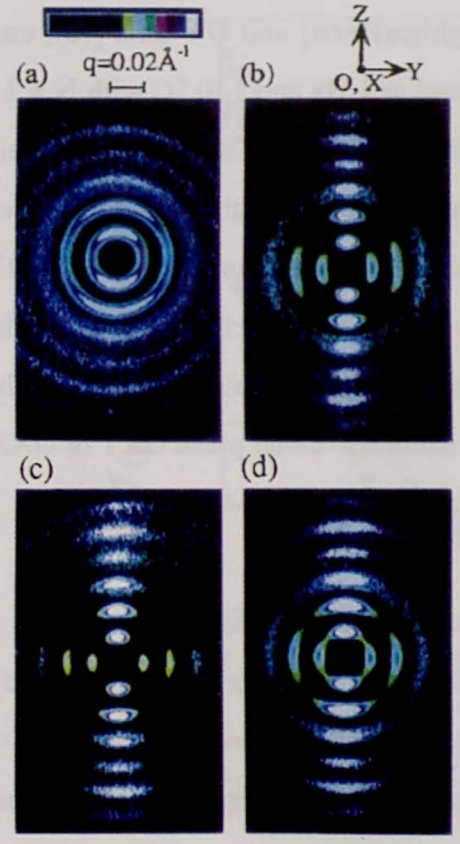

Figure 6-10. Effects of the large-amplitude oscillatory shear deformation at 1 Hz and at 130 °C on the SAXS patterns; (a) pattern for the undeformed specimen at 130 °C; (b) pattern taken *in situ* during the oscillation cycles N = 1-1000 s; (c and d) patterns taken *in situ* at 130 °C in the time interval of 0-1000 and 3000-4000 s after cessation of the shear deformation, at $\gamma = 0$, respectively, from the state corresponding to that for pattern (b). The intensity ratios of the second-, third-, fourth- and fifth-order maxima relative to that of the first-order maximum in the meridional direction are approximately 1/10, 1/250, 1/1200, and 1/1000. The eight different colors in the bar attached at the top of the pattern are explained in the caption of Figure 6-8.

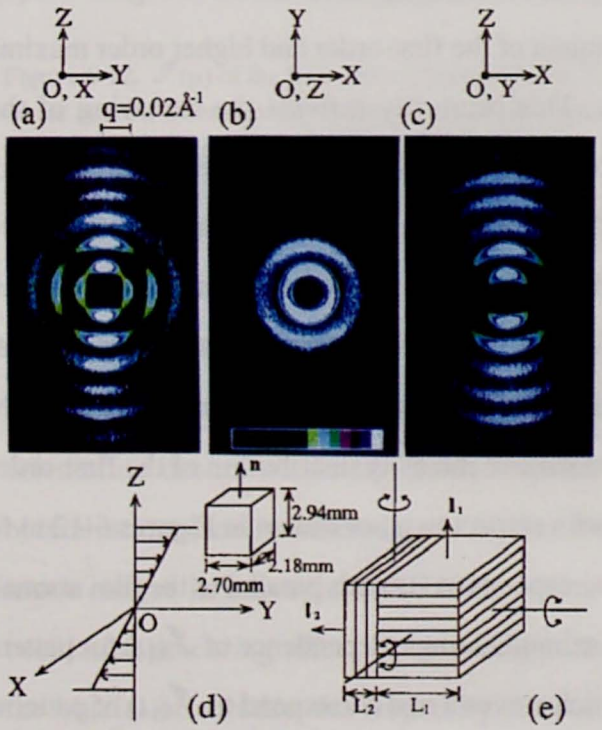

Figure 6-11. The SAXS patterns (a)-(c) for the specimens vitrified in the state corresponding to the pattern (d) in Figure 6-10. The patterns were taken from three directions as specified in part (d). Part (e) represents a model showing the lamellar orientation in the specimen. **n** specifies the film normal, while $\mathbf{l}_1$ and $\mathbf{l}_2$ specify the lamellar normals. The intensity ratios of the second-, third-, fourth- and fifth-order maxima relative to that of the first-order maximum in the meridional direction are approximately 1/10, 1/500, 1/400, and 1/500 for an edge pattern (pattern (a)), 1/10, 1/600, 1/600, 1/750 for an end pattern (pattern (c)), and 1/10 for a through pattern (pattern (b)). The eight different colors in the bar attached at the bottom of the pattern are explained in the caption of Figure 6-8.

edge pattern], OZ-axis [(b), **through pattern**] and OY-axis [(c), **end pattern**] for the specimen first deformed at 1 Hz and 130 °C with N = 1 - 4000 and then vitrified by quenching below T_g of the PS domains with liquid nitrogen. The relationship between the Cartesian coordinate and specimen is shown in part (d) with OZ axis parallel to the film normal **n** and the OY axis parallel to the shear displacement vector. Figure 6-11 (e) shows a model describing the biaxial orientation of the lamellar normals l_i (i = 1, 2) in the specimen with their interfaces oriented parallel to either plane OXY or OXZ. The detailed discussion will be given later in Section 6-4.

6-3-4. Relaxation of Orientation after Cessation of Shear

We now describe the change of the patterns shown in Figures 6-8 (d), (e), Figure 6-9 (c) and Figures 6-10 (c), (d) after cessation of shear at $\gamma = 0$. The pattern shown in Figure 6-8 (d), obtained at $\gamma = 0$ right after the cessation, shows a sharper biaxial orientation than the pattern shown in Figure 6-8 (c), is obvious from the sharp minima of the first-order and higher order maxima in the diagonal directions. This primarily reflects the smearing of the biaxiality in pattern (c) taken *in situ* during the oscillatory deformation, because the four spots (or diffraction maxima) along OY and OZ axes move with strain phase during oscillation. The same effect is seen in Figures 6-10 (b) and (c). The change of the lamellar orientation with shearing and that with time after cessation of the imposed shear deformation are more quantitatively seen in the normalized intensity distribution of the first-order scattering maximum $\mathcal{I}(\mu)$ with respect to μ, as shown in Figures 6-12 to 6-15. In these figures $\mu = 0°$ corresponds to OZ-axis parallel to the film normal.

Figure 6-12 shows the azimuthal-angle dependence of $\mathcal{I}(\mu)$ for pattern (a) to (d) in Figure 6-8, in which curves a to d correspond to $\mathcal{I}(\mu)$ of patterns

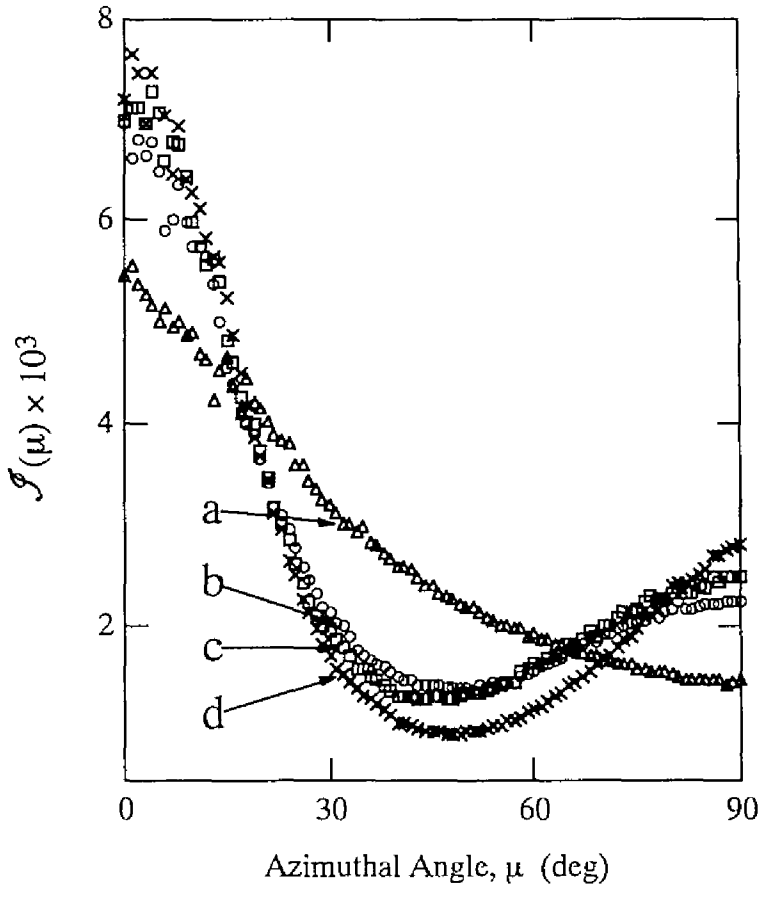

Figure 6-12. $\mathcal{F}(\mu)$ of the first-order maximum in the SAXS patterns shown in Figures 6-8, where curve a-d correspond to patterns (a)-(d) of Figure 6-8, respectively. $\mu = 0^\circ$ refers to the vertical direction in the patterns.

(a) to (d) in Figure 6-8, respectively. In shearing $\mathcal{F}(\mu)$ changes from curve a to b, indicating the change of the orientation of lamellar normals from a uniaxial to a biaxial orientation. The biaxiality increases slightly from curve b to c, which confirms our observation that the significant change in orientation occurs within the first 15 cycles of the shear. A steady state biaxial orientation is attained upon further increase of N. The biaxiality is much clearer in curve d than in curve c, due to the absence of the pattern oscillation smearing effect. Comparing patterns (d) and (e) in Figure 6-8, the biaxial orientation developed by the deformation is seen to gradually

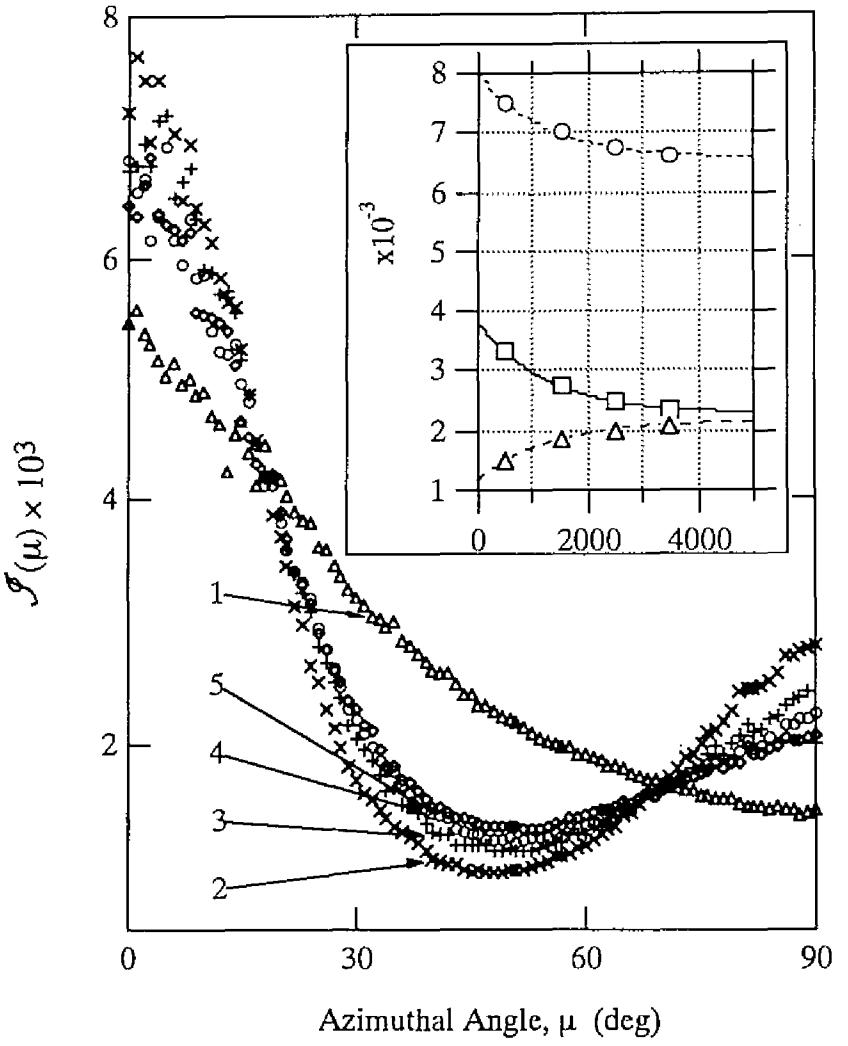

Figure 6-13. Change of $\mathcal{F}(\mu)$ of the first-order maximum with time during the relaxation of pattern (d) to (e) in Figure 6-8. Curves 1 and 2 in Figure 6-13, included as a reference, respectively correspond to curves a and d in Figure 6-12 (and hence to patterns (a) and (d) in Figure 6-8). Curve 5 corresponds to pattern (e) in Figure 6-8. $\mu = 0°$ refers to the vertical direction in the patterns. The inset of Figure 6-13 shows the changes of $\mathcal{F}(\mu)$ at $\mu = 0$, 45 and 90° with time where the solid and broken lines indicate a fitting of the exponential function.

relax toward a uniaxial orientation after cessation of shear, at $\gamma = 0$, though the biaxiality still remains clearly. An overall orientation of the lamellar normals is also seen to be relaxed. This relaxation behavior is more quantitatively presented in Figure 6-13.

Figure 6-13 shows the change of $\mathcal{J}(\mu)$ with time during the relaxation of pattern (d) to (e) in Figure 6-8. Curves 1 and 2 in Figure 6-13 which respectively correspond to curves a and d in Figure 6-12 (and hence patterns a and d in Figure 6-8) were included as a reference. Curve 5 corresponds to pattern (e). Thus the change of the pattern from (d) to (e) with time during the relaxation is shown in the evolution of $\mathcal{J}(\mu)$ from curve 2 to 5, indicating that the biaxiality decreases with time. The inset of Figure 6-13 shows the changes of $\mathcal{J}(\mu)$ at $\mu = 0$, 45 and 90° with time where the solid and broken lines indicate a fit of the exponential function $\mathcal{J}(\mu) = A[1+B\exp(-t/\tau)]$ with the relaxation time $\tau \cong 1.26\times10^3$ s, common for all the three curves and $|B|$ is of the order of 0.2 ~ 0.7. At the long time limit covered in this experiment, the values $\mathcal{J}(\mu)$ reach almost constant values which still show a slight biaxiality as evident from the fact that $\mathcal{J}(\mu)$ at $\mu = 90°$ is greater than $\mathcal{J}(\mu)$ at $\mu = 45°$.

The orientation relaxation similar to the case shown in Figure 6-8 is also seen in patterns (c) and (d) of Figures 6-10 obtained for the high-frequency and high-temperature deformation. Although the biaxiality is retained even at the longest time of our observation, the orientation distribution of the lamellar normals is clearly seen to become broader with time. Figure 6-14 shows $\mathcal{J}(\mu)$ where curves a-d respectively correspond to patterns (a)-(d) in Figure 6-10. The same trend as that observed earlier in Figures 6-12 and 6-13 is shown, except for the fact that the biaxiality developed (curve c in Figure 6-14) and the residual biaxiality attained a long time after relaxation of stress (curve d in Figure 6-14) are higher than the corresponding counterparts observed for low-frequency and low-temperature deformation (curves 2 and 5 in Figure 6-13).

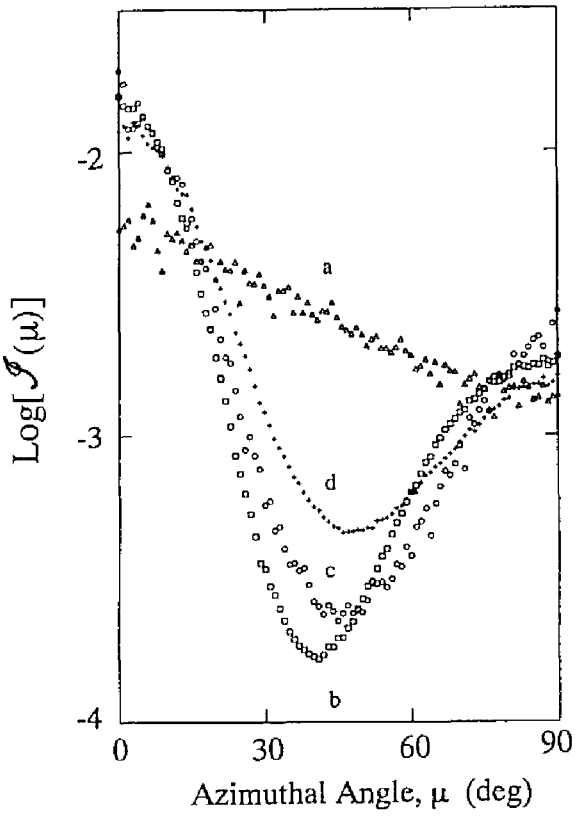

Figure 6-14. $\mathcal{I}(\mu)$ of the first-order maximum in the patterns shown in Figure 6-10, where curves a-d correspond to patterns (a)-(d), respectively. $\mu = 0°$ refers to the vertical direction in the patterns.

The uniaxial orientation obtained after the low-frequency and high-temperature shear deformation (pattern (b) in Figure 6-9) did not change at all after cessation of shear at $\gamma = 0$. The patterns taken 1000 s later in the relaxed state at 130 °C were identical to pattern (b) though they are not shown here. Moreover the orientation was observed to be unaltered even after this specimen was cooled to 105 °C, as shown in pattern (c). These observations are more quantitatively confirmed by the $\mathcal{I}(\mu)$ data shown in Figure 6-15 where curves a-c respectively correspond to patterns (a)-(c) in Figure 6-9. Although not shown here, all the patterns taken during the time interval up to 3000 s after cooling to 105 °C were the same as that in pattern (b)-(c) of Figure 6-9.

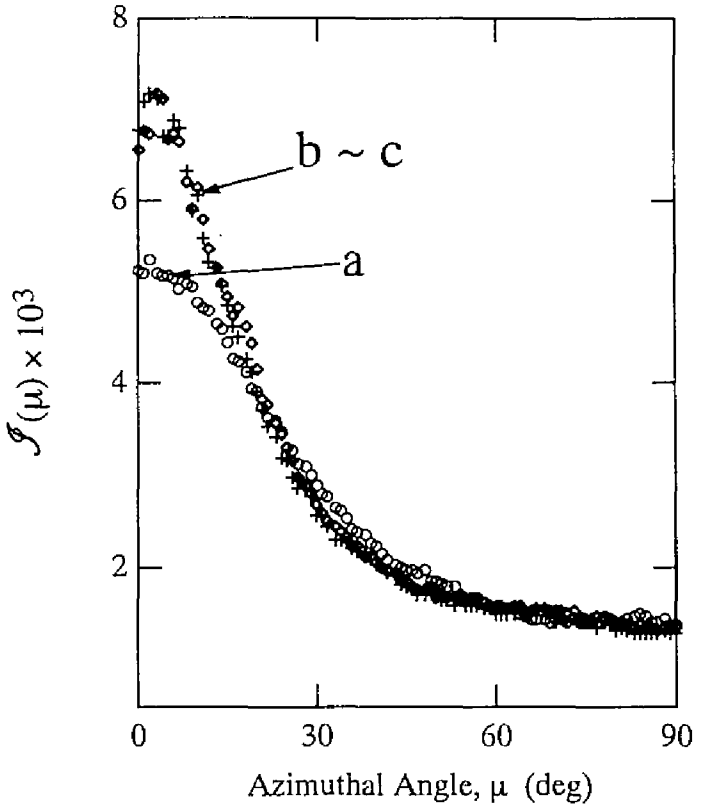

Figure 6-15. $\mathcal{I}(\mu)$ of the first-order maximum in the patterns shown in Figure 6-9, where curves a-c correspond to patterns (a)-(c), respectively. $\mu = 0°$ refers to the vertical direction in the patterns.

6-4. Discussion

It is clearly shown from Figures 6-10 and 6-14 that the shear deformation at high frequency and at high temperature (f = 1 Hz and T = 130 °C) develops a biaxial orientation. The development of the biaxial orientation is also clearly observed for the shear deformation at low frequency and at low temperature (f = 0.0149 Hz and T = 105 °C) from the μ-dependence of the SAXS patterns shown in Figure 6-8, and also from curve 2 in Figure 6-13.

The state of the biaxial orientation attained in the specimen subjected

to high-frequency (1 Hz) shear deformation at high temperature (130 °C) can be investigated from Figure 6-11. The edge pattern (a) clearly shows a bimodal intensity distribution with respect to an azimuthal angle, with maximum intensity along the OZ and OY axes; the intensity along the OZ axis is stronger than that along the OY axis. The former intensity is attributed to lamellae L_1 with their normals $\mathbf{l}_1$ preferentially oriented along the OZ axis, while the latter intensity is attributed to lamellae L_2 with their normals $\mathbf{l}_2$ preferentially oriented along the OY axis. The fraction of lamellae L_1 should be larger than that of lamellae L_2, judging from the data $\mathcal{J}(\mu)$ shown in Figure 6-14. The μ-dependence of the SAXS intensity reflects the distributions of $\mathbf{l}_1$ and $\mathbf{l}_2$ in the plane OYZ, i.e., some rotations of L_1 and L_2 around the OX axis.

The through pattern (b) shows a unimodal intensity distribution with respect to azimuthal angle, with a maximum intensity along the OY axis. This pattern arises also from lamellae L_2 and confirms the biaxial orientation. Its azimuthal breadth depends on an orientation distribution of $\mathbf{l}_2$ in the plane OXY, i.e., some rotations of L_2 around the OZ axis. The end pattern (c) also shows a unimodal intensity distribution with respect to azimuthal angle, with a maximum intensity along the OZ axis. This pattern arises from Lamellar L_1 but its azimuthal breadth reflects an orientation distribution of $\mathbf{l}_1$ in the plane OXZ, i.e., some rotations of L_2 around the OY axis. It may be noted that the intensity along the OY axis in pattern (a) is not the same as that in pattern (b) along the OY axis. We interpret this as follows. The intensity along the OY axis in pattern (a) depends on the rotation of the lamellae L_2 around the OZ axis, but the intensity along the OY axis in pattern (b) depends on the rotation of the lamellae L_2 around the OX axis. Thus the difference in the intensity in (a) and that in (b) may be possible if the specimens are

composed of many grains and if there is a difference in the degree of the two types of rotation.

In all the cases covered in this work, we cannot find the preferential orientation of the lamellae whose normal vectors are oriented along the OX axis (i.e., **preferential perpendicular orientation**), as reported earlier by Koppi et al.[12] and Winey et al.[13], although a minor fraction of lamellae has the perpendicular orientation as evident from Figure 6-11(b). Our observation on the lack of the preferential perpendicular orientation may be consistent with the previous results,[12,13] because our experiments were done far below T_{ODT} and the perpendicular orientation of the lamellae has been observed so far only when shear deformation is applied at T close to T_{ODT}.

SEP-34/32 is expected to have very high T_{ODT} which is estimated to be much higher than 400 °C. Hence the experimental temperatures of 105 °C and 130 °C are very much far below T_{ODT} and hence our sample is in a very strong segregation regime. The precursory SI diblock copolymer subjected to the selective hydrogenation of polyisoprene block had T_{ODT} in the melt much higher than 200 °C from SAXS measurements as a function of T. The SAXS measurements of T_{ODT} were done for dioctyl phthalate (DOP) solutions of the SI copolymer as a function of the copolymer concentration ϕ_P. The T_{ODT} values are extrapolated to the value at $\phi_P = 1$ in order to estimate its value in bulk. The T_{ODT} value for the bulk copolymer[30] was 370 ± 20 °C. It is known[31] that SEP has a Flory-Huggins' segmental interaction parameter much larger than that of SI. It is thus reasonable to assume T_{ODT} for SEP-34/32 is much higher than 370 °C. Thus our sample has $T/T_{ODT} < 403/643 = 0.63$ and is in an ordered state with a segregation stronger than the lamellae specimens[12,13] previously used. This fact seems to be important for understanding the biaxial orientation behavior. Although

the fraction of the lamellae L_2 as shown in Figure 6-11(e) is energetically unfavorable under the shear deformation, it may not be possible to be transformed into the parallel lamellae L_1 or into the perpendicular lamellae as reported by Koppi et al. by the processes such as destruction/re-formation[7,9,13] and grain rotation.[7] These processes may be much suppressed under the strong segregation regime. Because the perpendicular lamellae of the type reported by Koppi et al.[12] should be energetically more favorable than the lamellae L_2 under shear deformation, it is puzzling that we cannot attain the biaxial orientation with the preferential perpendicular lamellar orientation of the type reported by Koppi et al.

The state of orientation attained by the shear deformation seems to be intimately related to the stress level of our specimens. The biaxial orientation attained either by the low-frequency and low-temperature deformation or by the high-frequency and high-temperature deformation is associated with a higher stress than the uniaxial orientation attained by the low-frequency and high-temperature deformation. This situation may be roughly seen in the stress relaxation data shown in Figure 6-6. If we assume that the stress level encountered in an oscillatory deformation with a frequency f is roughly proportional to the relaxation modulus at $t = 1/f$. Then the two deformations giving rise to the biaxial orientation should have almost the same stress level, their moduli corresponding to point A and B in the figure, while the deformation yielding the uniaxial orientation should have a much lower stress than the above two deformations, with its modulus corresponding to point C.

One last comment I like to address is that on stability of the state of orientation attained by the shear deformation. In Section 6-3-4 it was clarified that the uniaxial orientation attained is quite stable after the cessation of

shear. It is also stable at temperatures lower than the temperature of the deformation. Thus the uniaxial orientation appears to be thermodynamically stable or metastable, at least, up to the temperature where the shear deformation is imposed. However, the biaxial orientation attained under the shear deformations employed in this work was shown to relax after cessation as shown in Figures 6-8 and 6-10, and 6-13 and 6-14. Figures 6-13 and 6-14 show quantitatively relaxation of the biaxial orientation toward a uniaxial orientation as well as overall orientation relaxation, although our data in the long time limit still show a biaxial orientation. Thus the biaxial orientation attained by the shear deformation is a thermodynamically unstable state. However it certainly exists as a steady state under the shear deformation accompanied by a high stress level, as evident by comparing patterns (b) and (c) in Figure 6-8 and curves b and c in Figure 6-12. However we cannot explain why the biaxial orientation exists in the steady state. This might be associated with the strong segregation phenomenon which suppresses the grain rotation and destruction/re-formation processes as discussed above.

6-5. Conclusion

Real-time and in-situ SAXS was performed with a SEP-34/32 diblock copolymer film specimen having alternating lamellar microdomains in a strong segregation regime far below the T_{ODT}. The 2D detector described in detail in Chapter 4 was used to measure 2D SAXS from the film specimen subjected to a large-amplitude oscillatory shear deformation. The shear deformation at high temperature and high frequency (f = 1 Hz and T = 130 °C) or at low temperature and low frequency (f = 0.0149 Hz and T = 105 °C) develops a biaxial

orientation, while the shear deformation at high temperature and low frequency (f = 0.0149 Hz and T = 130 ℃) improved a uniaxial orientation. The orientation attained by the shear deformation appears to be classified by the stress level of the specimen. The biaxial orientation attained either by the low-frequency and low-temperature deformation or by the high-frequency and high-temperature deformation is associated with a higher stress than the uniaxial orientation attained by the low-frequency and high-temperature deformation.

References

(1) See for example, Hashimoto, T. In *Thermoplastic Elastomers*; Legge, N. R.; Holden, G.; Schroeder, H. E., Ed.; Hanser Publishers, Munich Vienna New York, **1987**; p 349.

(2) See for example, Bates, F. S.; Fredrickson, G. H. *Ann. Rev. Phys. Chem.*, **1990**, *41*, 525.

(3) Keller, A.; Pedemonte, E.; Willmouth, F. M. Kolloid Z. Z. *Polym.* **1970**, *238*, 2329; *Nature* **1970**, *225*, 538.

(4) Hadziioannou, G.; Mathis, A.; Skoulios, A. *Colloid Polym. Sci.* **1979**, *257*, 136. Hadziioannou, G.; Picot, C; Skoulios, A.; Ionescu, M.-L.; Mathis, A.; Duplessix, R.; Gallot, Y.; Lingelser, J.-P. *Macromolecules* **1982**, *15*, 263.

(5) Fujimura, M.; Hashimoto, T.; Kawai, H. *Rubber Chem. Tech.*, **1978**, *51*, 215. Hashimoto, T.; Fujimura, M.; Saijo, K.; Kawai, H. *Adv. Chem. Series, Am. Chem. Soc.*, **1979**, *176*, 257.

(6) Pakula, T.; Saijo, K.; Kawai, H.; Hashimoto, T. *Macromolecules* **1985**, *18*, 1294. Pakula, T.; Saijo, K.; Hashimoto, T. *Macromolecules* **1985**, *18*, 2037.

(7) Morrison, F. A.; Winter, H. H. *Macromolecules* **1989**, *22*, 3533.

(8) Morrison, F. A.; Winter, H. H.; Gronski, W.; Barnes, J. D. *Macromolecules* **1990**, *23*, 4200.

(9) Scott, D. B.; Waddon, A. J.; Lin, Y. G.; Karasz, F. E.; Winter, H. H. *Macromolecules* **1992**, *25*, 4175.

(10) Morrison, F. A.; Mays, J. W.; Muthukmar, M.; Nakatani, A. I.; Han C. C. *Macromolecules* **1993**, *26*, 5271.

(11) Albalak, R. J.; Thomas, E. L. *J. Polym. Sci., part B, Polym. Phys.* **1993**, *31*, 37.

(12) Koppi, K. A.; Tirell, M.; Bates, F. S.; Almdal, K.; Colby, R. H. *J. Phys. II(Fr)* **1992**, *2*, 1941.

(13) Winey, K. I.; Patel, S. S.; Larson, R. G.; Watanabe, H. *Macromolecules* **1993**, *26*, 2542. Winey, K. I.; Patel, S. S.; Larson, R. G.; Watanabe, H. *Macromolecules* **1993**, *26*, 4373.

(14) Almdal, K.; Koppi, K. A.; Bates, F. S. *Macromolecules* **1993**, *26*, 4058

(15) Okamoto, S.; Saijo, K.; Hashimoto, T. *Macromolecules* **1994**, *27*, 3753.

(16) Koppi, K. A.; Tirrell, M.; Bates, F. S. *Phys. Rev. Lett.* **1993**, *70*, 1449.

(17) Balsara, N. P.; Hammouda, B. *Phys. Rev. Lett.* **1994**, *72*, 360.

(18) Harlan, J. T., Jr. U.S. Patent 3792005, 1974.

(19) Hashimoto, T.; Okamoto, S.; Saijo, K.; Kimishima, K.; Kume, T. *Acta Polymer.* **1995**, *46*, 463.

(20) Suehiro, S.; Saijo, K.; Ohta, Y.; Hashimoto, T.; Kawai, H. Analytica Chimica Acta 1986, 189, 41.

(21) Winter, H. H.; Scott, D. B.; Wolfram, G.; Okamoto, S.; Hashimoto, T. *Macromolecules* **1993**, *26*, 7236.

(22) Nishikawa, Y.; Kawada, H.; Hasegawa, H.; Hashimoto, T. *Acta Polymer.* **1993**, *4*, 192.

(23) Nitche, J. C. C. *Lectures on minimal surfaces, volume 1*; Cambridge University Press; Cambridge, **1989**.

(24) Thomas, E. L.; Alward, D. B.; Henkee, C. S.; Hoffman, D. *Nature* **1988**, *334*, 598.

(25) Hashimoto, T.; Nagatoshi, K.; Todo, A.; Hasegawa, H.; Kawai, H. *Macromolecules* **1974**, *7*, 364. Shibayama, M.; Hashimoto, T.; *Macromolecules* **1986**, *19*, 740.

(26) Bates, F. S.; *Macromolecules* **1984**, *17*, 2607. Rosedale, J. H.; Bates, F. S. *Macromolecules* **1990**, *23*, 2329. Bates, F. S.; Rosedale, J. H.; Fredrickson, G. H. *J. Chem. Phys.* **1990**, *92*, 6255.

(27) Kawasaki, K.; Onuki, A. *Phys. Rev.* **1990**, *A42*, 3664.

(28) Witten, T. A.; Leibler, L.; Pincus, P. A. *Macromolecules* **1990**, *23*, 824.

(29) Rubinstein, M.; Obukhov, S. P. *Macromolecules* **1993**, *26*, 1740.

(30) Mori, K.; Hashimoto, T., unpublished data.

(31) Owens, J. N.; Gancarz. I. S.; Koberstein, J. T.; Russell, T. P. *Macromolecules* **1989**, *22*, 3380.

Chapter 7

Small-Angle X-ray Scattering Studies of a Sphere-Forming Block Copolymer under Large Oscillatory Shear Deformation

7-1. Introduction

As the last of this series of studies on the behavior of block copolymers under the shear deformation, the dynamic rheo-optical experiment synchronous to mechanical stimulus was carried out with a 2D detector described in Chapter 4. I investigated in detail structural responses of spherical microdomains packed in a body-centered-cubic lattice in the very strong segregation regime *in situ* under the sinusoidal large-amplitude oscillatory shear deformation.

In the previous work,[1] a relationship between the ordered structure in the block copolymer solutions and their rheological behavior was explored by measuring separately small-angle X-ray scattering (SAXS) and rheology on the same solutions. The solutions studied were a polystyrene-*block*-polybutadiene (SB) in a solvent of n-tetradecane (C14), selectively good for polybutadiene block chains (PB) but very poor for polystyrene chains (PS). They formed the spheres composed of PS in the matrix of PB chains swollen with C14. The junction points between the two block chains are preferentially located at the interfaces between the spheres and matrix. The SAXS studies revealed that at low temperatures and/or high concentrations the spherical microdomains are packed in a cubic lattice with a long-range order. This ordered structure was found to give rise to a linear viscoelastic property with

shear modulus G, if shear stress σ is smaller than the yield stress σ_0 of the solutions, or a nonlinear, plastic flow, if $\sigma > \sigma_0$. Both σ_0 and G were found to be proportional to polymer concentration ϕ_p, which in turn was explained in terms of entropy elasticity of the confined chains, i.e., the elasticity of the swollen PB chains emanating from the vitrified PS spheres.

When the cubic lattice is deformed as shown in Figure 7-1(a),(b), the end-to-end vectors $\mathbf{r}_1$ and $\mathbf{r}_2$ of PB block chains are deformed to $\mathbf{r}_1'$ and $\mathbf{r}_2'$, respectively, to satisfy the demand of the uniform space filling by the corona chains (the block chains emanating from the spheres), as a consequence of low osmotic compressibility of the solution at high concentrations. The elastic deformation of the polymer coils leads to a decrease of the conformational entropy of the confined chains and hence an increase in elastic free energy.

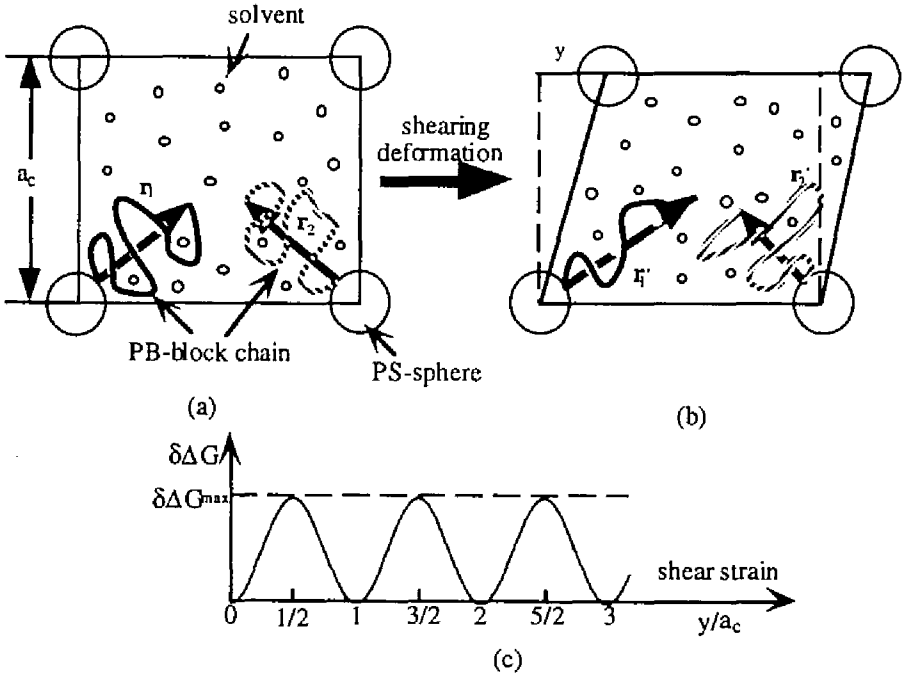

Figure 7-1. Schematic diagram showing elastic deformation of a cubic lattice formed by microphase-separated block copolymer solutions: (a) undeformed state, (b) deformed state with shear strain $\gamma = y/a_c$, a_c being the length of the cell, and (c) free energy change $\delta\Delta G$ as a function of the shear strain γ (based on ref 1).

In this way the excess free energy $\delta\Delta G$ is stored in the system as shown in Figure 7-1(c), which are responsible for σ_0 and G of the systems. The entropy elasticity of the confined chain was found to give also a nice correlation between the microstructural properties $\delta s/s_m$ and the rheological properties k_BT/GV_c and $k_BT/\sigma_0 V_c$, where $\delta s/s_m$ is the full width at half-maximum (fwhm) for the first-order SAXS peak relative to its peak position and V_c is the volume of the unit cell.[1]

In this work I extend the earlier work on the SI/C14 systems to polystyrene-*block*-poly(ethylene-*alt*-propylene) (SEP) in bulk which has a microdomain morphology of the spheres composed of PS packed in a bcc with a large paracrystal distortion of the second kind[2,3] in the matrix composed of poly(ethylene-*alt*-propylene) (PEP). I simultaneously observe *in situ* SAXS and stress for the specimen subjected to a large oscillatory shear strain in order to investigate a relationship between the deformation behavior of the bcc lattice systems and nonlinear mechanical properties.

Almdal et al.[4] reported very interesting results on the effects of large-amplitude oscillatory strain (100% strain with $\omega = 0.02$ rad/s) on the spheres packed in a bcc lattice in the PEP-PEE diblock copolymers. They studied the shear effect at temperatures 70-90 °C, relatively close to order-disorder transition temperature, $T_{ODT} = 105 \pm 5$ °C, in which both the matrix phase and the sphere phase are far above their glass transition temperatures. In contrast, I study here the shear effect at frequency $\omega = 0.0936$ rad/s and at temperature T = 25 °C; they were, respectively, higher and much lower than those used by Almdal et al. Our system is far below T_{ODT}, which is estimated[5] to be 180 ± 5 °C by SAXS, and PS spheres in our system are vitrified in the molten matrix of PEP. Thus I study the shear effects at very low temperature and high frequency, i.e., in a regime which is very different from that studied

by Almdal et al. The fact that our dispersed phase is vitrified may result in the shear effects which are different also from those predicted by simulations and theories.[6,7] It may give rise to some similarities between the behaviors of my system and those of colloidal crystals or of the micellar solution.[6] However the detailed discussions on the similarities and dissimilarities are beyond scope of this study. Here I report some initial results of our studies.

7-2. Experimental Section

7-2-1. Specimen

SEP (designated as SEP-10/34) which was prepared by hydrogenation of polystyrene-*block*-polyisoprene) (SI) copolymers was kindly supplied from Kuraray Co. Ltd., Japan. It has number-average molecular weight $M_n = 3.4 \times 10^4$, heterogeneity index $M_w/M_n = 1.3$ where M_w is weight-average molecular weight, and PS volume fraction in the copolymer 0.1. Polyisoprene block chain had a microstructure rich in 1,4-linkage (95 %) before hydrogenation. The as-received SEP-10/34 which is viscoelastic liquid at room temperature was annealed under vacuum at 60 °C for 1 week before the use for our experiment.

7-2-2. Rheo-optical Method

Simultaneous SAXS and stress measurements were performed by the dynamic SAXS apparatus presented in Chapter 4.[7,8] The hydraulic deformation apparatus used to impose the shear deformation was shown schematically in Figure 4-9(a).

The oscillatory shear strain was imposed on the specimen, sandwiched between two metal plates as shown in Figure 4-9(a). Incident X-ray beam

was irradiated normal to the plane OYZ in which the shear strain $\gamma = dy/dz$ exists. The OY axis is the direction parallel to the shear displacement. The SAXS intensity distribution was detected by IP placed normal to the incident beam.

In this work we imposed a large-amplitude sinusoidal shear strain with amplitude $\gamma_0 = 50$ % and static strain $\gamma_s = 0$ % and angular frequency $\omega = 0.0936$ rad/s at room 25 °C. The SAXS patterns were taken *in situ* during oscillatory deformation with the 2D detector. The following two modes were used: (i) the patterns were cumulated onto the detector over many cycles of oscillations between Nth cycle and (N+ΔN)th cycle, both N and ΔN being varied (designated hereafter the "**average mode**" for the sake of convenience), and (ii) the patterns were cumulated at particular strain phases over many cycles of oscillations, between Nth and (N+ΔN)th, in order to count a sufficient number of scattered X-ray photons for good statistical accuracy (designated hereafter the "**synchronous mode**"). Our IP detector has an octagon shape,[9] each face of which has IP having area of 100 mm x 200 mm The detector plane can be shifted from one face to another by rotating the octagon around its axis. In the synchronous mode, we assigned the four faces of the octagon to the four different phase intervals of the strain and changed these faces in synchronization with the strain phase.

The patterns were also taken as a function of time after cessation of the shear deformation. The change of linear dynamic mechanical response with N during the large-amplitude oscillatory deformation was investigated separately by an RMS605 mechanical spectrometer, Rheometrics CO. Ltd., Piscataway, NJ, under the same condition as those employed in our rheo-optical experiments. For this purpose a small strain amplitude of $\gamma_0 = 5\%$ and $\gamma_s = 0\%$ were used with parallel-plate geometry, and the part and

imaginary parts of dynamic shear moduli G' and G" were measured as a function of ω immediately after N cycles of the large-amplitude oscillations where N was also varied.

7-3. Results

7-3-1. Structure before Shear Deformation

Figure 7-2 shows the DSC thermogram of SEP-10/34 used in the experiment in a temperature range near the glass transition of the PS microdomains. The thermogram obtained at a heating rate of 20 °C/min shows a change of the base line between 22 and 62 °C, reflecting the glass transition temperature T_g of the PS microdomains. The T_g of PEP is about -60 °C, well below the experimental temperature, so that PEP alone behaves like a liquid. Thus the PS microdomains are glassy spheres immersed in a liquid medium at the experimental temperature.

Figure 7-3 shows the 2D-SAXS pattern taken with IP (part (a)) and the circular-averaged SAXS intensity distribution, I(q), for the annealed specimens of SEP-10/34 (part (b)) where q is the scattering vector defined by $q = (4\pi/\lambda)\sin(\theta/2)$, θ being the scattering angle. The 2D pattern shows no azimuthal angle dependence, and I(q) shows a sharp first-order maximum at $q_m = 0.0297$ Å^{-1} and a shoulder at the position of about $\sqrt{3}$ relative to the first

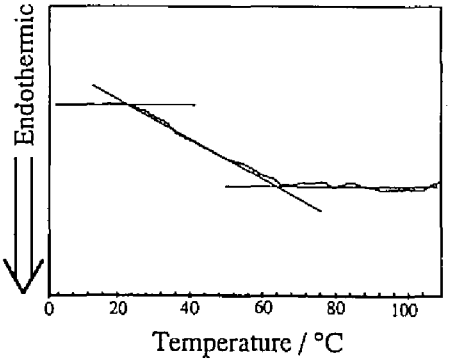

Figure 7-2. DSC thermogram obtained at a heating rate of 20 °C/min in a temperature range close to the glass transition temperature of the PS microdomains. The straight lines offer a visual guide for the thermogram.

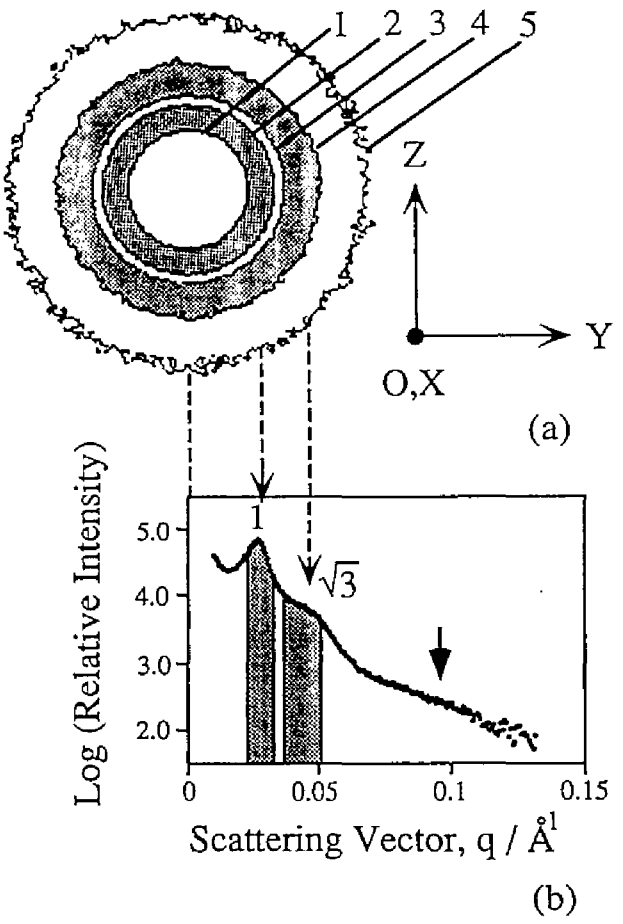

Figure 7-3. SAXS patterns taken by the 2D detector (a) and the circular-averaged intensity distribution with scattering vector q (b) for the undeformed SEP-10/34. The shaded zones in pattern (a) offer visual guides for the scattering maximum and shoulder. They also correspond to the intensity or q ranges shaded in part (b). The contour lines numbered 1-5 in pattern (a) have logarithm of scattered intensity of 4.60, 4.24, 3.88, 3.52, and 3.16, respectively.

order maximum and a very broad maximum at $q \cong 0.1$ Å^{-1}, defined hereafter as $q_{m,p}$. The detailed analysis of I(q) and transmission electron micrographs (TEM) yielded the following pieces of information:[10] (i) the spherical PS microdomains are dispersed in the matrix of PEP block chains, (ii) the first-order maximum and the higher order shoulder reflect the intersphere interference of the scattered waves, while the broad maximum at $q_{m,p}$ reflects the form factor of single spheres, and (iii) the number-average radius of the

spheres R is 70.6 ± 0.25 Å, the standard deviation of the radius σ_R is 15.1 ± 0.35 Å, and the characteristic interfacial thickness t_I = 13.3 ± 0.9 Å. The volume analysis yielded information that bcc is more favorable than the simple cubic lattice (sc) and the face-centered cubic lattice (fcc): the volume fraction of the PS spheres Φ_{PS} as calculated from the Bragg spacing $d = 2\pi/q_m = 212$ Å and R under the assumption of the bcc symmetry and that of a complete segregation of PS and PEP chains into the respective domains gives a best agreement with the volume fraction of the PS block chain in the copolymer ($f_{PS} = 0.1$). We obtained Φ_{PS} equal to 0.151 for sc, 0.107 for bcc, and 0.116 for fcc by using mass densities 1.06 and 0.86 g/cm^3 for PS and PEP, respectively. SAXS and TEM indicates that the lattice is considerably disordered and randomly oriented.

7-3-2. Mechanical Properties

Upon imposing the large-amplitude oscillatory strain, the force detected by our transducer decayed as a function of N, as schematically shown in Figure 7-4(a). The maximum stress for the N-th cycle of oscillation relative to that of the first cycle $\sigma(N)/\sigma(1)$ was plotted either semilogarithmically or doublelogarithmically in Figure 7-4(b). The stress decay appears to have at least two processes, i.e., the early and the late processes, which is believed to reflect a change of the microdomain structure of the system with N, as will be discussed later in section 7-4.

Figure 7-5 shows Lissajous figures for the large-amplitude oscillatory strain γ_0 = 50 % (a) and for a relatively small strain γ_0 = 17 % (b) at the same ω as described earlier. The data were obtained for the first cycle N = 1. The Lissajous figure in part (a) clearly shows nonlinear stress-response as shown by the humps at two strain phases (marked by arrows), but the nonlinearity

is less clear in part (b). We noted that the nonlinearity seen in part (a) does not necessarily vanish when the stress σ(N) decays with N.

Figure 7-6 shows the change of linear dynamic mechanical properties with N during the large-amplitude oscillatory deformation. The frequency dependence of the real part of the shear modulus G' and that of the imaginary part G'' are found nearly independent of N, and only their magnitudes decrease

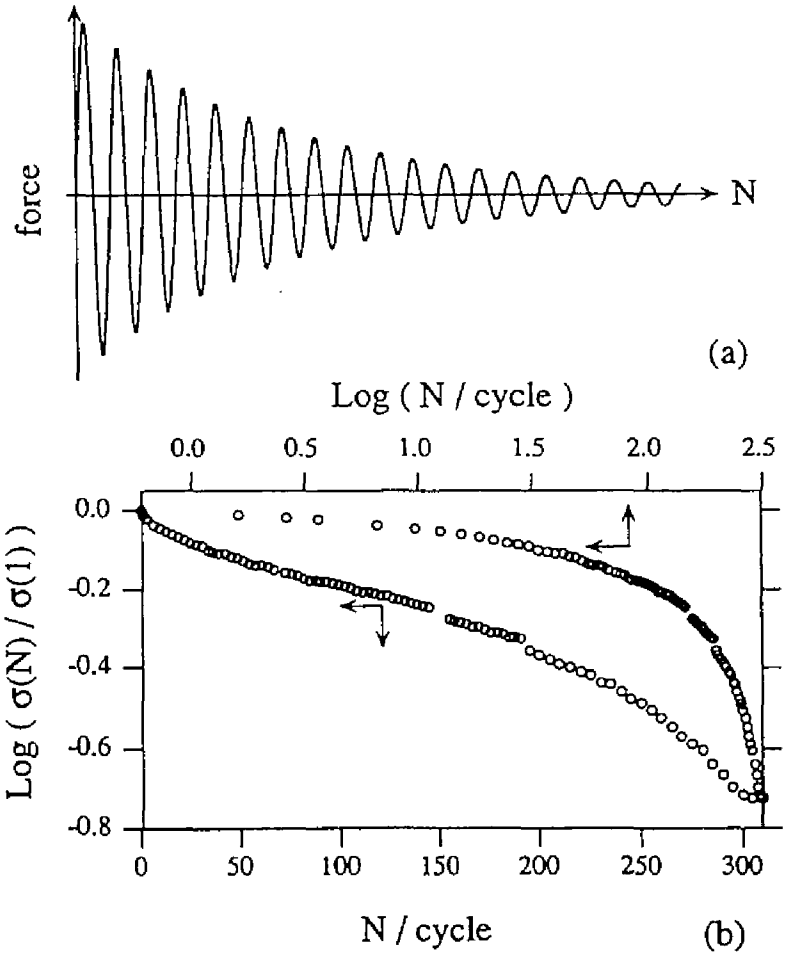

Figure 7-4. (a) Schematic diagram showing the variation of force under a large-amplitude oscillatory shear deformation, and (b) the decay of stress amplitude σ(N) with a number of deformation cycles N relative to the stress amplitude at the first cycle of the deformation σ(1).

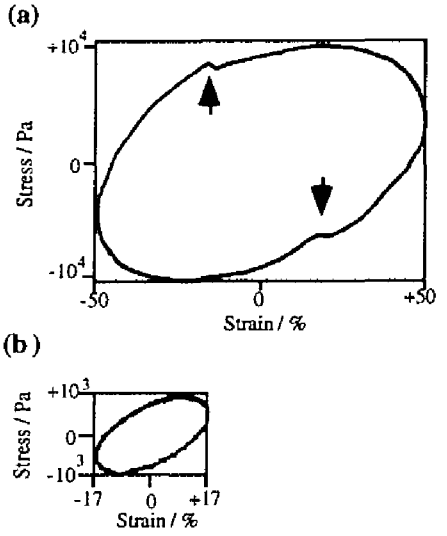

Figure 7-5. Typical Lissajous figures obtained for $\gamma_0 = 0.5$ (a) and $\gamma_0 = 0.17$ (b) in the first cycle of shear deformation at $\omega = 0.0936$ rad/s.

with N. The data for N = 0 stand for the data for the virgin sample. We also note the fact that at the low frequency of $\omega < 1$ the frequency dependence of G' is nearly identical to that of G", i.e.,

$$G',\ G'' \sim \omega^n \tag{7-1}$$

with $n \cong 0.6$. The low frequency scaling behavior given by eq 7-1 seems typical to that of the ordered microdomain systems of block copolymers. The value $n \cong 0.5$ was reported for the lamellar phase.[11,12] The fact that the prefactor of ω^n depends on N is parallel to the fact that $\sigma(N)$ decays with N.

7-3-3. SAXS Results Obtained with the Average Mode

Figure 7-7(a) shows the SAXS patterns taken *in situ* with IP during the large-amplitude oscillatory shear deformation. The pattern was taken with the average mode with N = 30 and $\Delta N = 150$. Comparing with the pattern in Figure 7-3(a), we found that the shear deformation tends to preferentially

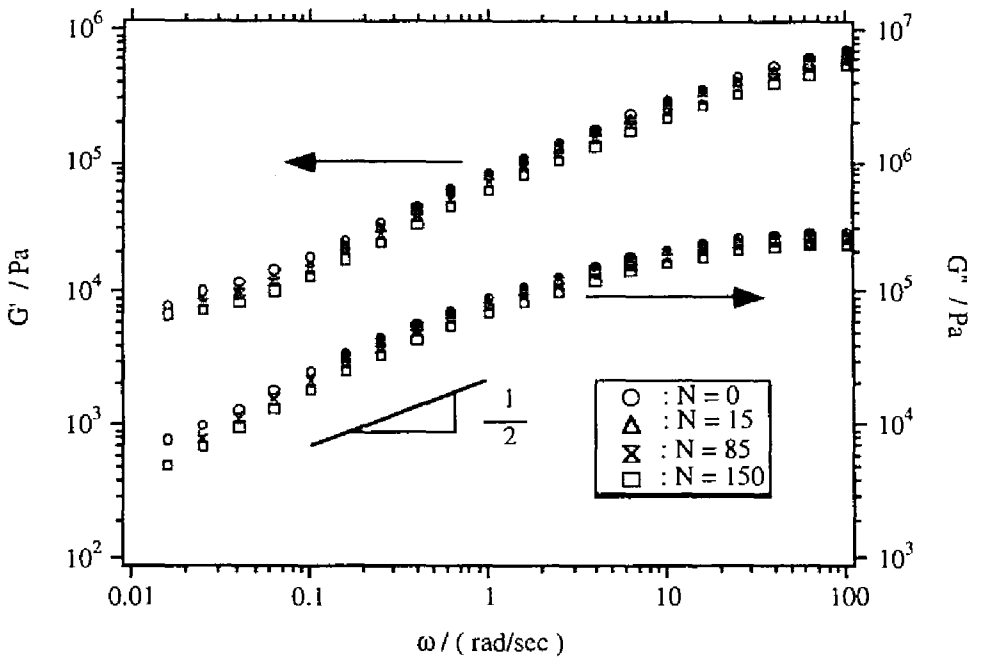

Figure 7-6. Linear dynamic mechanical properties obtained immediately after N cycles of the large-amplitude oscillatory shear deformation with varying N as shown in the figure. N = 0 corresponds to the results obtained with the virgin sample. G' and G" are real and imaginary parts of the shear moduli, respectively.

orient a particular lattice plane. The diffraction pattern at the first-order maximum position defined hereafter as $q_{m,l}$ is clearly directionally dependent: a sharp meridional two-point pattern along the OZ axis and long equatorial arcs along the OY axis.

On the other hand, the SAXS intensity in the vicinity of $q_{m,p}$ is directionally independent, implying that the vitrified PS spheres are not deformed under the shear deformation. Thus the bcc lattice is oriented and deformed, but the spheres remains undeformed under the shear deformation. Figure 7-7(b) presents a model showing preferred (110) plane orientation parallel to the OXY plane to explain the two-point pattern observed under the oscillatory shear deformation. The details will be discussed later in Section 7-4. Our preliminary results indicated that the meridional two-point pattern

shown in part (a) becomes increasingly sharp with N, although not shown here.

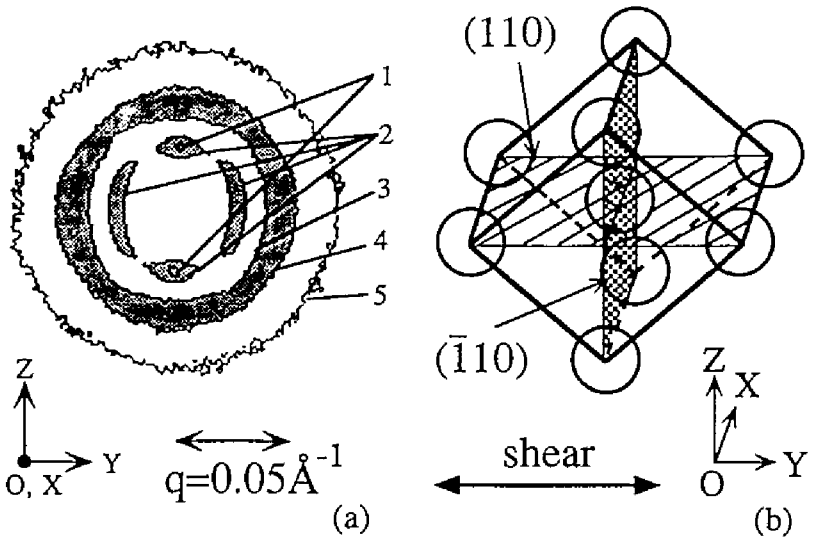

Figure 7-7. (a) SAXS pattern cumulated over the strain cycles defined by N = 30 and ΔN = 150 (the average mode) during the large-amplitude oscillatory shear deformation and (b) the model showing a preferential orientation of the (110) lattice plane parallel to OXY plane. The shaded zones in the pattern (a) offer visual guides for the scattering maximum and shoulder. The contour lines numbered 1-5 in pattern (a) have logarithm of scattered intensity of 4.66, 4.31, 3.64, 3.28, and 2.60, respectively.

7-3-4. SAXS Results Obtained with the Synchronous Mode

In order to gain a deeper insight into the lattice deformation and orientation under the shear deformation, the SAXS pattern was taken *in situ* with the *synchronous mode* and with N = 80 and ΔN = 70. The patterns in Figure 7-8(a) were taken at four representative strain phases centered at 0, $\pi/2$, π and $3\pi/2$ (designated phase 1 to 4, respectively) and over the phase interval $2\Delta = 0.388\ \pi$, as shown in parts (b) and (c). The response of the pattern at $q_{m,1}$ position is particularly interesting: each pattern in part (a) is composed of four points. The two points along the OZ axis are almost stationary, staying parallel to the OZ axis for all the strain phases, but the other two points are oscillating, i.e., they are approximately at 65°, 90°, 115°,

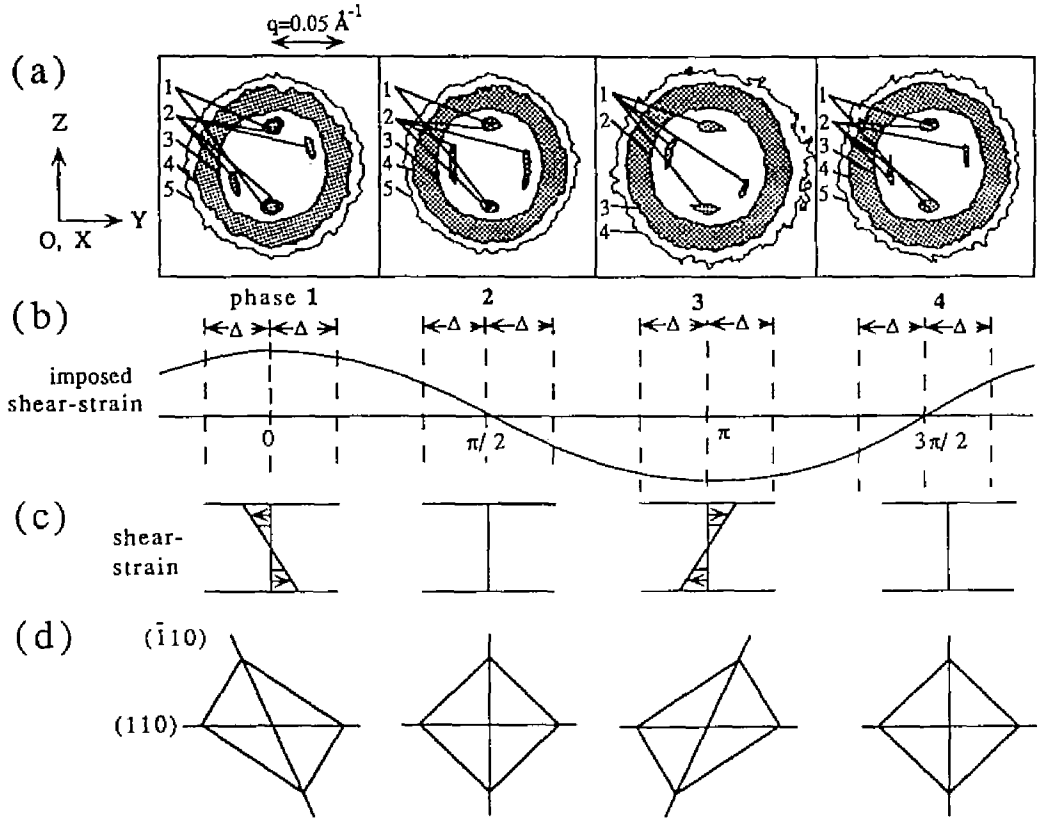

Figure 7-8. SAXS pattern (a) obtained at four representative strain phases as shown in (b) and (c) (the synchronous mode), and the model to explain the four diffraction spots arising from (110) and ($\bar{1}$10) lattice planes (d). The pattern at each phase was obtained for the strain phase of $[-\Delta + \phi_i, \Delta + \phi_i]$ where $\phi_i = 0, \pi/2, \pi$, and $3\pi/2$ for phase 1-4, respectively and $\Delta = 0.194\ \pi$. The pattern at each phase was obtained by cumulating the SAXS intensity over the strain cycles defined by N = 80 and ΔN = 70. The shaded zones in pattern (a) offer visual guides for the scattering maximum and shoulder. The contour lines numbered 1-5 have respectively logarithm of scattering intensity of 3.60, 3.40, 2.80, 2.40, and 2.20 for the patterns in phases 1 and 2, 3.45, 2.77, 2.32, and 2.10 for those in phase 3, and 3.65, 3.42, 2.74, 2.28, and 2.05 for those in phase 4.

and 90° with respect to the OZ axis in phases 1-4, respectively. Part (d) indicates a qualitative, simplified model to explain the above observation, the details of which will be discussed in Section 7-4.

7-4. Discussion

7-4-1. Response of the bcc Lattice

The results obtained in Figure 7-8(a) clarify the pattern obtained in Figure 7-7(a). The meridional two-point pattern along the OZ axis should arise from the (110) plane oriented more or less stationarily parallel to the plane OXY, as shown in Figures 7-7(b) and 7-8(d), while the other two-point pattern (equatorial two-point pattern) changes its orientation, oscillating in the OYZ plane about the equator with a change of the strain phase, as shown in Figure 7-8(a). Hence in the average mode, the oscillating equatorial two-point pattern should appear to be a long arc, while the stationary meridional two-point pattern should remain two-point like, as shown in Figure 7-7(a). The oscillating equatorial two-point patterns in Figure 7-8(a) or the long equatorial arc in Figure 7-7(a) should arise from the $(\bar{1}10)$ plane orthogonal to the (110) plane. The oscillating equatorial pattern indicates a dynamic lattice deformation as shown schematically in Figure 7-8(d).

Thus the results obtained in Figures 7-7 and 7-9 immediately give us the following two conclusions. (1) Under the oscillatory shear deformation, (110) plane having the highest number density of the spheres orient parallel to the OXY plane. A similar orientation of the (110) plane parallel to the OXY plane was also reported after cessation of a large-amplitude oscillatory shear strain.[2] we found that the degree of orientation of the (110) plane increases with N. The preliminary SAXS results with the average mode

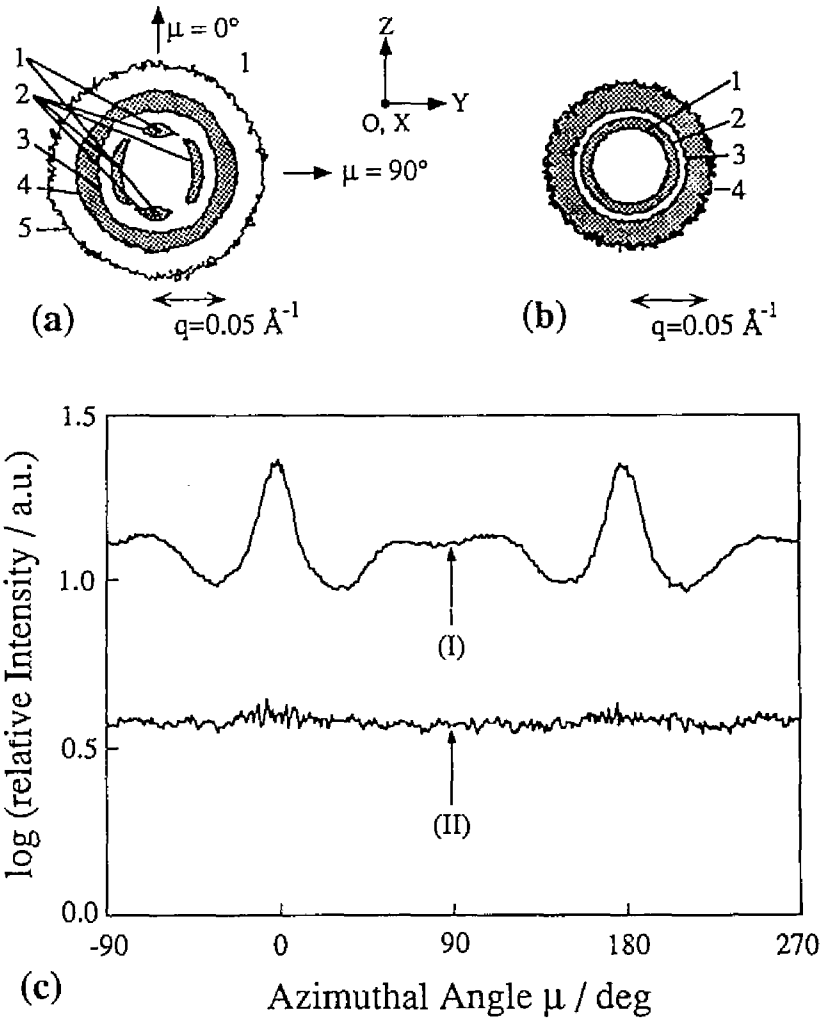

Figure 7-9. Change of the SAXS pattern with time after cessation of the large-amplitude oscillatory shear deformation. Pattern (a) was obtained during oscillatory shear deformation with the average mode with N = 30 and ΔN = 150. After this experiment, the shear deformation was stopped at zero strain. Then pattern (b) was taken from 0 to 1000 s after cessation of the shear deformation. The azimuthal-angular dependences for the first-order diffraction maximum in patterns (a) and (b) are shown by curve (I) and (II), respectively, in part (c). The shaded zones of patterns (a) and (b) offer visual guides for the scattering maximum and shoulder. The contour lines numbered 1-5 for pattern (a) have respectively logarithm of scattered intensity of 4.66, 4.31, 3.64, 3.28, and 2.60, while those numbered 1-4 for pattern (b) have respectively 2.81, 2.61, 2.27, and 2.03.

indicate that a rapid increase in the degree of orientation is achieved for the first 30 cycles and a further increase of orientation occurs gradually with a further increase of N. (2) In response to the applied shear deformation, the bcc lattice undergoes dynamic lattice deformation under the constraint that the (1 1 0) planes orient, by and large, parallel to the OXY plane. The position of the meridional two-point pattern with respect to θ or q remains almost unchanged with the strain phase, indicating that the (1 1 0) spacing is essentially kept constant during the deformation. However the position of the $(\bar{1}10)$ diffraction peak changes with the strain phase: the positions of the diagonal two-point pattern in phases 1 and 3 locate at higher q than those of the equatorial two-point pattern in phases 2 and 4. The latter positions locate at smaller q than those of the meridional two-point pattern. The change of $(\bar{1}10)$ diffraction spots with the strain phase implies the $(\bar{1}10)$ spacing is stretched under the shear deformation in phases 2 and 4 and it tends to be compressed in phase 1 and 3. we roughly estimated the strain amplitude imposed on the crystal γ_{cryst} from the changes of (1 1 0) and $(\bar{1}10)$with the strain to be $\gamma_{cryst} \equiv \tan 25° = 0.47$, close to γ_0, where the angle 25° is that between the equator and the line connecting the centers of the diagonal two-point patterns in phases 1 and 3.

Close observations of the results in Figure 7-8(a) lead us to the following additional conclusions. (3) If the crystal deformation as indicated in Figure 7-8(d) occurs in phase with the applied strain phase, the SAXS patterns obtained in phases 2 and 4 should be identical and those obtained in phase 1 and 3 should be in mirror-image with respect to the OZ axis. However, the patterns in phase 2 and 4 are not clearly identical, indicating that a phase difference exists between the applied strain and the strain on the crystal. (4) The width of the meridional two-point pattern along the azimuthal-angular

direction appears to depend on the strain phase. This implies a dynamic variation of the crystal orientation as a whole under the oscillatory deformation. (5) Our preliminary SAXS results with the synchronous mode with a small fixed ΔN but varying N appear to indicate that the lattice strain γ_{cryst} gradually decreases with N in the region of $N > 40$.

7-4-2. Origin of Stress Decay

The conclusions 1-5 obtained in Section 7-4-1 should be somehow related to the rheological behavior of the systems under the large amplitude of oscillatory shear strain (Figure 7-4) as well as under the small strain (Figure 7-6). The rheological behavior should be affected by all the factors given above; the orientation of the (110) plane (conclusion 1), the dynamic deformation of the bcc lattice (conclusion 2), its loss tangent (conclusion 3) and their changes with N (conclusion 5), and the dynamic orientation of crystal as a whole (conclusion 4).

The decay of the stress amplitude $\sigma(N)$ with N appears to be apparently composed of the early and the late processes which dominate at $N \ll 30$ and $N \gg 30$, respectively. The rapid orientation of the (110) plane parallel to the OXY plane (conclusion 1) is apparently related to the decay process in the early stage, while the gradual decrease of the lattice deformation γ_{cryst} with N (conclusion 5) is related to the decay process in the late stage. The phase difference of the lattice deformation and orientation against the strain (conclusion 3) may be related to the large loss tangent observed in the Lissajous figures in Figure 7-5.

The decrease of the dynamic lattice strain γ_{cryst} with N may occur as a consequence of increased volume fraction of the grain-boundary region where

the cubic packing of the spheres may be more disordered than that inside the grain. This effect may account also the decrease of G' and G" with N in Figure 7-6.

7-4-3. Relaxation after Cessation of Oscillatory Shear

The orientation of the (110) plane developed under the large-amplitude oscillatory shear deformation was found to relax into random orientation after cessation of the shear, as shown in Figure 7-9 where the pattern in part (a) was obtained with the average mode and with N = 30 and $\Delta N = 150$. The pattern in part (b) was taken from 0 to 1000 s after the cessation of the shear deformation. The patterns a and b have the azimuthal-angular dependence of the first-order diffraction intensity as shown in curves I and II in part (c), respectively. This clearly indicates the orientational memory built up by the shear deformation completely decays after the cessation. This fact is a big surprise to me, puzzling but yet intriguing. It is also a big contrast to the results reported by Almdal et al.[2] They reported a high orientation of the bcc lattice even after cessation of the shear at zero strain. Interestingly the decay of the orientation memory causes the recovery of stress after the cessation of the shear as is demonstrated in Figure 7-10.

The virgin sample shows the stress decay with N during the large-amplitude oscillatory deformation as shown in the curve labeled 1 in Figure 7-10. After oscillation up to N = 300, the stress decayed to point A. In this figure $\sigma(1)$ always refers to the stress at N = 1 for the virgin sample. The specimen subjected to the oscillation up to $N \cong 300$ was released from the strain and left relaxed for 4.5 h at room temperature. The stress at point A was relaxed to zero (point B) after the release of the strain to zero. After the rest for 4.5 h at room temperature, the large-amplitude shear deformation

was applied to the specimen, and the stress decay was measured again as a function of N. The result is shown by the curve labeled 2. We found the stress recovery to point C at the second-run deformation, which may be due to a structure recovery during the rest. The stress decay due to the oscillation (point C to point D) is found to be much faster in the second run than in the first run. The same specimen was released from the strain at point D, and the stress relaxation occurred to point E. The specimen was left at room temperature for 2 to 3 min and then subjected to the third-run oscillatory deformation. The stress decay is shown by the curve labeled 3. It is clearly seen that the amount of stress recovery depends on the time spent for the stress relaxation. Almost no stress recovery is attained during the relaxation between the second and the third runs; i.e., the stress level of point D is almost the same as that of point F. The initial stress decay with N appears to increase in the order of the first run, the second run and the third

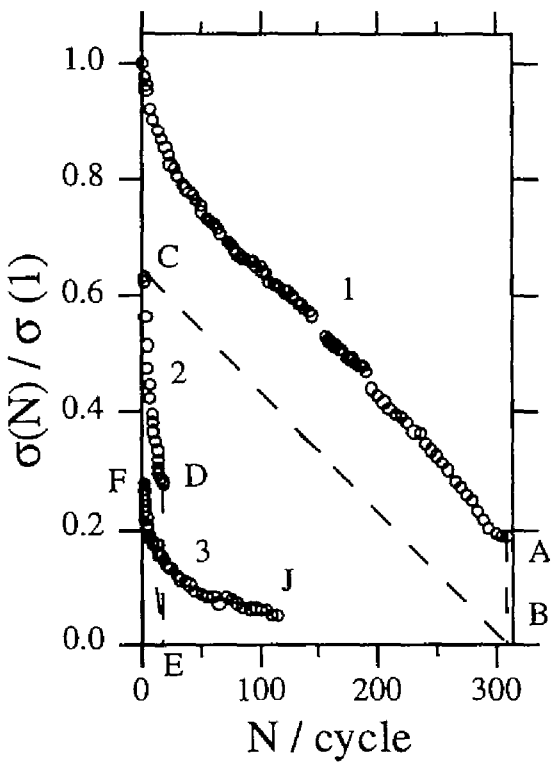

Figure 7-10. Stress recovery after cessation of the large-amplitude oscillatory shear strain. The decay of the stress amplitude $\sigma(N)/\sigma(1)$ with N under the deformation was plotted for the virgin sample (curve 1), for the sample subjected to the first-run deformation to point A and then relaxed to zero strain for 4.5 h (curve 2) and for the sample subjected to the second-run deformation to point D and then relaxed to zero strain for a few minutes (curve 3). $\sigma(1)$ always refers to the maximum stress at the first cycle of deformation for the virgin sample.

run. However the stress decay rate appears to be slowed down as the stress level decreases, which is obvious in curve 3.

The recovery of the stress may be attributed to a recovery of the cubic structure in the grain-boundary region in which the bcc crystallike structure may be transformed into the spheres packed in the disordered lattice under the large-amplitude oscillatory strain. The recovery of the lattice structure in the grain boundary may induce disorientation and reorganization of the shear-aligned lattice structure in the strong segregation limit, resulting in the relaxation of the structure and stress recovery after cessation of the shear deformation.

7-5. Conclusion

In this work I presented a structural response of the spherical microdomains of block copolymers to a large-amplitude oscillatory shear deformation in the regime of low-temperature and strong-segregation limit. The regime explored is quite different from the high-temperature and weak-segregation regime covered by previous work, e.g., Almdal et al.[2] The information obtained covers not only the structure attained after cessation but also *real-time*, *in-situ* response of the domains which has not been reported previously. The high-temperature and weak-segregation system contains the soft spheres in the soft matrix near the order-disorder transition (ODT), while the low-temperature and strong segregation system contains the vitrified hard spheres in the soft matrix far below ODT. Thus, the former system should be subjected to structure reorganization under shear more easily and extensively than the latter system. I hope that our information obtained with the low-temperature behavior is also important to the enrichment of our

understanding of the rheo-optical behavior of block copolymers. A more detailed analysis and theoretical interpretation of our results deserve future work.

References

(1) Hashimoto, T.; Shibayama, M.; Kawai, H.; Watanabe, H.; Kotaka, T. *Macromolecules*, **1983**, *16*, 361.

(2) Almdal, K.; Koppi, K. A.; Bates, F. S. *Macromolecules*, **1993**, *26*, 4058 and the references cited therein.

(3) Kawamura, T., Hashimoto, T. unpublished data.

(4) Ohta, T.; Enomoto, Y.; Harden, J. L.; Doi, M. *Macromolecules*, **1993**, *26*, 4928.

(5) Doi, M., Harden, J. L.; Ohta, T. *Macromolecules*, **1993**, *26*, 4935.

(6) Phoon, C. L.; Higgins, J. S.; Allegra, G.; van Leeuwen, P.; Staples, E. *Proc. R. Soc. Lond. A* , **1993**, *442*, 221.

(7) Hashimoto, T.; Suehiro, S.; Shibayama, M.; Saijo K.; Kawai, H. *Polym. J.*, **1981**, *13*, 501. Hashimoto, T.; Saijo, K.; Kość, M.; Kawai, H.; Wasiak, A.; Ziabicki, A. *Macromolecules*, **1985**, *18*, 472.

(8) Suehiro, S.; Saijo, K.; Ohta, Y.; Hashimoto, T.; Kawai, H. *Analytica Chimica Acta*, **1986**, *189*, 41.

(9) Hashimoto, T.; Kume, T.; Saijo, K.; Kimishima, K.; Okamoto, S. in preparation.

(10) Hashimoto, T.; Kawamura, T.; Harada, M.; Tanaka, H. *Macromolecules*, **1994**, *27*, 3063

(11) Bates, F. S. *Macromolecules*, **1984**, *17*, 2607, Rosedale, J. H.; Bates, F. S. *Macromolecules*, **1990**, *23*, 2329, Koppi, K. A.,; Tirrel, M.; Bates, F. S.; Almdal, K.; Colby, R. H. *J. Phys. II (Fr.)* **1992**, *2*, 1941.

(12) Kawasaki, K.; Onuki, A. *Phys. Rev.* **1990**, *A42*, 3664.

Summary

Part I.

In Part I, detailed studies on static structures and their formation were carried out. The following results were obtained.

Chapter 1.

The structure evolution in a polystyrene-*block*-polyisoprene-*block*-polystyrene triblock copolymer (SIS) on the phase transition (or order-disorder transition, ODT) was investigated by rheology and small-angle X-ray scattering (SAXS). The copolymer has an equilibrium morphology of cylindrical polystyrene microdomains hexagonally packed in polyisoprene matrix. The order-to-disorder transition temperatures determined by rheological and SAXS techniques in the heating cycle were in good agreement with each other while the ordering phenomena observed upon cooling depended on the observation techniques. Since SAXS measurements provide the structural information of a 10-nm scale, the formation of the cylindrical microdomains was detected by SAXS. On the other hand, low-frequency dynamic mechanical measurements are mainly affected by the 1-μm-scale grain morphology. The results imply that the microphase separation occurs rapidly upon cooling below the ODT temperature whereas the growth of the grain structures needs longer time.

Chapter 2.

A lamellar microdomain structure formed in the solvent-cast films of a polystyrene-*block*-poly(ethylene-*alt*-propylene) diblock copolymer (SEP) was studied in detail by SAXS. The SAXS profiles displayed a series of peculiar

scattering maxima which cannot be ascribed to the higher-order diffraction maxima from the one-dimensional lattice of the regular lamellar structure. A one-dimensional paracrystal model with a preferential orientation was employed to analyze the SAXS profiles. The results suggest that these maxima are attributed to the higher-order scattering maxima of the particle scattering factor from single lamellar microdomains. The maxima suggest that the relative standard deviation for the distribution of the polystyrene lamellar size is much smaller than that of the lamellar spacing, giving rise to a situation in which the oscillation of the particle factor with scattering vector **h** persists up to high h (magnitude of **h**) values while that of the lattice factor damps to unity at low h values. The SAXS result was interpreted as being due to a bending distortion of the polystyrene lamella with a smaller thickness and a narrower thickness distribution than those of the poly(ethylene-*alt*-propylene) lamella. A study by transmission electron microscopy supported this result.

Chapter 3.

New class of molecular constraint was investigated to find new morphology and new properties. The microdomain structure of the model three-component, three-arm star-shaped copolymers consisting of polystyrene (PS), poly(dimethylsiloxane) (PDMS) and poly(*tert*-butyl methacrylate) (PTBMA), each of them having nearly the same weight fraction, were investigated by means of differential scanning calorimetry (DSC), transmission electron microscopy (TEM) and SAXS. The DSC results exhibiting the glass transition of PS and PTBMA and the crystallization and melting of PDMS strongly suggest the microphase separation of the three components into three microdomains. The microdomain structure is considered to be extremely complicated because the

chemical junction points of the three constituent polymers must be confined on the lines where three kinds of interfaces meet. TEM and SAXS results strongly support the existence of the very regular microdomain structure with three-fold symmetry. Each of the three components possibly forms a three-dimensionally continuous network domains resulting in an ordered tricontinuous microdomain structure.

Part II.

I presented the works on the observation of rearrangement of domain structures of block copolymers under large-amplitude oscillatory shear deformation as well as the structures before the deformation.

Chapter 4.

A new data acquisition system for time-resolved SAXS and wide-angle X-ray diffraction (WAXD) studies, especially designed for a use with a rotating anode X-ray generator as an X-ray beam source, was developed. A drum with eight imaging plates (IP) containing phosphor crystals photostimulable for X-ray beam was used as the two-dimensional (2D) detector. A time-resolved and continuous data acquisition of SAXS and WAXD patterns on the 2D detector was enabled either by changing the IP by a rotation of the drum or by shifting the exposed region of one IP with respect to the incident beam. This system was adopted to the *in situ* measurements of the time-evolution of SAXS patterns during the isothermal orientation crystallization of a crosslinked *cis*-1,4-polybutadiene rubber. It was observed that the long period decreased with time during the crystallization as a results of increasing the number of lamellar crystallites, and that the lamellar crystallites were regularly stacked with their

lamellar normals oriented parallel to the stretching direction.

Chapter 5.

As a consequence of the findings in Chapter 1, the slow part of the structuring process in the SIS triblock copolymer gave sufficient time for flow alignment of microphase-separated domains with the hexagonally-packed cylindrical morphology during their growth phase. The resulted morphology was observed by the 2D detector system for SAXS described in Chapter 4. Near "single crystal" morphology was obtained through large-amplitude oscillatory shear at about 25 K below ODT. The direction of the cylindrical axes was uniform, i.e., formation of grain boundaries was avoided. The low-frequency linear viscoelastic properties of the single crystal structure were found to be affected by the domain alignment in the flow direction. The quench depth ΔT was found to be an important parameter: at a small quench depth of $\Delta T \cong 10$ K, microphase separation was found to be suppressed by the oscillatory shear.

Chapter 6.

Real-time and *in situ* SAXS studies were conducted on an SEP diblock copolymer film having alternating lamellar microdomains. SAXS was measured with the 2D detector (shown in Chapter 4) for the film specimens subjected to a large-amplitude oscillatory shear deformation with a sawtooth type strain γ ($-0.5 \leq \gamma \leq 0.5$) at frequency f = 0.0149 or 1 Hz and at temperature T = 105 or 130 °C. The specimens initially had a uniaxial orientation with the lamellar normal **l** preferentially oriented parallel to the film normal (OZ-axis). The shear deformation at low temperature and low frequency (f = 0.0149 Hz, T = 105 °C), or that at high temperature and high frequency (f = 1 Hz, T = 130 °C), with the

displacement vector parallel to the OY axis and the shear gradient axis parallel to the OZ axis, gave a biaxial orientation with **l** preferentially oriented either along the OZ or OY axis, the former being dominant to the latter. On the other hand, the shear deformation at high temperature and low frequency (f = 0.0149 Hz, T = 130 °C) gave an improved uniaxial orientation of **l** with respect to the OZ axis. A preferred orientation of **l** along the OX axis, the neutral axis, was not detected in any case. The two deformations which gave the biaxial orientation involved about the same shear stress level, but this stress level was much higher than that involved by the deformation giving rise to the improved uniaxial orientation.

Chapter 7.

Rheo-optical studies were conducted on an SEP diblock copolymer having spherical microdomains composed of polystyrene block chains (PS) in the matrix composed of poly(ethylene-*alt*-propylene) block chains. SAXS was detected with the 2D detector described in Chapter 4 simultaneously with stress measurements on the specimens subjected to a large-amplitude oscillatory shear deformation with strain amplitude of 50% and zero static strain at frequency of 0.0936 rad/s and at room temperature, with the purpose to elucidate a relationship between a macroscopic property of the systems and their mesoscopic structure as revealed by SAXS. The results indicated that the spheres are packed in a body-centered-cubic (bcc) lattice and that the shear deformation induces a preferential orientation of (110) lattice planes parallel to shear plane and elastic deformation of the bcc lattice under this particular (110) lattice plane orientation. The stress amplitude $\sigma(N)$ is found to decay with N, the number of strain cycle, and the stress decay to be recovered after cessation of shear. The stress decay with N and the stress

recovery after the cessation appear to be interrelated to the preferential orientation (110) plane with N and its orientation relaxation after the cessation, respectively. The change of the elastic strain amplitude on the lattice with N and with time after cessation of shear was also proposed to be responsible for the stress decay and stress recovery.

List of Publications

Chapter 1

1. "Ordering by Flow near the Disorder-Order Transition of a Triblock Copolymer Styrene-Isoprene-Styrene" Winter, H.H.; Scott, D.B.; Gronski, W.; Okamoto, S.; Hashimoto T. *Macromolecules*, **1993**, *26*, 7236.

Chapter 2

2. "Small-Angle X-ray Scattering Study of Lamellar Microdomains of Block Copolymer" Sakurai, S.; Okamoto, S.; Kawamura, T.; Hashimoto, T. *J. Appl. Crystallogr.*, **1991**, *24*, 679.

Chapter 3

3. "Morphology of Model Three-Component Three-Arm Star-Shaped Copolymers" Okamoto, S.; Hasegawa, H.; Hashimoto, T.; Fujimoto, T.; Zhang, H.; Kazama, T.; Takano, A; Isono, Y. *Polymer*, **1997**, *in press*.

Chapter 4

4. "Time-resolved small-angle and wide-angle X-ray scattering apparatus using the imaging plate as a two-dimensional detector" Hashimoto, T.; Okamoto, S.; Saijo, K.; Kimishima K.; Kume, T *Acta. Polymer.*, **1995**, *46*, 463.

Chapter 5

1. "Ordering by Flow near the Disorder-Order Transition of a Triblock Copolymer Styrene-Isoprene-Styrene" Winter, H.H.; Scott, D.B.; Gronski, W.; Okamoto, S.; Hashimoto T. *Macromolecules*, **1993**, *26*, 7236.

Chapter 6

5. "Real-Time SAXS Observations of Lamella-Forming Block Copolymers under Large Oscillatory Shear Deformation" Okamoto, S.; Saijo, K.; Hashimoto T. *Macromolecules*, **1994**, *27*, 5547.

Chapter 7

6. "Dynamic SAXS Studies of Sphere-Forming Block Copolymers under Large Oscillatory Shear Deformation" Okamoto, S.; Saijo, K.; Hashimoto T. *Macromolecules*, **1994**, *27*, 3753.

Other Publications

1. "Living Cationic Polymerization of Vinyl Monomers by Organoaluminum Halides V. Polymerization of Isobutyl Vinyl Ether with EtAlCl2 in the Presence of 2,6-Dimethyl Pyridine and Related Amines" Higashimura, T.; Okamoto, S.; Kishimoto, Y.; Aoshima S. *Polym. J.*, **1989**, *21*, 725.

2. "Viscoelastic Behavior of a Homogeneous Polystyrene-*block*-Polyisoprene-*block*-Polystyrene Copolymer" Han, C.D.; Baek, D.M.; Kim, J.K.; Hashimoto, T.; Okamoto, S. *Macromolecules*, **1991**, *24*, 5408.

3. "FRS Study of the Diffusion of a Block Copolymer. 1. Direct Determination of the Anisotropic Diffusion of Block Copolymer Chains in a Lamellar Microdomain" Ehlich, D.; Takenaka, M.; Okamoto, S.; Hashimoto T. *Macromolecules*, **1993**, *26*, 189.

Acknowledgments

The presented studies are based upon the studies carried out under the guidance of Professor Takeji Hashimoto at the Department of Polymer Chemistry, Faculty of Engineering, Kyoto University, from 1988 to 1994.

The author wishes to express his sincere gratitude to Professor Hashimoto for his constant guidance, encouragement, valuable suggestions and discussions in the course of his studies. He also wishes to express his thanks to Professor Hirokazu Hasegawa at the Department of Polymer Chemistry, Faculty of Engineering, Kyoto University, for his helpful suggestions, valuable comments and kind supplement of sample specimens. He also wishes to express thanks to Mr. Kenji Saijo at the Department of Polymer Chemistry, Faculty of Engineering, Kyoto University for his continuous support in the SAXS measurements.

The author acknowledges to Drs. Toshio Higashimura, Sadahito Aoshima, Shinichi Sakurai, Mikihito Takenaka, Ehlich Dietmar, Yoshinobu Isono, Atsushi Takano, Hongmin Zhang, and late Professor Teruo Fujimoto for his useful suggestions, cooperation and kind supplement of sample specimens.

The author also acknowledges to Dr. Shoji Suehiro, Miss Akemi Nakai and Mr. Takeo Kazama for valuable comments and help.

Finally, the author expresses his thanks to Professors Sadao Hibi and Eiji Nakanishi, at the Department of Material Science and Engineering, Nagoya Institute of Technology, and his parents, Hisao and Shigeko Okamoto for their care and constant encouragements during the studies.

March 1997 Shigeru Okamoto